SEA LEVEL AND SEDIMENTS:

SOURCES, SINKS AND SIGNALS

AN ABSTRACT

SUBMITTED ON THE XXXXTH DAY OF AUGUST 2022

TO THE DEPARTMENT OF EARTH AND ENVIRONMENTAL SCIENCES

IN PARTIAL FULLFILLMENT OF THE REQUIREMENTS

OF THE SCHOOL OF SCIENCE AND ENGINEERING

OF TULANE UNIVERSITY

FOR THE DEGREE

OF

DOCTOR OF PHILOSOPHY

BY

Udita Mukherjee

APPROVED:

Torbjörn E. Törnqvist, PhD
Director

Kyle M. Straub, PhD

Nicole Gasparini, PhD

Glenn Milne, PhD

Brent M. Goehring, PhD

ABSTRACT

Mass redistribution on the continental shelf, both with respect to meltwater from ice sheets and sediments being transported by rivers into the ocean, over time and space is of interest especially to stratigraphers and paleoclimate researchers. During the last deglaciation, ice sheets melted to raise sea level, with the shoreline moving onshore on the continental shelf. In the first chapter of this dissertation, I have explored the partitioning of meltwater coming from the North American and the Antarctic ice sheets during the last phase of this deglaciation. I show that the north American ice sheet was the major contributor of meltwater to the global oceans about 9000-7000 years ago. In the next chapter, I have looked at fundamental questions about transport of sediments into deep ocean during the sea-level lowstands and the factors behind formation and progradation of the shelf edge, using the distinctly different western and eastern shelves of southern Africa. In the last chapter, I have field-tested the signal shredding theory using a seismic volume from the Mississippi delta and have shown that preservation potential of different relative sea level signals of varying amplitude in the strata are different, which is dependent also on the internal dynamics of the largest sediment transport system present locally. This dissertation presents research work that progresses our understanding of paleo sea level, stratigraphy and source to sink sediment transport.

SEA LEVEL AND SEDIMENTS:

SOURCES, SINKS AND SIGNALS

A DISSERTATION

SUBMITTED ON THE XXXXTH DAY OF AUGUST 2022

TO THE DEPARTMENT OF EARTH AND ENVIRONMENTAL SCIENCES

IN PARTIAL FULLFILLMENT OF THE REQUIREMENTS

OF THE SCHOOL OF SCIENCE AND ENGINEERING

OF TULANE UNIVERSITY

FOR THE DEGREE

OF

DOCTOR OF PHILOSOPHY

BY

Udita Mukherjee

APPROVED:

Torbjörn E. Törnqvist, PhD
Director

Kyle M. Straub, PhD

Nicole Gasparini, PhD

Glenn Milne, PhD

Brent M. Goehring, PhD

ACKNOWLEDGEMENTS

TABLE OF CONTENTS

LIST OF TABLES

LIST OF FIGURES

INTRODUCTION

Continental shelf systems are among the first responders to changes in sediment delivery and relative sea level (RSL) cycles. The continental shelf is the part of the Earth's continental margin system which lies between the shoreline and the continental slope, with an average width of 75 km and an average slope of ~0.1° (Jackson, 1997; Slatt, 2013). Generally, the water depth in this area is quite shallow (average depth ~60 m). However, depending on the tectonic setting, amount of sediment delivery to the shelf as well as the base level (RSL), continental shelves vary immensely around the world. In the following chapters of this dissertation, I explore mass redistribution over time as well as space in the continental shelf, including both changes in volume of water caused by changes in sea level, as well as sediments delivered to this part of the continental margin system.

The Earth has gone through changes in sea level over various timescales throughout its history. During the most recent lowstand, the Last Glacial Maximum (LGM), about ~21,000 years ago, the Earth was covered by extensive continental ice sheets, and sea level was ~130 m lower than present (Clark et al., 2009). With more water trapped in ice sheets during the culmination of the LGM, less land area was covered by oceans and, hence, left to the mercy of the elements to be eroded. As continents wear down over time, rivers carry the eroded sediments to the oceans. These RSL changes also affect transport of sediments in source to sink (S2S) systems. Ocean basins deepen from the shallow continental shelf to the deep ocean, with the continental shelf edge defining the margin between the two. The continental shelf, which is connected to the continent, may or may not be under water during low sea level. The conventional models of sediment delivery systems during such sea-level lowstands assume that the shoreline generally is located below or at the shelf edge, which in turn facilitates the transport of sediment to the deeper ocean (Posamentier and Vail, 1988a). However, recent research has shown that this is not always the case. Many other factors can control sediment-transport systems on the continental shelf during sea-level lowstands.

As shorelines recede during falling sea level, rivers must travel a longer distance to reach the sea, but whilst at it, they often carve out valleys on the shelf, making it easier for sediments to reach the deep marine environment. Sediment transport mechanisms across the shelf edge and the factors that control them are important for several natural processes, like controlling the amount of sand that can make its way into deep-water environments, the formation and maintenance of the shelf edge itself, environmental signal propagation which helps us in understanding long-term climate change (among other things), as well as global carbon cycling, to name a few. These paleovalleys and other associated sediment delivery features can also be preserved in the subsurface strata and can be used for reconstructing the geologic past.

During these last 20 kyr, RSL has been constantly rising globally and according to the latest SROCC report, under RCP8.5, the rate of sea level rise in 2100 will be 10-20 mm/yr (Oppenheimer, 2019). Past RSL change events can be a major source of knowledge to understand future sea-level rise and the threat that this accelerated RSL rise poses in low-lying areas of the world. RSL change is defined as the elevation of the ocean surface with respect to the local solid Earth surface, excluding the dynamic sediment surface (Khan et al., 2019). Regional RSL data are important for a number of disciplines, ranging from glacial isostasy and ice sheet modeling to coastal restoration, archaeology and anthropology. We still do not know enough about how sediments get transported to the deep marine environment during RSL cycles and whether these RSL signals are stored in the stratigraphy. My projects deal with various aspects of RSL change and how it affects the S2S system.

Even though we have some understanding about past RSL changes (e.g. (Dutton et al., 2015; Lambeck et al., 2014)), we have some critical gaps in the early Holocene RSL history. For my first project, I am working on filling some of these gaps. One big question that remains to be understood is the contribution of different ice sheets, namely the North American and the Antarctic ice sheets to the EH RSL rise. I have used high resolution RSL data from four study areas around the world and glacio-isostatic adjustment (GIA) models. The implications resulting from this are important and myriad, and they are discussed in the relevant chapter in the thesis.

My second project deals with the question about sediment transport to the deep marine environment during RSL lowstands. Exposure of the shelf and the shelf edge depends on the amount of relative sea-level (RSL) fall, which in turn influences paleovalley incision that plays a big part in transporting sediments across the shelf edge. We use a glacial isostatic adjustment model of the southern African continental shelf to recreate the paleo-elevation of the region during the LGM. Using relatively simple geomorphic parameters involving the morphology of the shelf edge, the project seeks to answer questions about whether riverine sediments can reach the deeper marine sinks during RSL lowstands and its effect on progradation of continental shelf edge.

For my third project, I pursue the question of whether all RSL signals, regardless of size, get preserved in stratigraphy. Sediments transported from the source to the sink carry environmental signals which may or may not be preserved in the stratigraphy. For this project, we are interested in testing whether changes in the RSL signal gets stored in the stratigraphy, and if not, what type of base level change signals get stored in the rock record, using field datasets. Previous studies have deduced that only those RSL cycles with greater magnitudes and periodicities than the spatial and temporal scales of the internal (autogenic) dynamics of deltas can be extracted from the stratigraphic record. A publicly available seismic cube from NAMSS-USGS has been used to study the long-term signal shredding ion the Gulf of Mexico shelf. In this chapter, I show that the larger Quaternary RSL signals (amplitude of ~60-70 m) were stored in the Mississippi River Delta strata, but the smaller Miocene RSL signals (amplitude of 10 m) were shredded by the internal processes of the same depositional system. This attempt is one of the first of its kind to evaluate the theories of signal shredding from field datasets.

Dutton, A., Carlson, A. E., Long, A., Milne, G. A., Clark, P. U., DeConto, R., Horton, B. P., Rahmstorf, S., and Raymo, M. E., 2015, Sea-level rise due to polar ice-sheet mass loss during past warm periods: science, v. 349, no. 6244, p. aaa4019.

Jackson, J. A. e., 1997, Glossary of Geology (fourth ed.), Am. Geol. Institute.

Khan, N. S., Horton, B. P., Engelhart, S., Rovere, A., Vacchi, M., Ashe, E. L., Törnqvist, T. E., Dutton, A., Hijma, M. P., and Shennan, I., 2019, Inception of a global atlas of sea levels since the Last Glacial Maximum: Quaternary Science Reviews, v. 220, p. 359-371.

Lambeck, K., Rouby, H., Purcell, A., Sun, Y., and Sambridge, M., 2014, Sea level and global ice volumes from the Last Glacial Maximum to the Holocene: Proceedings of the National Academy of Sciences, v. 111, no. 43, p. 15296-15303.

Oppenheimer, M., B.C. Glavovic , J. Hinkel, R. van de Wal, A.K. Magnan, A. Abd-Elgawad, R. Cai, M. Cifuentes-Jara, R.M. DeConto, T. Ghosh, J. Hay, F. Isla, B. Marzeion, B. Meyssignac, and Z. Sebesvari,, 2019, Sea Level Rise and Implications for Low-Lying Islands, Coasts and Communities., in B.C. Glavovic , J. H., R. van de Wal, A.K. Magnan, A. Abd-Elgawad, R. Cai, M. Cifuentes-Jara, R.M. DeConto, T. Ghosh, J. Hay, F. Isla, B. Marzeion, B. Meyssignac, and Z. Sebesvari,, ed.: IPCC Special Report on the Ocean and Cryosphere in a Changing Climate.

Slatt, R. M., 2013, Nondeltaic, Shallow Marine Deposits and Reservoirs, Developments in Petroleum Science, Volume 61, Elsevier, p. 441-473.

CHAPTER 1: Partitioning early Holocene North American v. Antarctic ice melt from high-resolution reconstructions of sea-level rise and glacial isostatic adjustment modeling

ABSTRACT

According to the SROCC report, under RCP8.5, the rate of sea level rise in 2100 will be 10-20 mm/yr and extreme sea level events will become common. Past relative sea level (RSL) change informs our understanding of future sea-level rise and the threat that acceleration of RSL rise poses in low-lying areas around the world. The Early Holocene (EH), the most recent time interval with rapid ice-sheet retreat and rapid sea level rise, contains critical gaps in RSL history that are one of the remaining outstanding questions regarding eustatic sea level (Khan et al., 2019). A better understanding of the rates and sources of RSL change between 10-7 ka can help in better predictions of future sea level rise, particularly since the melting of Antarctic ice sheet may have been a key contributor to this high rate of sea level rise.

A new RSL record from the Mississippi Delta comprising eight sea level index points (SLIP) and seven upper limiting data points extending to about 10 ka has been assembled as part of this project. A global RSL database spanning 10-7 ka has been prepared as well, using a rigorous set of criteria to control the quality of the indicators. The observed RSL rate of change at the four locations is compared to model output calculated using a suite of Earth viscosity models and ice sheet chronologies from approximate Bayesian

calibrations of glaciological models for the Antarctic and North American Ice Sheets to determine the ice sheet histories and north-south partitioning that best fit the data.

1.1 INTRODUCTION

According to the latest IPCC report, under the middle of the road and the extreme scenarios the rate of global mean sea level (GMSL) rise in 2100 will be 5-12 and 9-18 mm/yr respectively (Fox-Kemper et al., 2021). Globally averaged rates of sea-level rise during the early Holocene (eH), between ~11.4 and 8.2 ka, were on the order of 15 mm/yr (Lambeck et al., 2014b). Despite the different cause of high latitude warming during the eH compared to the present (orbital v. greenhouse gas forcing), this period could offer unique insights into ice sheet–sea level interactions, with relevance for the future, but this period remains strikingly understudied (Törnqvist and Hijma, 2012). Sophisticated observations of present day ice-sheet dynamics (IMBIE, 2018; IMBIE et al., 2020; Joughin et al., 2014; Rignot et al., 2011; Shepherd et al., 2012; Tapley et al., 2019; van den Broeke et al., 2009) and sea-level rise (Cazenave et al., 2014; Dangendorf et al., 2017; Frederikse et al., 2020; Hamlington et al., 2020; Stammer et al., 2013) using a wide range of remote sensing techniques, along with a variety of modeling approaches [e.g., (Golledge et al., 2019; Moore et al., 2013)] are underway. However, instrumental studies of ice sheets and sea level are inevitably limited by the short time span of observation (decadal and century scale, respectively). Including the paleo-record to our understanding of sea-level change during past periods of rapid loss of continental ice can be a major source of knowledge, extending our understanding of relative sea level (RSL) change, and can be used to ground-truth model predictions (Alley et al., 2005; Gehrels, 2010; Horton et al., 2020; Khan et al., 2019; Levermann et al., 2013; Milne et al., 2009).

A number of sea-level studies have targeted past warm intervals like the last interglacial (Eemian or Marine Isotope Stage (MIS) 5e), MIS11 and the mid-Pliocene [e.g., (Barlow et al., 2018; Dutton et al., 2015; Dutton and Lambeck, 2012; Raymo and Mitrovica, 2012; Raymo et al., 2011) to understand the ice-sheet volumes and melt rates during these periods. However, community papers like PALSEA (PALeo SEA level working group) (2010) and Khan et al. (2019) have concluded that "the early to mid-Holocene may be key to understanding future sea-level change" and one of the remaining outstanding questions regarding barystatic sea level (BSL) (Gregory et al., 2019). As we go back in time towards the early Holocene, high-resolution RSL indicators become sparser (Khan et al., 2019). One reason for this is that areas where these records are preserved in the stratigraphy are now offshore, as the shoreline retreated over time, and thus these records are more difficult to obtain than the ones from the late Holocene. It is easier to find such data in thick Holocene progradational sequences, like large deltas.

Regional RSL reconstructions from the Gulf of Mexico [eg. (Simms et al., 2007a)] show 10-15 m higher RSL elevations compared to the global average during the time period of 8-10 ka. Even though the magnitude of the total deglacial sea-level rise since the Last Glacial Maximum is increasingly well known and is now believed to be about 130 m (Austermann et al., 2013; Lambeck et al., 2014b), the difference between the estimates of this quantity from sea-level observations versus those from ice sheet reconstructions is large (Clark and Tarasov, 2014; Simms et al., 2019). The missing ice issue for the LGM is well recognized, but here we show that this issue may extend throughout the last deglaciation.

The time-period between 9-7 ka accounts for about 20 m of BSL rise (Lambeck et al., 2014b). Around 7 ka, the rate of GMSL increase had slowed by an order of magnitude (Smith et al., 2011) than the SL rate of ~15mm/yr during the eEH to stay mostly close to the present-day RSL. Between 9 and 7 ka, two rapid RSL jumps have been reported in the literature: at 8.2 ka (e.g., Törnqvist et al., 2004) and 7.6 ka (e.g., Blanchon et al., 2002). The decay of the Eurasian ice sheet was complete by ~9.7 ka (Carlson and Clark, 2012; Stroeven et al., 2016), so this ice sheet did not contribute to the global SL rise between 9-7 ka. The North American Ice Sheet (NAIS), and the Antarctic Ice Sheet (AIS) are believed to have contributed to the RSL rise during the 9-7 ka time period, but the contributions of each of these ice sheets are not well constrained (Carlson and Clark, 2012; Smith et al., 2011; Törnqvist and Hijma, 2012). The reconstruction of ice margins in formerly glaciated terrains only constrains ice-sheet area, not thickness. Even though this is an important source of evidence, ice-sheet thickness is very important for converting ice-area changes into equivalent sea-level changes. From a glaciological perspective, this can only be directly constrained in high-relief settings with undisputable trim lines. However, reconstructions of sea-level change during periods of rapid ice retreat can also be used to estimate the volume of ice-sheet melt and in turn, their thickness. The spatial extent of the LIS is better constrained compared to that of the AIS. However, there is a lack in ice-thickness data for the LIS, leading to disparities in different models and ice-sheet reconstructions (Törnqvist and Hijma, 2012). During the eH, Carlson et al. (2008) estimated that the contribution of the LIS was ~30 m, whereas Roy and Peltier (2017), using the recent ICE-6G model used an ice melt contribution of ~27 m. ICE-5G, on the other hand, predicts that the contribution of the NAIS to be ~20 m during the eEH (Peltier, 2004). Carlson et al. (2008) calculated the contribution of LIS between 9-7 ka to be ~14 m sea level rise. The contribution of the AIS during eH over the last deglaciation is highly uncertain and a range of ~1.2m-~8.5 m sea level rise have been proposed for this (Albrecht et al., 2020; Golledge et al., 2014; Ivins et al., 2013; Whitehouse et al., 2012a). Spector et al. (2017) indicate that the Ross Sector of the AIS contributed the most to sea level during ~9-8 kyr, but the total contribution of this sector to RSL has been shown to be only 3-4 m during the entire deglaciation (Briggs et al., 2014; Whitehouse et al., 2012). For the Weddell Sea sector, Nichols et al. (2019) estimates a minimum contribution of is not more than 4.6 m for the entire deglaciation. These observations suggest that the meltwater contribution of the AIS was significantly lower than that of the LIS during the period 9-7 ka. However, the uncertainties in these vital issues remain and they add to the uncertainties in freshwater forcing of the ocean circulation system. There is a need to resolve these differences in calculations with a better constraint on the sea level rise and ice-sheet retreat between 9-7 ka. This time-period includes the most prominent abrupt climate event during interglacial conditions (the 8.2 ka event), and it can be used as a very useful analog for understanding icesheet melt during the relatively warm climate conditions of today and the future.

A well-constrained RSL database is necessary to calculate accurate rates of RSL change. Collating and presenting RSL data from around the world require a well-defined RSL protocol to document the necessary information and quantify all the possible errors involved, has become an essential part of these types of studies. Sifting through the literature, three high-resolution RSL records from the eH from the Rhine-Meuse Delta, the Yangtze Delta and the Malay Peninsula have been documented, and will be discussed in the following sections. A new record from the Mississippi Delta that covers the time-period till 10 ka is also reported here. Using the RSL records and glacial isostatic adjustment (GIA) models, we have calculated the partitioning of the NAIS vs. AIS meltwater volumes during 9-7 kyr. The meltwater contribution from NAIS between 9-8 kyr was significantly higher than what was known earlier, and we believe that addition of extra freshwater to the North Atlantic around this time would have significant effect on the abrupt climate change that happened during 8.2 kyr. Enhanced addition of freshwater to the North Atlantic Ocean could have also affected different components of the climate system like the Atlantic Meridional Overturning Circulation (AMOC), which is of interest to the climate and sea level community, as well as the paleoclimate community in connection to its effect in a future warming world.

1.2 RSL data evaluation

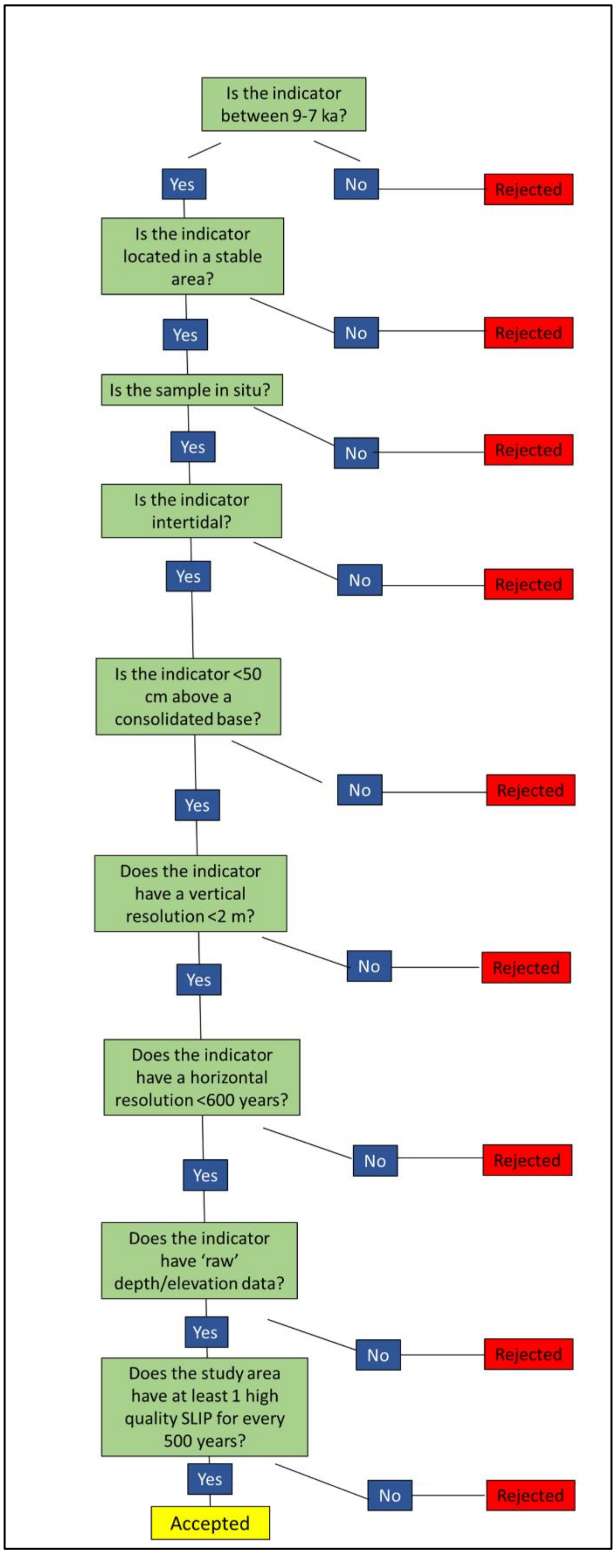

Figure 1 The flowchart with all the criteria used to evaluate RSL data.

To standardize the quality of data that are used in this work, we have used a set of criteria (Fig. 1) against which every RSL datapoint has been evaluated. Due to the difference in approaches, techniques, and the types of research questions, the available RSL data from around the world are not of the same quality across the board. The goal of creating this set of criteria is to systematically choose the best quality RSL record, given the objectives of this study. To be included in the database, an RSL record should contain high-quality RSL indicators which best describe the RSL history of a given geographic area from 9 to 7 ka . These RSL indicators must be between 9-7 ka in age (the central age of the ^{14}C age distribution), from a reasonably stable area, an *in situ* and relatively uncompacted intertidal sea-level index point (SLIP), with a quantifiable 2σ vertical and horizontal resolution. Here we describe the criteria used to create this database in more detail.

1.1.1 *Age of the sample*

After the decay of the EIS at ~9.7 ka (Carlson and Clark, 2012; Hughes et al., 2016; Stroeven et al., 2016), the meltwater for the global sea-level rise must have been partitioned between the NAIS and the AIS. The rates of BSL rise showed a marked deceleration at around 7 ka and it corresponds with the end of significant melting of the LIS (6.7±0.4 ka) (Carlson et al., 2008). However, to constrain meaningful uncertainty calculation near the end points of the RSL curves by the Bayesian modeling methods (Section 3), we increased our search interval to include slightly younger and slightly older samples. So, the SLIPs and limiting data included in this database are 6-10 ka, along with one additional SLIP (~4.5 ka in age) in Malay Peninsula due to a dearth of data younger than 7.5 ka in this area. It is extremely rare to find SLIPs which satisfy all our criteria as we get closer to 10 ka. A few well-constrained upper limiting data points have also been included to test the validity of calculated paleo-RSL.

The other issue related to sample ages concerns dating uncertainties. Beachrocks (Mauz et al., 2015) and mangrove muds (Sefton et al., 2021; Woodroffe et al., 2015) are two examples where dating issues are very common and thus, only a few RSL indicators from these materials are used in the current database. Dating beachrocks using broken cemented *ex situ* materials like shell fragments or recrystallized cements do not provide the actual age of the formation of the beachrock. Using mangrove sediments to reconstruct RSL history, on the other hand, can be challenging because of their complex carbon cycling processes (Sefton et al., 2021). Dating bulk mangrove sediments, roots, reworked pollen concentrates, and bioturbated and tidally reworked materials can provide problematic results due to introduction of carbon from different sources. Compared to saltmarshes, mangrove roots penetrate deeper (up to 2 m) into the subsurface, and the roots form a large proportion of the biomass of the mangroves. These large mangrove roots introduce younger carbon in the samples, which, along with other sources of carbon contamination like surficial and subsurface exchange of carbon due to tidal flow, can lead to dating issues in mangrove samples.

2.1.1 Location

RSL indicators which might be affected by tectonic or other vertical movements (GIA), such as most near-field locations and active margins, have not been considered here, so that no major tectonic or GIA corrections are needed. A map (Fig. 2) combining the extent of ice sheets during the Last Glacial Maximum and the major tectonic plate boundaries, with a somewhat arbitrary buffer of 250 km and 350 km (Dura et al., 2015; Sella et al., 2007) respectively, has been created to select the study locations, to avoid the active areas affected by vertical movement.

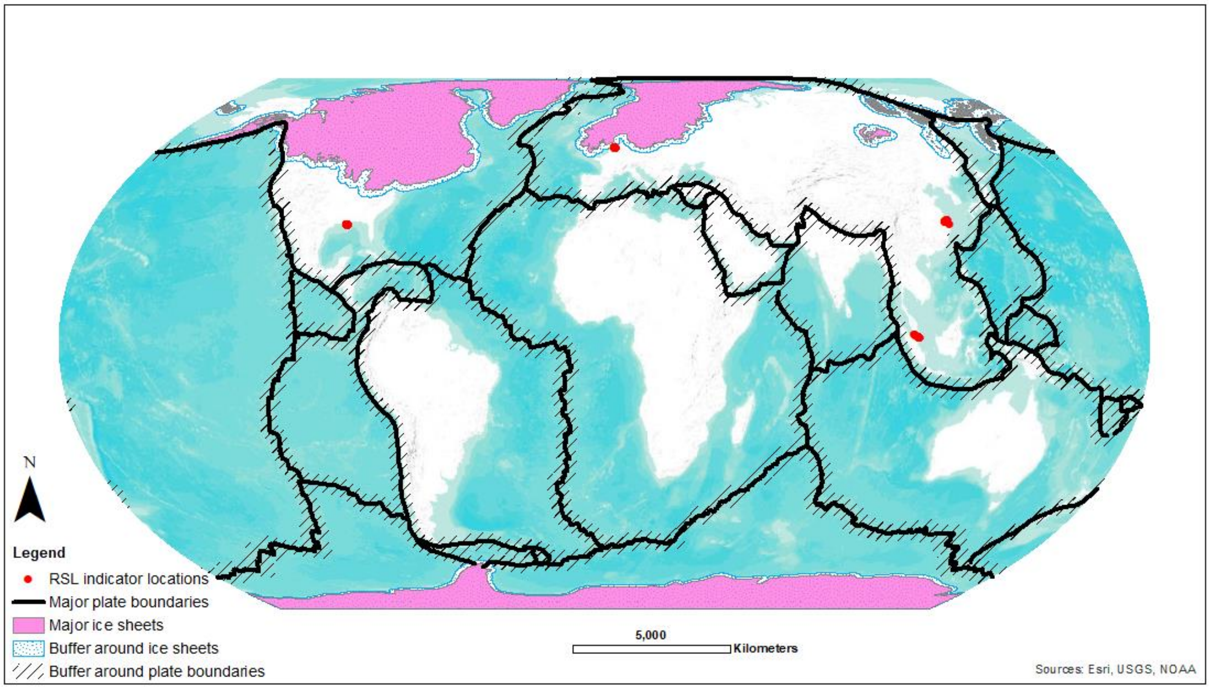

Figure 2. Map showing the extent of ice sheets during the Last Glacial Maximum (Ehlers et al., 2011) and the major tectonic plate boundaries (Bird, 2003) used to avoid areas where the Earth's surface is affected by significant vertical movements. The black lines represent the major plate boundaries with the area covered by the hatched black area represents a buffer zone of 350 km, and a buffer of 250 km around the major ice sheets are shown by the blue dotted area. The red circles represent the locations of the four study areas (Mississippi Delta, Rhine-Meuse Delta, Yangtze Delta, and Malay Peninsula).

2.1 *Undisturbed samples*

Once an RSL indicator passes the eligibility criteria for timing and location, the characteristics of the material that was dated were studied in detail to assess its eligibility for the database. A large number of samples were *ex situ*. These *ex situ* materials had been shifted posthumously from the position where they were formed, leading to misinterpretation of their relationship to RSL during their formation. Thus, only *in situ* samples, which have preserved their relationship to the past RSL when they were formed, are considered in this database. For example, offshore shell samples that are not articulated and therefore are suspected to be *ex situ* have been rejected from the database.

2.2 *Type of sea-level indicator*

For accurate estimation of RSL change in each study area, the indicative meaning of the samples must be determined. The indicative meaning tells us where the RSL indicator formed with respect to the contemporaneous reference water level (Hijma et al., 2015; Shennan, 1982). Different types of RSL indicators have different indicative meanings, consisting of two parameters: the indicative range (IR) and the reference water level (RWL). The entire range over which an RSL indicator could have formed is defined as the IR and the RWL is the mid-point of this range, expressed with reference to a geodetic datum, similar to the one used to determine the sample elevation. Depending on whether a specific indicator can be assigned an IR, it can be classified as a SLIP) or a limiting data point (LDP) (Shennan, 1982; Hijma et al., 2015). The RSL of a SLIP is calculated using the following equation:

$$RSL = Sample\ elevation - RWL \text{ (m)}$$

For a LDP, the same calculation as that of a SLIP is used, but it is labeled as an upper LDP or a lower LDP in the database. The SLIPs in the database are basal peats and plant fragments from tidal flats.

2.3 *Compaction*

Compaction of sediments used as SLIPs is a major concern. There might be vertical displacement of the sample on the order of several meters (Tornqvist et al., 2008; Van Asselen et al., 2009), and the presently available compaction correction models come with a high degree of uncertainty (eg., (Bird et al., 2004; Brain et al., 2012; Van Asselen et al., 2009). For materials deposited on a consolidated basement, the top ~0.5 m of organic-rich sediments shows a compaction ratio close to 100%, i.e, the compaction is negligible (Brain et al., 2012; Keogh et al., 2021). The compaction ratio remains near 100% within 100 cm of burial and only starts to significantly increase below that (Keogh et al., 2021). However, Keogh et al. (2021) only considered surface sediments, which is different from the basal peats and related sediments used here. Sediments that sit higher up in a core can be compacted up to 50% based on the difference of elevation between the sample and the consolidated basement. Thus, to reduce the error that might be introduced into the RSL histories due to the use of compacted sediments as SLIPs, we are only using materials which were sampled within 50 cm from the top of the consolidated basement.

Basal peats are the most preferable and commonly dated RSL indicators for this type of analysis. They form as soon as the groundwater level rises above the land surface, thus making them a well-suited candidate for SLIPs forming due to the transgression of the sea over the consolidated substrate (usually Pleistocene). For buried organic-rich samples, we increase the sample thickness by a factor of 2.5, and by a factor of 4 for the deepest samples in the Mississippi delta and use that as an error (Hijma et al., 2015; Keogh et al., 2021). Without sufficiently detailed stratigraphic information, it becomes difficult to ascertain the amount of vertical displacement and thus such samples have been rejected.

2.4 *Time and elevation resolution*

The 2σ horizontal (time) and vertical (elevation) resolution of the samples is extremely important with respect to the questions asked here. Since we are interested in ~2000 years of deglacial history, the temporal resolution has to be small enough to meaningfully piece together the timing of the RSL change during this period, but an overly strict criterion will lead to the rejection of data in an already under-examined time window. The temporal resolution of an indicator has been decided to be <600 years, which gives us an optimal trade-off between resolution and the numbers of surviving data points.

With respect to vertical resolution of the data, the same arguments are applicable. To resolve the last few tens of meters of RSL change during the 9-7 ka time window, high-resolution records are to be used, making it necessary for the vertical resolution to be <2 m, which is less than half the Greenland Ice Sheet. For example, this leads to the exclusion of RSL records constructed using corals. Even though corals have been extensively used to study the postglacial RSL history in different parts of the world, due to their low vertical resolution (>5 m), they are unable to reduce errors on reconstructed rates of RSL rise to make a rigorous data-model comparison (Gehrels, 2010; Törnqvist and Hijma, 2012), and have therefore not been included here.

2.5 Elevation

Without the critical "raw" depth/elevation information that is needed to rigorously assess a RSL indicator, it will not be included in the database. Some studies only report the calculated paleo-RSL (eg., (Lewis et al., 2008)), without the elevation from which the samples were extracted, which makes it impossible to recalculate paleo-RSL, when new information about the IR or RWL becomes available. Knowing the accurate sampling elevation of a RSL indicator as well as its RWL is essential to understanding RSL changes. Linking geodetic datums to local RSL is more useful than to link it with other datums (e.g., tidal datums), because geodetic datums remain constant for a longer period of time. The indicators in this database are assigned their respective geodetic datum, elevation and/or depth and the surveying and sampling methods, as they are mentioned in the original publications.

2.6 Data density

The aim of creating this database is to understand the partitioning of meltwater coming from the Antarctic and the North American ice sheets. For this, we need eH RSL records from intermediate and far-field locations around the world, which can then be used to compare with modeled RSL rates. Using the RSL indicators that we collate in the database, we have further used Bayesian modeling to calculate the RSL estimates and the rate of RSL change during the eH, as described in the following section. To produce meaningful results from these data, a number of high-quality datapoints that are spread evenly to cover the entire time interval of interest is used here.

1.3 Database Structure

The sea-level indicators used in this project have been collated in the HOLSEA database format (Khan et al., 2019). The protocol to collate RSL indicators in databases provided in Hijma et al. (2015) has been followed in putting together this database, estimating various errors and corrections, and a detailed discussion about all the components of the database can be found there. The end goal of analyzing any RSL indicator is to calculate at what elevation (depth/elevation of the sample with the errors associated, briefly discussed in section 3.2) it formed and at what time (dating of the samples, with the uncertainties involved, briefly discussed in section 3.1), with relation to the RSL (indicative meaning, discussed in section 5). These indicators also have a number of uncertainties which are briefly discussed in section 3.3.

3.1 Dating

All the samples used in this RSL database have been dated using the radiocarbon method. All the radiocarbon samples have gone through isotopic fractionation correction (Stuiver and Polach, 1977), as mentioned in the publications. All the indicators collated in this database are intertidal basal saltmarsh and mangrove peats or plant remains from tidal flats, and they are not affected by marine or estuarine reservoir effects. In case of bulk peat samples, a bulk error of 100 years has been used (Hu, 2010). Also, in the few instances where only calibrated radiocarbon ages were reported, an appropriate age uncertainty has been introduced, as discussed in the relevant sections. We used OxCal (Bronk Ramsey, 2009, 2017) for calibrating the ^{14}C ages to calendar years, using the IntCal20 calibration curve (Reimer et al., 2020), and the weighted mean calibrated ages were used. The 2σ age errors, rounded to the nearest 10 years are also reported.

3.2 Elevation

In cases that lacked detailed information regarding the uncertainties in elevation of the RSL indicators, these errors had to be estimated, following Hijma et al. (2015), leading to mostly large (i.e., conservative) vertical errors. The data coming from publications with detailed documentation of these aspects tend to have smaller errors associated with their final paleo-RSL calculations. The final upward and downward vertical errors are calculated by the expression:

$$E_t = \sqrt{e_1^2 + e_2^2 + \cdots + e_n^2}$$

where e1, e2, …, en are individual component errors assigned to a specific data point related to its indicative meaning, sampling, and elevation measurement and Et is the total vertical error.

3.3 Compaction, paleotidal and GIA corrections associated with RSL indicators

The RSL data were also corrected for several other factors. To correct for compaction, the vertical distance between the base of the sample and the top of the compaction-free consolidated base is calculated. This distance is multiplied by 2.5, and in some cases, by 4 for the deepest samples and then added to the calculated paleo-RSL of the SLIP.

The sea-level indicators are also affected by paleotidal changes, which have been calculated using various paleotidal models for the different study areas (Hijma and Cohen, 2019; Hill et al., 2011; Uehara et al., 2002; Uehara et al., 2006). These paleotidal models were created for open marine tides, using paleobathymetry from GIA models, which might introduce greater uncertainties in the RSL indicators which are mostly onshore. Therefore we use the difference between the present IR and the paleo-IR as an additional error, following Hijma et al. (2015). Detailed paleotidal models are available for the Mississippi Delta (MD) (Hill et al., 2011) and the Rhine-Meuse Delta (Uehara et al., 2006; Van der Molen and Van Dijck, 2000; Van der Molen and De Swart, 2001) and these models have been utilized to calculate the paleo-IR for the SLIPs from these areas. However, even in these cases, limitations exist. For example, in Hill et al. (2011) and Uehara et al. (2006), which are the most detailed models available, 1000-year age increments are used. Uehara et al. (2006), Hijma and Cohen (2019) and others show that

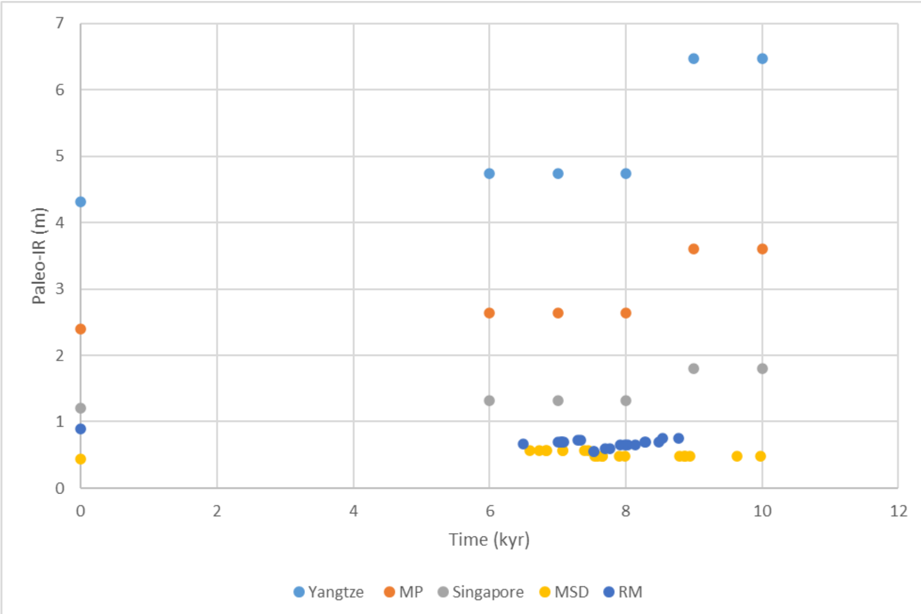

Figure 3. Comparing the changes in indicative range over time in different study areas, Yangtze delta (blue dots),Malay Peninsula (orange dots),Singapore (grey dots), Mississippi delta (yellow dots) and Rhine-Meuse delta (blue dots), as a proxy for calculating paleotidal uncertainties. The modern data comes from Admiralty Tide Tables.

the tidal range in the area surrounding Rotterdam, which is our study area in the Rhine-Meuse Delta, has remained fairly constant throughout the last 8 kyr, and this area was only flooded a while before this (Lambeck, 1995). In case of the RSL indicators from the MD, following Hill et al. (2011), the paleo-IR of samples older than 8 ka have been calculated by increasing the present day IR by a factor of 1.5. During the time period of 10 to 8 ka, studies like Hill et al. (2011) from the western North Atlantic and Uehara et al. (2002) from the Yangtze Delta have noticed a dramatic change in the tidal amplitude. Uehara et al. (2002) showed about a 50% increase from 6 to 10 ka in the YD in the M_2 magnitude. However, in case of Uehara et al. (2002), the models were only generated for the present day, 6 ka and 10 ka, so the exact timing of the increased tidal amplitude is not known. In the absence of detailed paleotidal modeling and paleo-tidal range reconstruction studies in the YD and Malay Peninsula, for RSL samples older than 8 ka, we have increased the present-day IR by a factor of 50% to calculate the paleo-IR and by a factor of 10% for samples younger than 8 ka. The present-day tidal parameters come from the Admiralty Tidal Tables (https://www.admiralty.co.uk/digital-services/admiralty-digital-publications/admiralty-totaltide).

GIA can cause slight spatial variability between sites within a single study area. To correct for this, the differences between the modeled RSL of a specific site and that of a central location using different Earth models, are calculated. The ICE-5G ice model has been used for these GIA models. The average of these differences for a specific time-period is then used to calculate the GIA uncertainty for al sampling sites within the study area. This is used to correct the paleo-RSL calculated from the data.

1.4 Bayesian statistical modeling of RSL records

RSL indicators can produce noisy data with both temporal, spatial and elevation uncertainties, and statistical models can be used to string these separate values into a quality-controlled consistent record for which these uncertainties are well quantified (Ashe et al., 2019; Düsterhus et al., 2016). To estimate the RSL history and calculate the rate of RSL change in the study areas, we use an Errors-in-Variables Integrated Gaussian Process (EIV IGP) model which performs Bayesian inference on RSL records, to calculate rates of RSL change (Cahill et al., 2015, 2016). Placing a Gaussian process prior on the rate of RSL change, the model then integrates to calculate the mean of the likelihood for the observed data. Both the independent (age) and dependent (elevation) variable uncertainties are considered by the EIV framework (Ashe et al., 2019; Cahill et al., 2015, 2016). This in turn captures the continuous dynamic change in RSL with all the uncertainties considered.

The age and calculated paleo-RSL of the SLIPs are used here as the input, with their one-sigma uncertainties, as required by the EIV-IGP model setup. The RSL estimates and rates of change are calculated for each of the records, with 95% confidence intervals (Section 5). This method uses only a few parameters and is simple and flexible when compared to other methods used in the past (Cahill et al., 2015). The estimated RSL and the rates of change of RSL calculated by this method are smoothed, which making it suitable for comparison with the rates calculated from GIA models which are also relatively smooth, due to the large age-increments used in these models. Note, however, that the uncertainties computed at the endpoints of the time series are exaggerated compared to the real uncertainties, herein referred to as 'edge effect'.

1.5 Description of individual records

Using the above-mentioned criteria for RSL indicators, the areas that have a well-constrained and useful record for our questions are the Yangtze Delta , the Rhine-Meuse Delta , the Mississippi Delta and Malay Peninsula. The records and the calculated rates of RSL change from these areas are presented in the following sections.

The Mississippi Delta

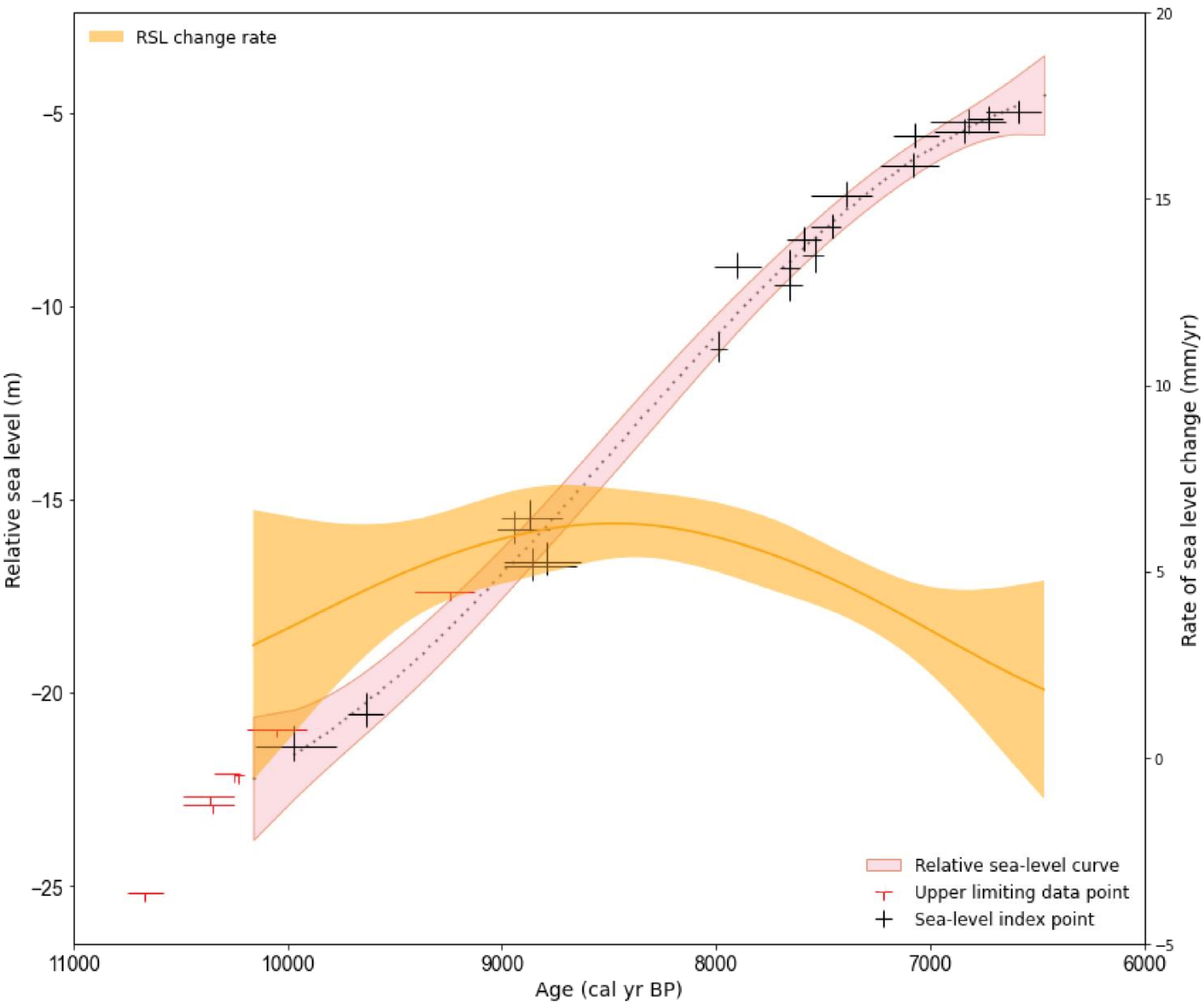

Figure 4. Plot showing the SLIPs, upper limiting data, estimated RSL, and the rate of change of RSL between 5-10 ka in the Mississippi Delta

A new RSL record was obtained from the eastern Mississippi Delta for the time interval ~8 to 11 ka, expanding on previously obtained and mostly younger RSL data from this region (Törnqvist et al., 2004b; Vetter et al., 2017). Here we report 14 ^{14}C dated cores (Extended Data Fig. x) with 53 ^{14}C ages (Extended Data Table y) from 25 discrete samples. This has resulted in 17 new RSL indicators (10 SLIPs and 7 upper LDPs) derived from basal peat or near-basal peat. This includes two recently published cores from the study area with SLIPs from basal peat (Vetter et al., 2017). The interpretation of the sea-level data is aided by stable carbon isotope ratios, plant macrofossils, and micropaleontology; ^{14}C dating was in most cases undertaken on multiple subsamples. All the data have been subject to rigorous error assessments, taking into account vertical changes due to sediment compaction and tidal-range change, as well as the role of sediment isostatic adjustment (see Methods).

The SLIPs and limiting data corroborate one another and collectively exhibit a comparatively modest and constant rate of RSL rise, with slightly higher rates between 9 and 8 ka. The record is constrained by SLIPs back to 10 ka; comparable rates of RSL rise may have occurred between 11 and 10 ka, considering the similarity between upper limiting data and SLIPs where they co-occur (Fig. 4). To our knowledge, this is the first RSL record that stretches back to 10 ka with a vertical resolution better than 1 m. This record differs markedly from the Lambeck et al. (2014) GMSL curve that shows a progressive rate increase before 7 ka (Lambeck et al., 2014b). While RSL in the MD was similar in elevation around 8.5 ka compared to the global sea-level curve of Lambeck et al. (Lambeck et al., 2014b), it plots ~15 m higher around 10 ka. Thus, we can now conclusively demonstrate what previous studies (Simms et al., 2007) had inferred: early Holocene RSL along the US Gulf Coast was considerably higher than the global average.

It is well documented that the Mississippi Delta has experienced slightly enhanced Holocene subsidence due to sediment isostatic adjustment (SIA) (Kuchar et al., 2018; Wolstencroft et al., 2014; Yu et al., 2012). We corrected for this effect based on these studies that used GIA modeling constrained by RSL data to infer a present-day SIA-driven rate of about 0.2 mm yr^{-1} for the study area. We assume here that this was broadly comparable during the early Holocene, even though the Mississippi Delta in its present configuration had yet to form. However, given that the shoreline was located near our study area, it is conceivable that rapid infilling of the paleovalley of the Mississippi River took place during this time, resulting in appreciable sediment loading. We assessed the uncertainty of the SIA component by using values of 0.1 and 0.3 mm yr^{-1} which resulted in small differences (about 1 m for the oldest part of the record).

The Rhine-Meuse Delta

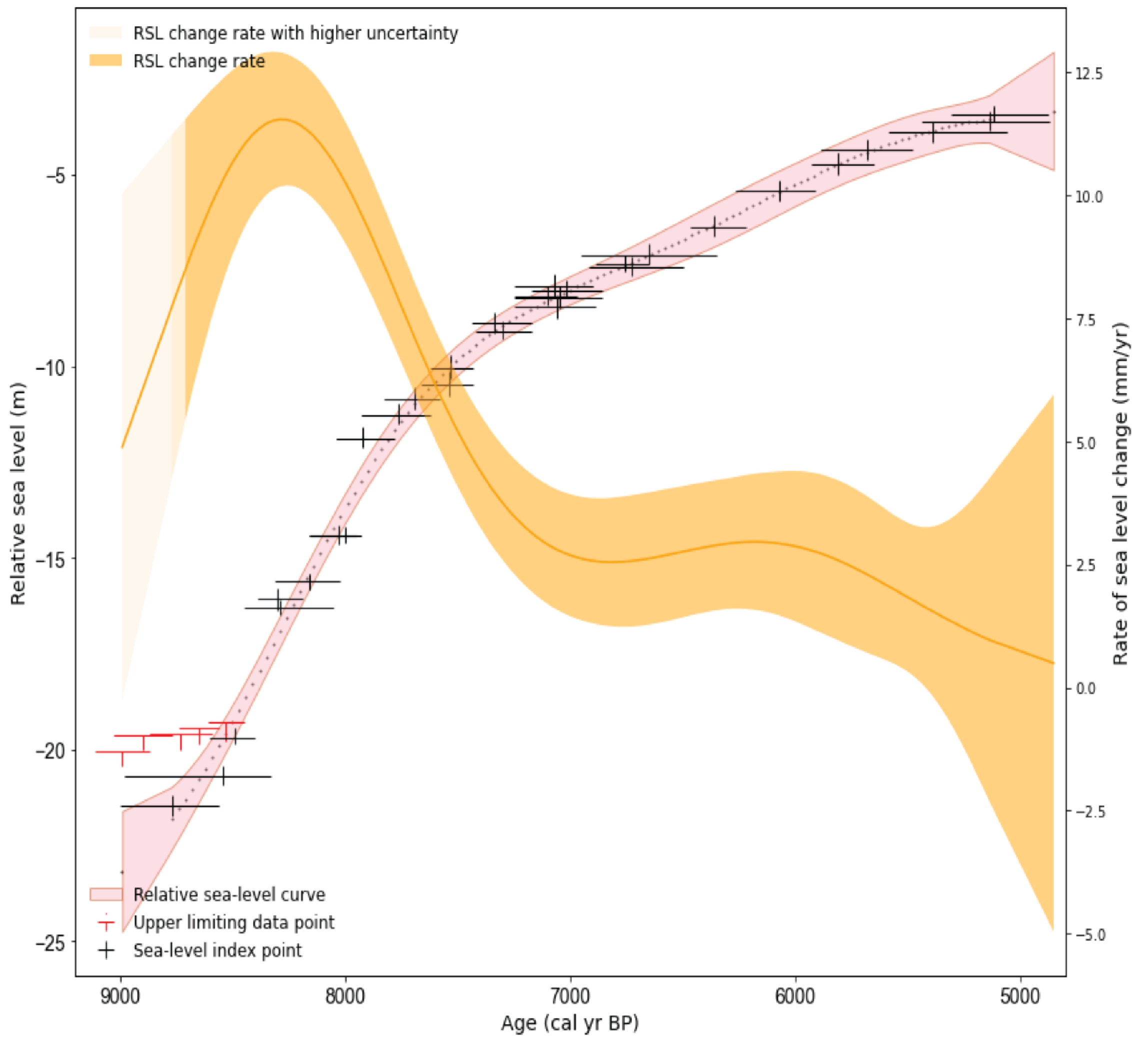

Figure 5 Plot showing the SLIPs, upper limiting data, estimated RSL, and the rate of change of RSL between 5-10 ka in Rhine-Meuse Delta

This record has 23 SLIPs and 5 upper LDPs from the Rotterdam and Maasvlakte areas of The Netherlands, compiled from Hijma and Cohen (2010, 2019), Van de Plassche et al. (1982, 1995; 2010), Berendsen et al. (2007), Vos (2013), Vos and Cohen (2015), Vos et al. (2015) and Jelgersma (1961). The SLIPs used here are all basal peats, sampled from the peat beds on buried eolian dune flanks, dune toes, and valley floors in the lower Rhine-Meuse Delta, and the upper limiting data are peat samples as well. We have adopted most of the interpretations and error calculations for the RSL indicators from Hijma and Cohen (2019), who have used the RSL database protocol as described in Hijma et al. (2015). For the RSL indicators from the Rhine- Meuse Delta, Yangtze Delta and the Malay Peninsula, a conservative RWL has been used for the SLIPs, defined to be (HAT+MTL)/2. For the upper limiting data, the RWL has been defined to be the MTL.

The RSL record for the Rhine-Meuse Delta covers the entire 9-7 ka period. However, the oldest SLIP in this has a central age of 8.77 cal a BP. This increases the uncertainty for the RSL curve and RSL change rate calculated using EIV-IGP in the oldest portion of the record that therefore carries less weight in our interpretation (below). The peak rate of RSL rise in the Rhine-Meuse Delta was ~11 ±2 mm/yr around 8.2 ka.

<u>Malay Peninsula</u>

The RSL history of the Malay Peninsula is based on radiocarbon ages from basal peats as described in Geyh et al. (1979) and Chua et al. (2021) from Singapore. We have interpreted six basal mangrove peat samples from Geyh et al. (1979) and three basal

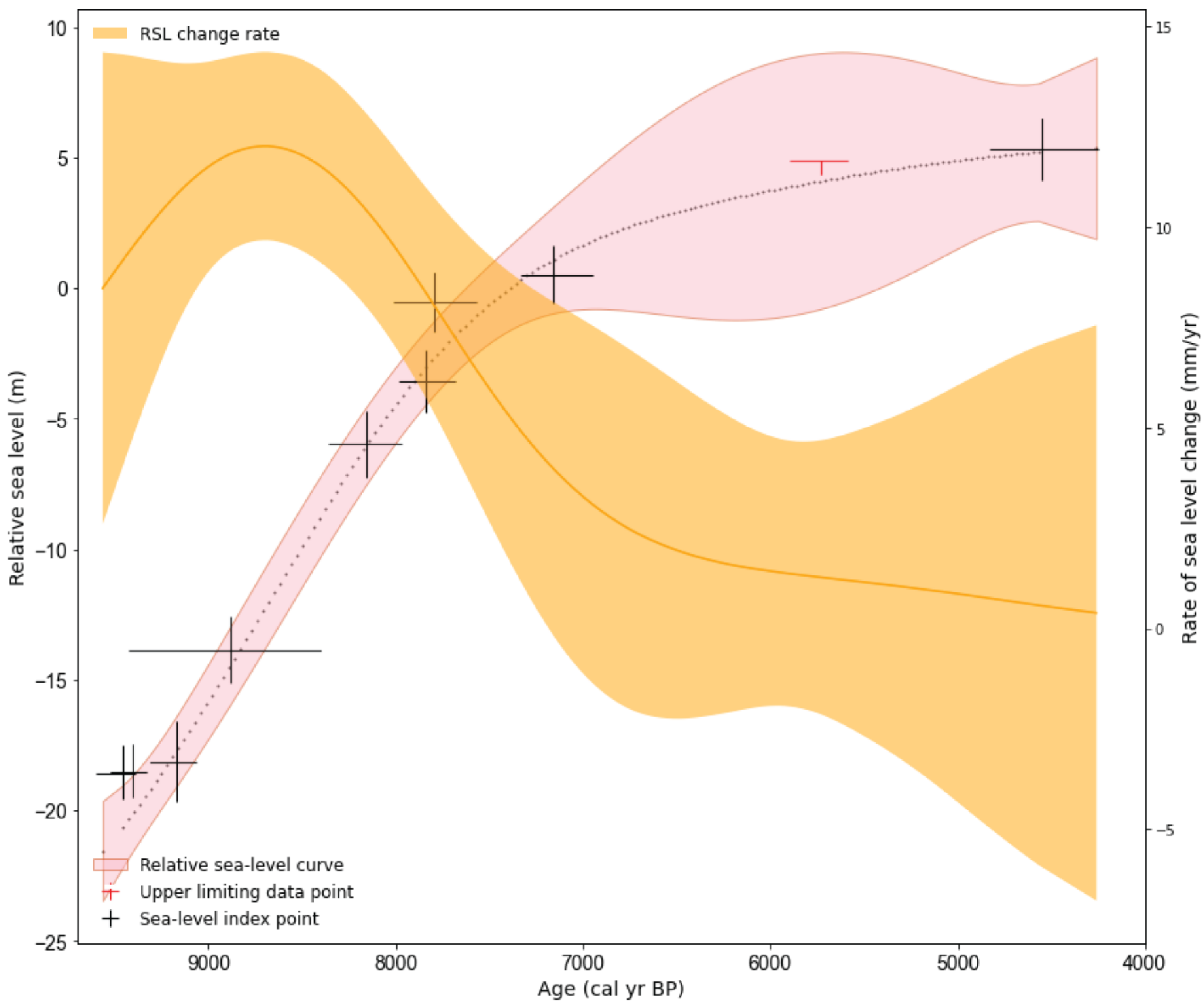

Figure 6 Plot showing the SLIPs, upper limiting data, estimated RSL, and the rate of change of RSL between 4 -10 ka in the Malay Peninsula

mangrove peat samples from Chua et al. (2021) to be SLIPs and one mangrove peat sample (Geyh et al., 1979) to be an upper limiting data point. The SLIPs from Geyh et al. (1979) are described as basal peats overlying terrestrial deposits, without any erosional hiatus with the overlying marine deposits. The lone upper LDP is a peat overlying brackish water deposits, which is not a basal peat.

The Yangtze Delta

In the southern Yangtze Delta region of China, the RSL history is reconstructed using sea level data reported in Wang et al. (2018; 2013), Zong et al. (2011), and Zhao

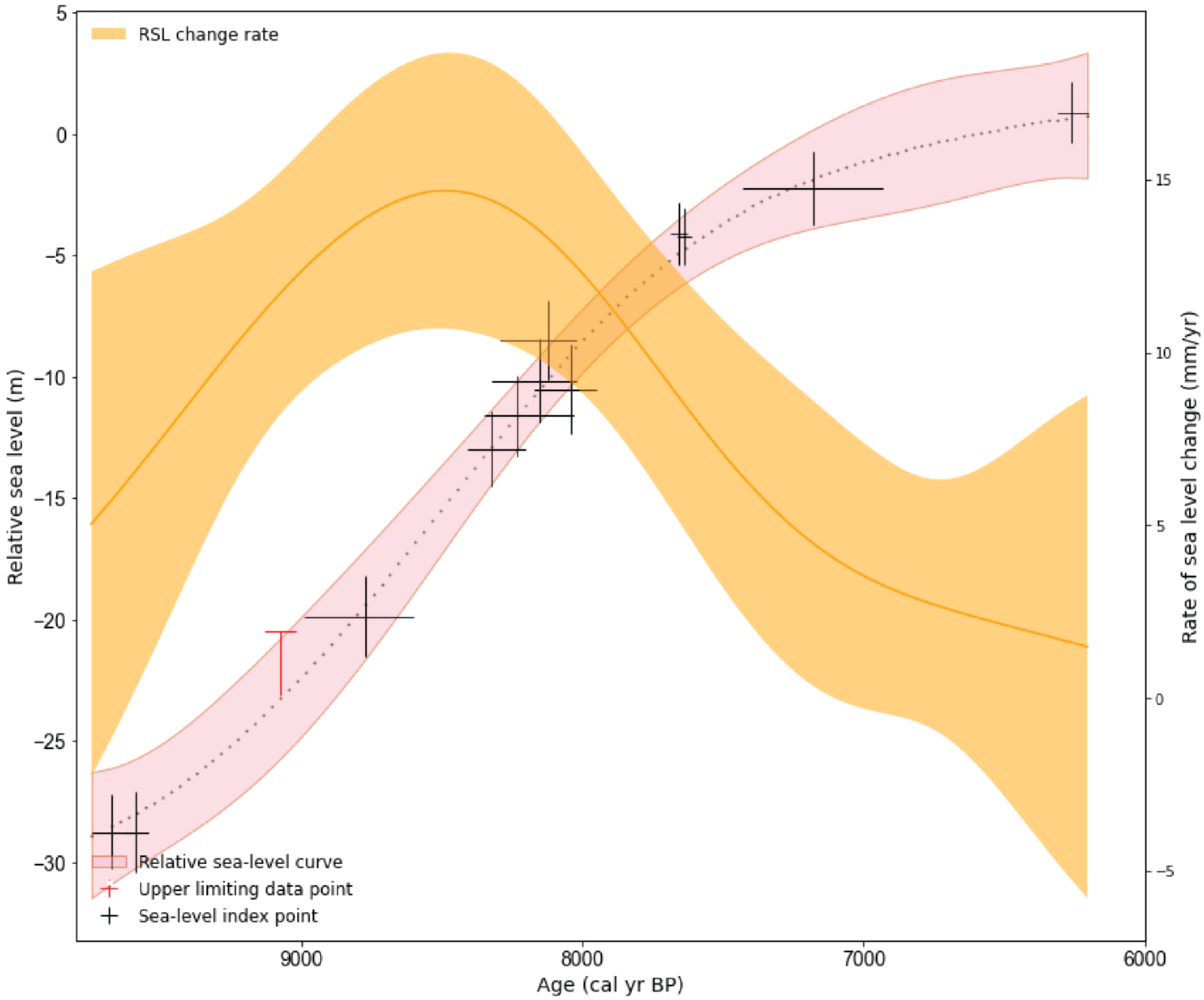

Figure 7 Plot showing the SLIPS, upper limiting data, estimated RSL, and the rate of change of RSL between 6.5 -10 ka in the Yangtze delta

(2015). The record consists of 12 SLIPs and one upper LDP, covering the time from ~10 ka to ~6.2 ka. Dated plant fragments collected from saltmarsh peat and tidal flats have been used as SLIPs, while the upper LDP consists of plant fragments from supratidal flat deposits. These publications provide detailed facies descriptions and other information about sample depth. We reinterpreted the IR for the SLIPs to be more conservative (MTL to HAT) than in the original publications where all the indicators had narrower ranges as their indicative meanings. The RSL record for this area covers the entire time period of interest 9-7 ka, with SLIPs present throughout this time period.

Key features from the four RSL records

In three of the four study areas discussed in the above section, namely the Rhine-Meuse Delta, Yangtze Delta and Malay Peninsula, we see the "peak" RSL rise rates around 9 to 8.5 ka. In these RSL records, we notice an increase in RSL rise rate from 9 to 8.5 ka, followed by a constant rate of RSL change until 7.5 ka and a decrease between 7.5 and 7 ka. In case of the Mississippi Delta, an increase in RSL rate is seen throughout our time-period of interest.

1.6 Glacial isostatic adjustment modeling

Predictions of past RSL changes for the four study areas have been generated using a GIA model. To run GIA models several components are needed: a suitable ice history (Argus et al., 2014; Peltier, 2004; Tarasov et al., 2012), a sea-level equation-solving algorithm that ensures proper redistribution of the meltwater (Farrell and Clark, 1976; Mitrovica and Milne, 2003), and an earth rheology model that constrains the isostatic response of the earth surface to glacial loading/unloading

(Milne and Shennan, 2013; Peltier, 1974; Whitehouse, 2018). Using various combinations of seven Earth models and 156 possible NAIS) and AIS ice model configurations (discussed below), a total of 1092 modeled RSL histories are tested and compared against the RSL history of each respective study area. The RSL history has been generated individually for the multiple NAIS and AIS models, using different Earth models. Then, for every Earth model scenario, the two sets of RSL curves, one generated using all the combinations of NAIS and the other using all AIS models, have been added to create the modeled RSL histories for the specific study area.

6.1 Earth Models

Table 1 The different Earth model parameters used for the glacial isostatic adjustment.

Earth model Parameters	Values tested		
Lithospheric thickness (LT) (km)	46	71	96
Upper mantle viscosity (UMV) (x10^{21} Pa s)	0.1	0.5	1
Lower mantle viscosity (LMV) (x10^{21} Pa s)	1	10	70

We assume a spherically symmetric Maxwell viscoelastic Earth model in which the viscosity structure is defined by a 3-shell structure: a thin outer region of very high viscosity (~10^{40} Pas) to simulate an elastic lithosphere (different thicknesses of this layer were considered (Table 1), an upper mantle region of uniform viscosity extending form the base of the lithosphere to 670 km depth, and a uniform viscosity lower mantle region extending from 670 km depth to the core-mantle boundary (~2900 km depth). We tested seven different combinations of lithospheric thickness, and upper and lower mantle viscosity, using three different values for each of the variables (Table 1). These different Earth model configurations were selected to span plausible uncertainty in these values as inferred from the relevant literature [for e.g. (Bassett et al., 2005; Lambeck et al., 2014a; Milne and Peros, 2013; Stocchi and Spada, 2009; Whitehouse et al., 2012a; Whitehouse et al., 2012b)].

For the four study areas, the optimum Earth model parameters were chosen after calculating misfits between the RSL rates determined from the Bayesian modeling of RSL records, henceforth referred to as the data-derived RSL rates (dRSLr), to RSL rates calculated from the GIA model derived RSL predictions, henceforth referred to as model-derived RSL rates (mRSLr) for the different Earth models using the χ^2 value (Eq. 1.1). The misfit between the RSL rise rate computed from these models for the specific location and time step and the RSL rate from the data is calculated using the relationship following similar relationships used by Love et al. (2016) and Milne and Peros (2013):

$$\chi^2 = \frac{1}{N}\sum_{i=1}^{N}\left[\frac{dRSLr - mRSLr}{\sigma_i}\right]^2$$

……….Equation 1.1

where χ^2 is the value of the data-model fit , N is the total number of time steps covering the dRSLr calculated from the available SLIPs for a given study

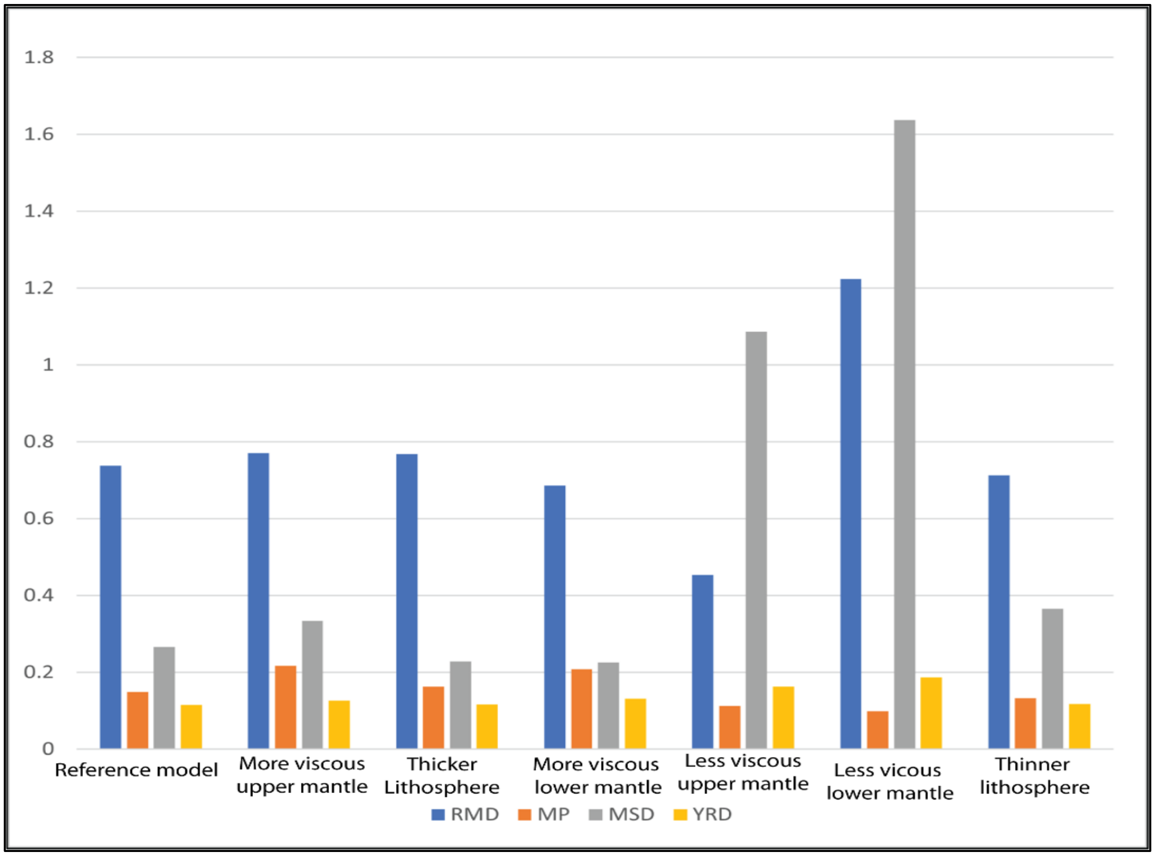

Figure 8 Data-model misfit calculation for the different earth model configuration shown in Table 1 for the different study areas: Rhine-Meuse Delta (blue bars), Malay Peninsula (orange bars), Mississippi delta (grey bars), Yangtze delta (yellow bars).

area, dRSLr and mRSLr are the observed and predicted RSL rates for the ith time step and σ_i is the rate uncertainty in the observed RSL rate value. An important distinction between this analysis and the χ^2 analysis done by earlier studies (e.g., Milne and Peros, 2013) is that instead of directly using SLIPs to compare with the GIA-modeled past RSL elevations, we use the rate of RSL rise. So, in other words, N is defined 4 (total time period, 2000 years, divided by the time increment used, 500 years) by us for this 2000-year time interval.

Seven model runs were computed using the LT, UMV, and LMV values from Table 1 for each of the four study areas (Fig 8). In case of the Malay Peninsula and the

Yangtze Delta, no significant difference was noted amongst the different Earth model configurations. However, in case of the Rhine-Meuse Delta and the Mississippi Delta, the Earth model with a less viscous lower mantle shows a high data-model misfit. Even though the earth model with a less viscous upper mantle has the lowest χ^2, we did not use that model because it does not work well for the Mississippi Delta. We acknowledge that there is some sensitivity to earth structure, particularly at the sites closest to former ice margins. Therefore, by considering different Earth model parameter sets, we are accommodating this uncertainty in the model results. We wanted to isolate one model that works moderately well for all the four study areas. For the subsequent data-model comparison an Earth model with a 71 km thick lithosphere, an upper mantle viscosity of 0.5×10^{21} Pa s and a lower mantle viscosity of 10×10^{22} Pa s has been used, which has a low χ^2 in the Mississippi Delta, the Yangtze Delta and the Malay Peninsula and works comparatively well in Rhine-Meuse Delta.

6.2 Ice models

Twenty-five different ice models have been used; 13 of these are NAIS models (Tarasov et al., 2012) and 12 are AIS models (Lecavalier and Tarasov, manuscript in preparation) (Fig 9). The NAIS suite of models is selected from a larger set of over 50,000 model runs, discussed in detail in Tarasov et al. (2012) to capture a high variance set of plausible ice histories for the 9-7 ka time period (Fig 9). All the NAIS and AIS ice sheet chronologies are output from a glacial systems model and so the thickness distributions are consistent with the specific boundary conditions (e.g., climate forcing) and incorporated ice physics (see Tarasov et al., 2012 and Lecavalier and Tarasov for further information). These models were calibrated against a large set of mostly near-field/ice margin RSL data, present-day surface uplift data as well as deglacial ice-margin chronologies and strandline observations. However, a number of unknown factors like ice sheet thickness, basal velocity, ice temperature fields, ice margin chronology, and Earth rheology add to the uncertainty for these models (Tarasov et al., 2012). Since these are regional ice sheet models, outside of North America and Antarctica, we used ICE-5G (Peltier, 2004) as the background model to ensure that the GIA signal due to other ice sheets is included in the model output.. Even though available ice models like ICE-5G can be manually made to fit RSL data (e.g., (Charbit et al., 2007; Marshall et al., 2000)), these models lack constraints like climate chronologies and glaciological self-consistency related to factors like ice deformation physics (Tarasov et al., 2012). The ice models used here consider both glaciological and geophysical constraints.

1.7 Data-Model comparison

7.1 Method

The data-model comparison was done in four steps. In this study, we are comparing the RSL history from vastly different areas around the world and instead of comparing the

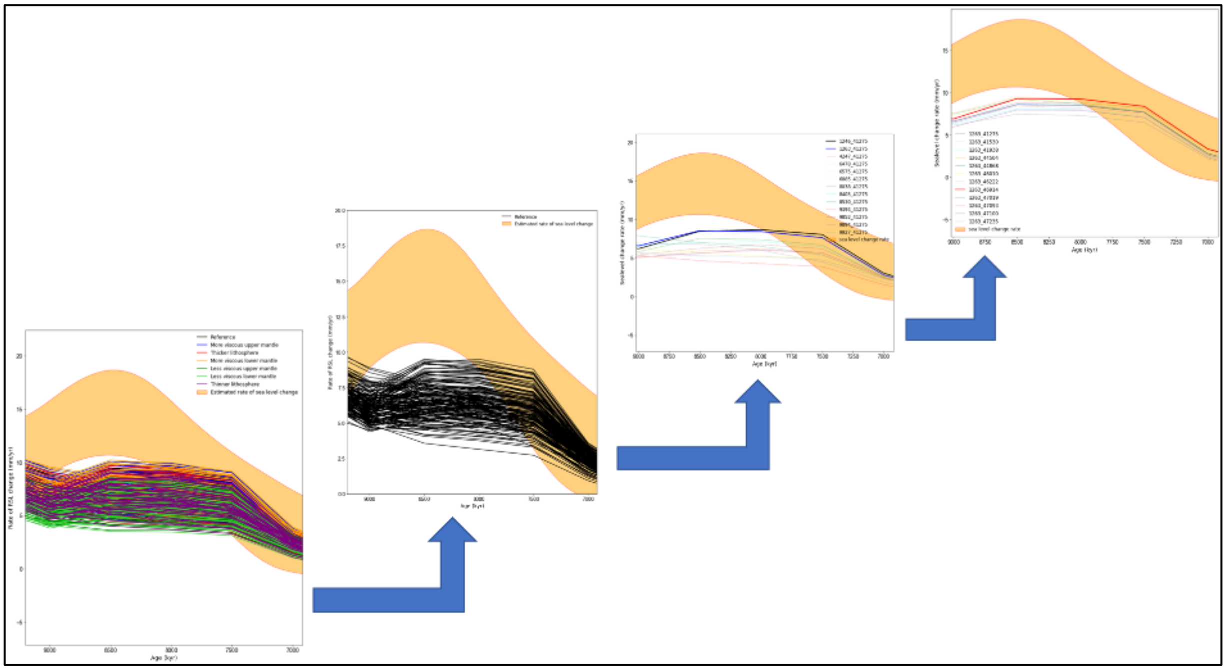

Figure 9 Steps for data-model comparison between RSL rates calculated from sea-level indicators and those from GIA models.

actual RSL elevation data, which can show major contrasts depending on local factors contributing to RSL change, the RSL rates calculated from the Bayesian modeling of RSL records for the study areas, dRSLr, have been compared with RSL rates calculated from the GIA model derived RSL predictions, mRSLr.

At first, for every study area all 1092 mRSLr were plotted with the dRSLr, with its 95% confidence interval to understand the overall (mis)fit between the data and the models. Then the spread of the mRSLr was narrowed down to the 156 ice model combinations and the reference Earth model. In the next step to identify the best-fit

NAIS model, the models were run with the reference Earth model, the reference AIS model and the entire spread of 13 NAIS models. In the next step, the mRSLr was calculated using all the AIS models and the best-fit NAIS model to pinpoint the combined ice model that has the closest fit to the dRSLr (Fig 10).

.

7.2 Ice sheet fingerprints in the study areas

Each combination of ice models has a unique fingerprint, which in conjunction with the data constraints can guide us to the most plausible solution. To identify the dominant ice sheet fingerprint in the different study areas, 25 individual GIA models, for each of the 13 NAIS and 12 AIS ice models and one reference Earth model were run to produce RSL predictions. As discussed above, 13 NAIS models, with the background ICE-5G model used for the other ice sheets, and 12 AIS models, with the ICE-5G model as background were used. Fig 11 shows the results of this analysis. In every study area, the mRSLr plots derived from the GIA models using NAIS models matched the dRSLr better than the ones using AIS models. In the Asian study areas and the Rhine-Meuse Delta (Fig 3b, c and d), the NAIS models have a better spread and are closer to describing the RSLR history compared to that shown by the AIS models. In the MSD, however, the AIS and NAIS ice models have a comparatively similar spread and compare well with the dSLRr. The dominant ice sheet signal for the four study areas between 9-7 ka comes from the NAIS, with the AIS signal only contributing a small part of the total RSLR in the Yangtze Delta, Malay Peninsula and Rhine-Meuse Delta.

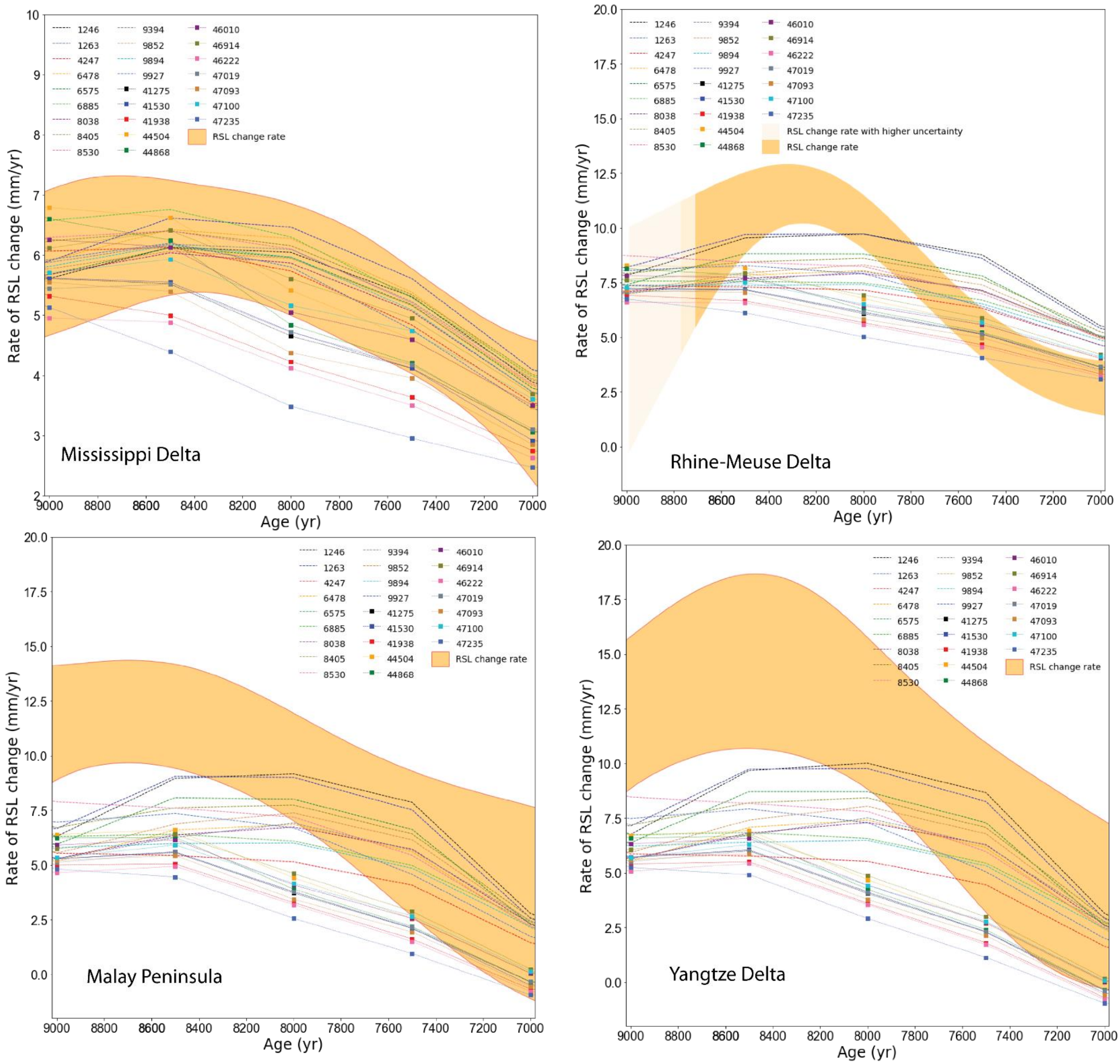

Figure 10 Comparison of the NAIS and the AIS signals in the four study areas, namely, Mississippi Delta, Rhine-Meuse Delta, Malay Peninsula and Yangtze Delta. The dotted lines represent RSLR rates calculated from GIA models that only use NAIS models and dotted lines with squares represent the same with only AIS models.

However, in case of MSD, even though the dominant signal is still the NAIS, the proportion of AIS signal is comparatively larger than the other three areas.

7.3 Results

The main focus of the data-model comparison is on the shapes of the dRSLr and mRSLr curves, instead of the particular values at different time steps. A number of mRSLr curves might match the values of the dRSLr curves at specific time steps, yet they may still fail to portray the trend of the full RSLR history in the study areas between 9-7 ka. For example, in Fig 11c and d, we can see that there are two distinct sets of mRSLr curves, one consistently showing slower rates relative to other model curves (an example being NAIS configuration 8530), and the other set showing a maximum between 8.5-7.5 ka, and subsequently slowing down (as shown by NAIS configuration 1263 and others). The shape of the dRSLr curve, with an increased rate between 9-8 ka, and subsequent slower rate of RSL change, provides a better match with the second set of the mRSLr curves shown by the likes of ice model 1263.

Yangtze Delta

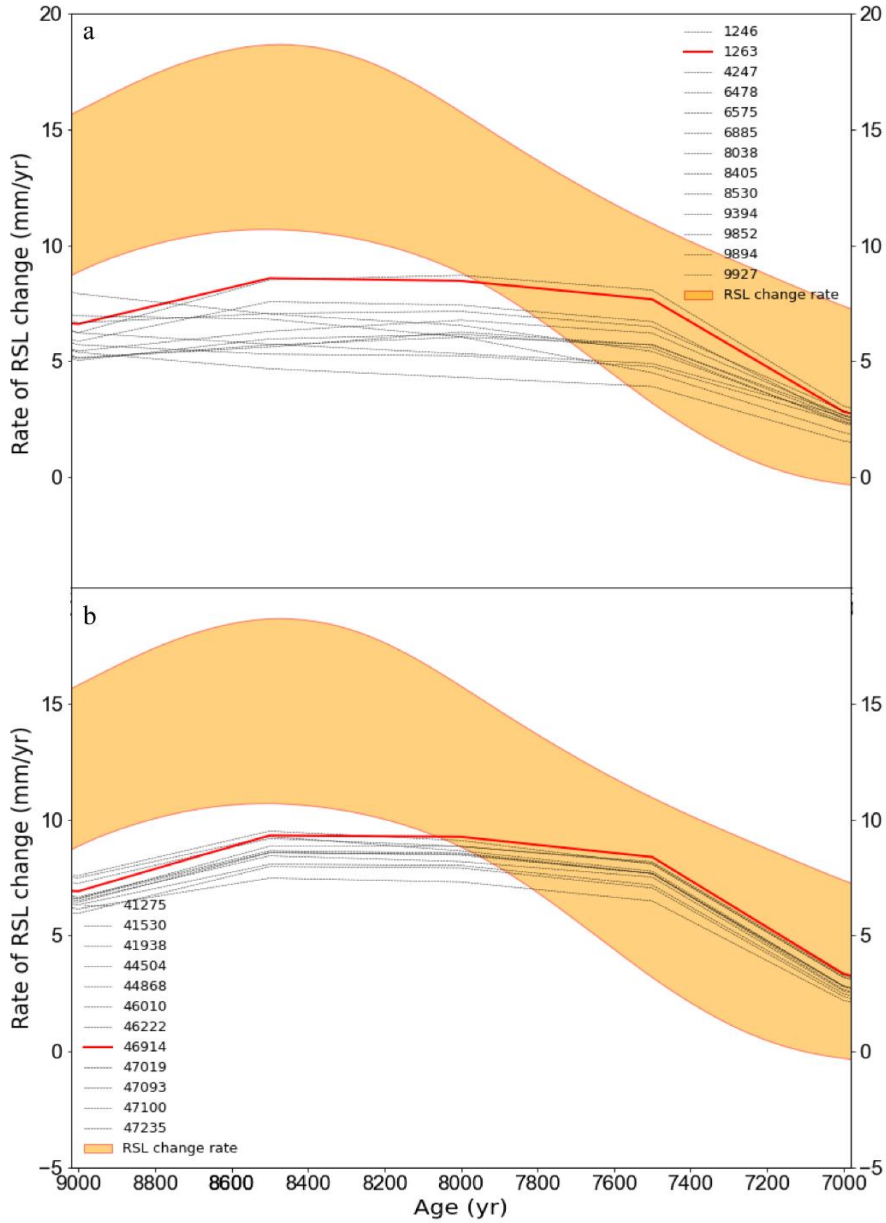

Figure 11 Data-model comparison for the Yangtze Delta study area. A. comparison between data derived rate of RSL change (dRSLr) to rates calculated from GIA modeling (mRSLr) using different NAIS models with one AIS model and the reference Earth model. B. Comparison of GIA models using the best-fit NAIS model with different AIS models and the reference Earth model. The red line signifies the best-fit model.

In the Yangtze Delta, the model predictions differ substantially from the dRSLr. The second set of mRSLr curves shows an increase in RSL rise rate from 9 to 8.5 ka, followed by a constant rate of RSL change until 7.5 ka and a decrease between 7.5 and 7 ka. This set of curves matches the trend of the dRSLr plot, however, all models underpredict the rate of RSL change between 9-8 ka by at least 5 mm/yr. After 8 ka, as RSL approaches present-day sea level, the models predict the rate of RSL change in this area correctly. We identify the best-fit combination of NAIS and AIS models, shown in red in Fig 4, but even this scenario consistently underpredicts the rate of RSL change between 9 and 8 ka. When this combination of ice models is traced back to Fig. 2, which shows the sea-level equivalent of all the ice models, it appears that the best-fit NAIS ice model is the one with the maximum amount of meltwater (model #1263). In case of the AIS ice models (Fig 2b), the best-fit model is #46914, also one of the models producing higher amounts of meltwater. However, NAIS remains a far larger contributor to RSLR compared to AIS, so the NAIS ice models with a higher rate of production of melt water between 9-8 ka are the best avenue towards a better data-model fit.

Malay Peninsula

In the Malay Peninsula, the data-model comparison yields similar results as in the Yangtze Delta. The mRSLr plots, with an increase in the rate of RSL change between 9-8 ka, followed by a constant rate of change until 7.5 ka, and a gradual decrease after that,

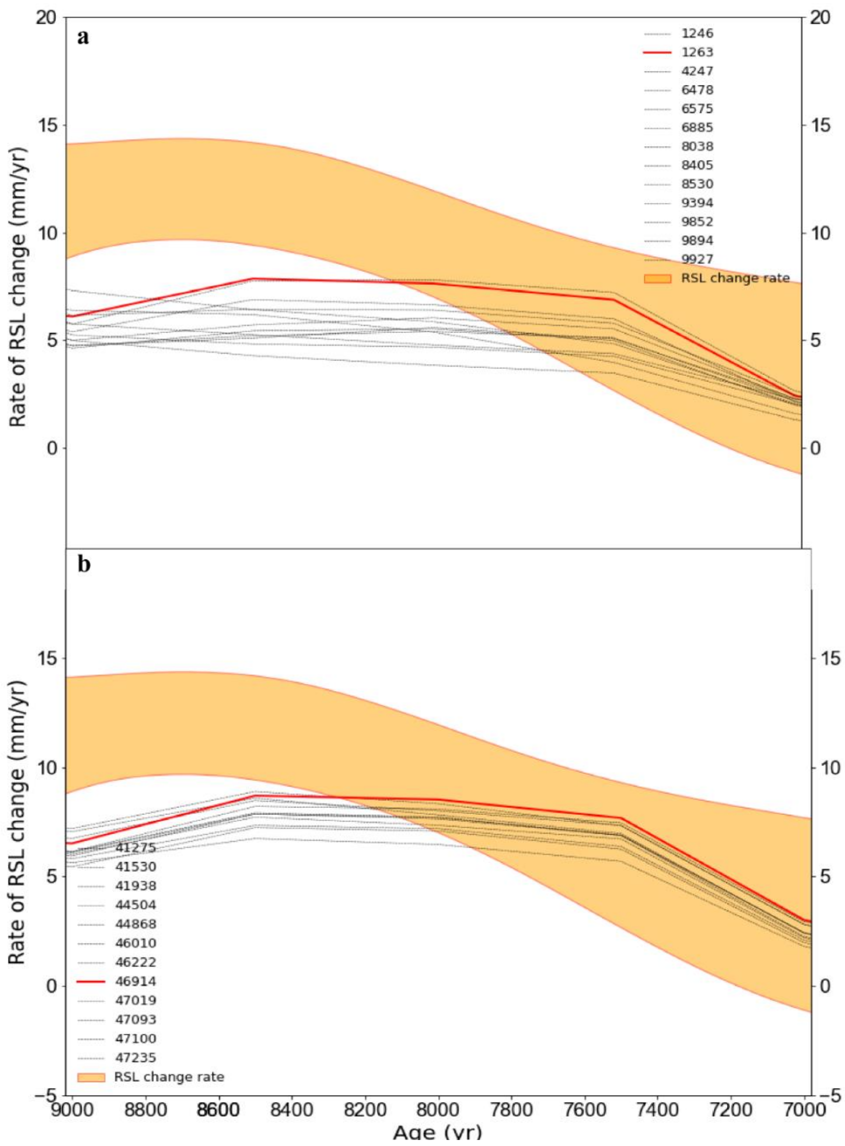

Figure 12 Data model comparison in the Malay Peninsula area. The top figure shows the comparison between data derived rate of RSL change to that of calculated from GIA models using different NAIS models with one AIS model and the 'reference' earth model. The bottom figure shows the same with the GIA models using the best-fit NAIS model with different AIS models and the 'reference' earth model. The grey box denotes the time-period 9-8 ka where the models underpredict the rate of RSL change. The red line signifies the best-fit model.

match the dRSLr trend. However, similar to the situation in the Yangtze Delta, all model scenarios underpredict the rate of RSL change as calculated from the RSL data by ~5 mm/yr at its maximum. In the Malay Peninsula, the data and model start to merge at around 8 ka. The combination of NAIS and AIS models that performs best in the Yangtze Delta also shows the best fit in the Malay Peninsula.

Rhine-Meuse Delta

In the Rhine-Meuse Delta, the dRSLr is very well-constrained for the time-period between 7 and 8.7 ka. The uncertainty in the dRSLr increases past 8.5 ka and we should consider this issue while carrying out the data-model comparison. The models underpredict the rate of RSL change in this area between 9-8 ka, but the difference between the data and

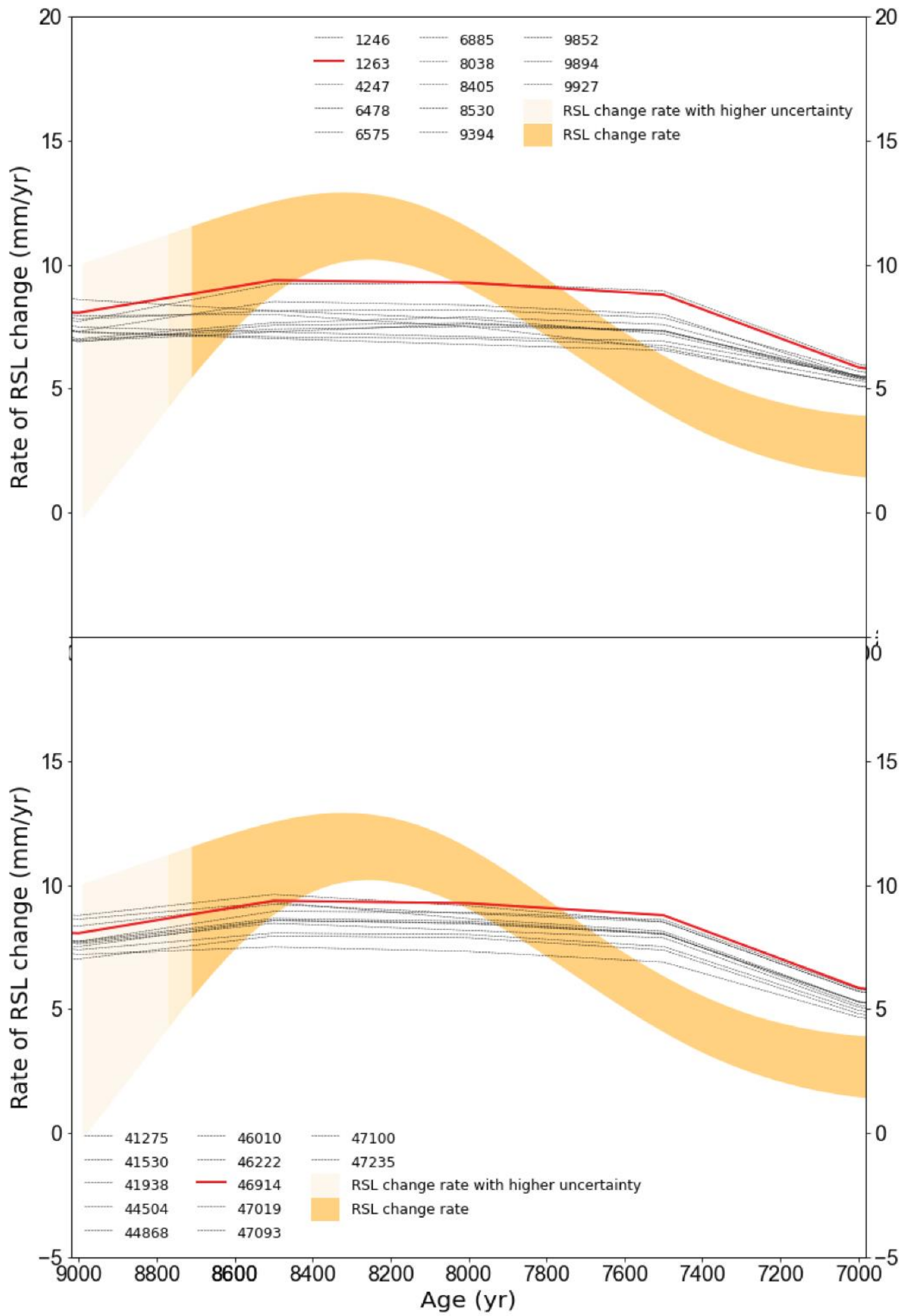

Figure 13 Data model comparison in the Rhine-Meuse delta. The top figure shows the comparison between data derived rate of RSL change to that of calculated from GIA models using different NAIS models with one AIS model and the 'reference' earth model. The bottom figure shows the same with the GIA models using the best-fit NAIS model with different AIS models and the 'reference' earth model. The red line signifies the best-fit model.

the models is smaller than that seen in the Asian study areas, with the best-fit model plotting just beneath the dRSLr curve. However, the models also overpredict the rate of RSL change in this area between 7.7-7 ka, which can be attributed to the fact that this study area is closer to an ice margin. On testing the combination of NAIS and AIS models that produce the best match in the Yangtze Delta and the Malay Peninsula, it is noted that the same ice model combination gives the most promising fit in the Rhine-Meuse Delta.

Mississippi Delta

The Mississippi Delta is the only study area amongst the four where the NAIS signal did not dominate during 9-7 ka (Fig 15), as seen by the greater spread of the RSLR rate calculated from the AIS models. This is the only study area where both the NAIS and AIS signals are almost equally large. In the three other study areas, the NAIS signal dominates (Fig 11). Here the dSLRr and mRSLr plots show comparable results. Some ice model combinations in this part of the world are able to predict the rate of RSL change during the entire 9-7 ka, with a number of the combinations plotting well below the observation envelope. The AIS and NAIS model combination, which is the best-fit model for the other three locations, largely fits the data here as seen in Fig 14.

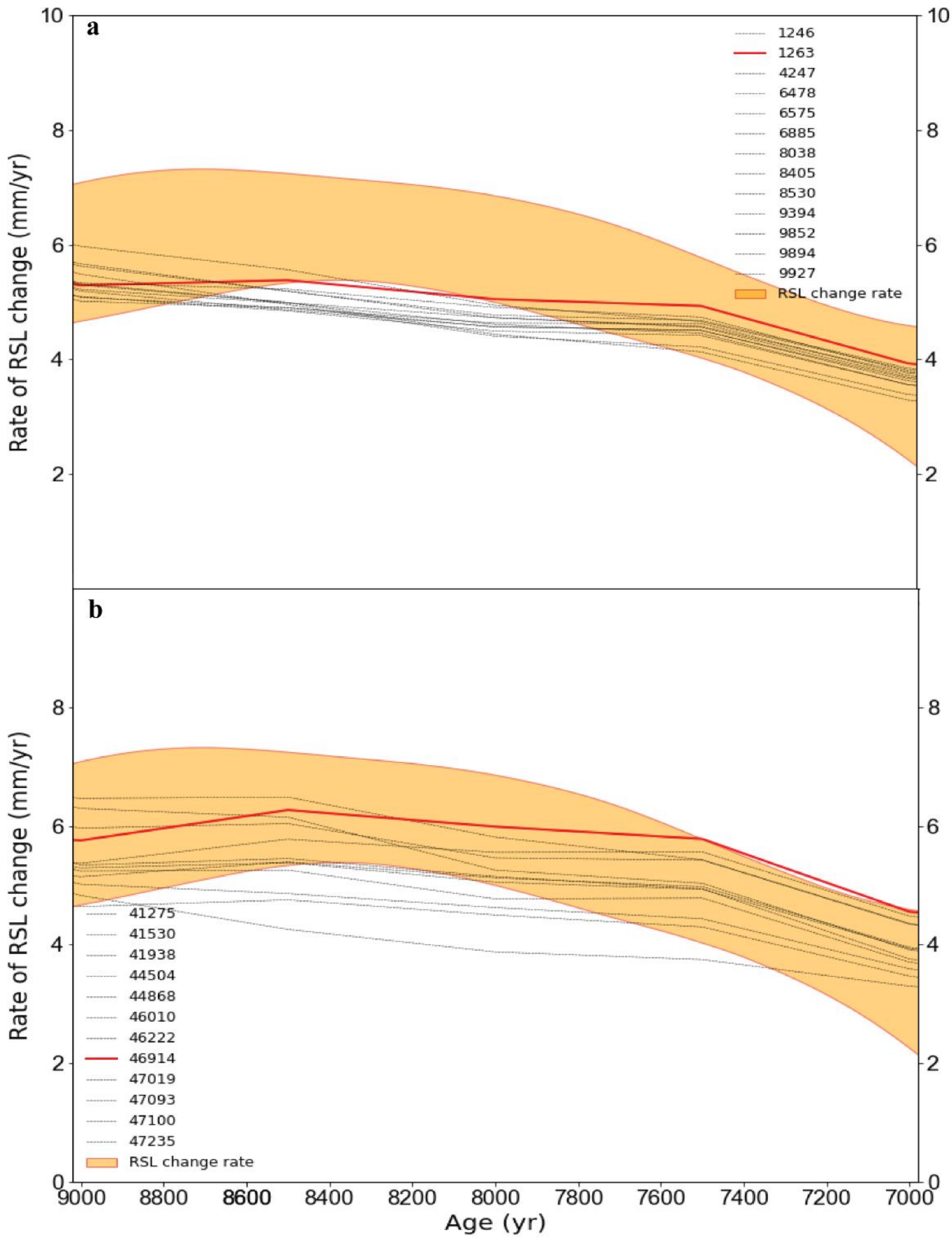

Figure 14 Data model comparison in the Mississippi delta. The top figure shows the comparison between data derived rate of RSL change to that of calculated from GIA models using different NAIS models with one AIS model and the 'reference' earth model. The bottom figure shows the same with the GIA models using the best-fit NAIS model with different AIS models and the 'reference' earth model. The red line signifies the best-fit model.

Introducing a best-fit NAIS model

The analysis of RSL records from the four distinctly different geographic locations, and multiple GIA model runs using different ice models brings to light major differences in RSLR rates. At all sites except Mississippi, rates in the early part of the time window (~9-8 ka) are too low by ~5 mm/yr. The only way to address this misfit is by increasing the contribution from the NAIS (so that the models still fit the dRSLr from the Mississippi delta).

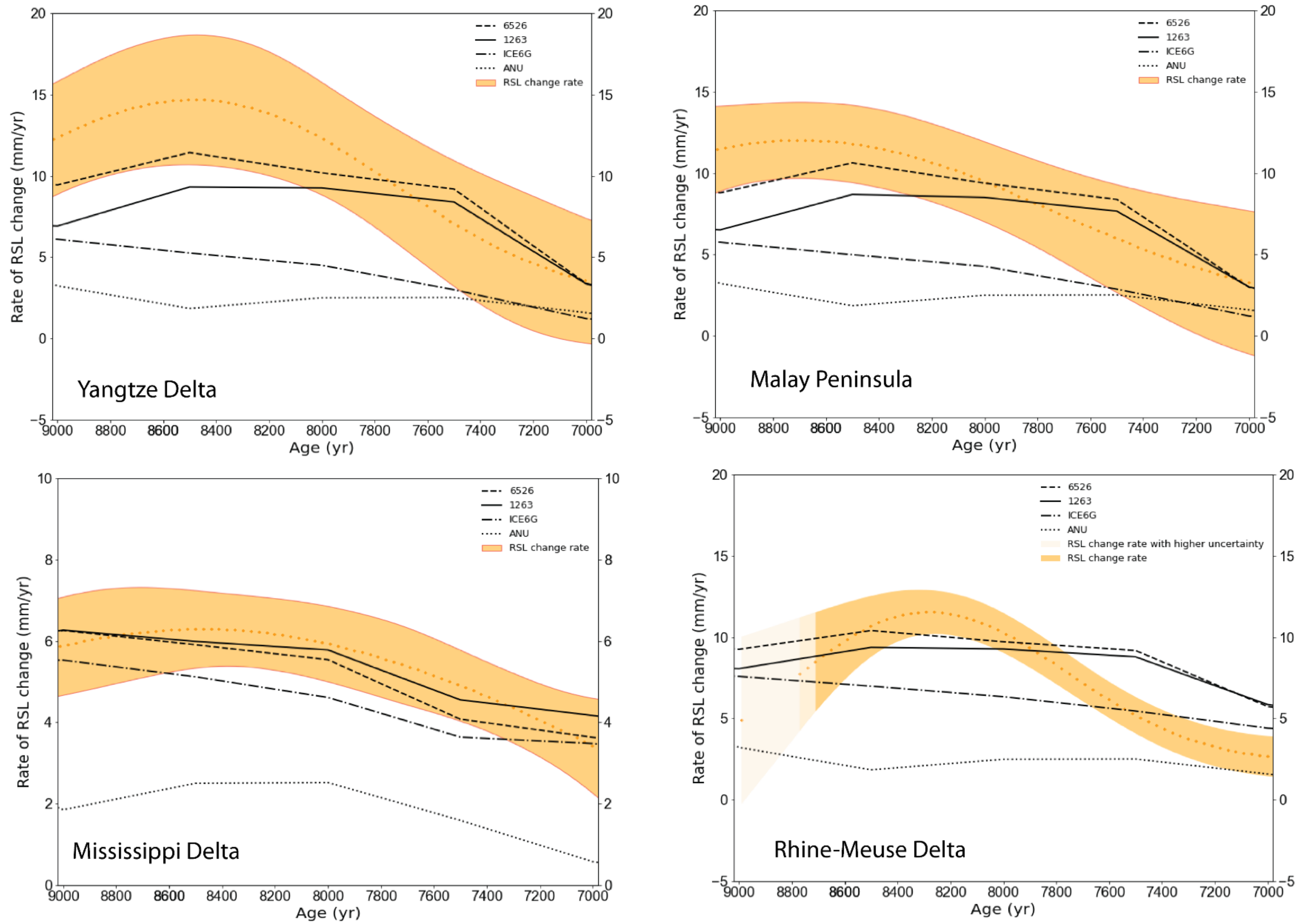

Figure 15 Comparison between two different NAIS models (1263 in black solid line, the best-fit NAIS model (6526) in black dashed line, ICE6G in black dots and dashed line), and ANU in black dotted line using one preferred AIS model (46914) and earth model in the four study areas as mentioned in the panels.

Using a newly developed ice model that aims to produce a better fit with the data an ice-model configuration (6526), henceforth referred to as the best-fit NAIS model (Fig 8 and 15), provides an estimate of the amount of meltwater required to fit the dRSLr seen in all the four study areas. This is only a minimum estimation of the excess meltwater that is believed to be produced from NAIS between 9-7 ka, i.e., a conservative number. This can be attested by the fit of this mRSLr with the lowest part of the error envelope for the dRSLr. In this ice model the sea-level equivalent (SLE) produced from NAIS is at least 14 m between 9-7 ka, as compared to ~9.5 ± 2 m and ~6 m from the average Tarasov et al. (2012) models and ICE-6G (Peltier et al., 2015; Stuhne and Peltier, 2017) (Fig 18). ICE-6G plots lower than the dRSLr and shows a completely different trend compared to the best-fit NAIS reconstruction and 1263 reconstruction in all the study areas except the Mississippi Delta (Fig 15). Compared to these ice sheet reconstructions, the present study shows a deficit of at least ~5 m SLE, i.e., almost equivalent to the SLE of an ice sheet the size of the present-day Greenland Ice Sheet. Such an amount of excess freshwater, when added to the North Atlantic system, would have had a number of implications for our current understanding of relative sea level rise (RSLR) and its effect on the other elements of the climate system between 9 and 7 ka. We have seen that the model consistently underpredicts the observation for time periods older than 8 ka. So, we also compared the meltwater production from the different ice sheet models and found that the bulk of the difference in the amount of meltwater actually stems from the time period 9-8 ka, the part of the record which has consistently being underpredicted by models from Tarasov et al. (2012) (Fig 16). On the other hand, the best-fit AIS model used in the present study, 46914, yields ~3.7 m SLE during this 2000 yr period (Fig 16). The average of the Lecavalier and Tarasov (in prep.) ice models produces 2 ± 3 m of SLE for the same time period, while ICE-6G produces <1 m (Argus et al., 2014).

1.8 Discussion

Partitioning NAIS and AIS meltwater

According to the present study, the amount of meltwater produced from NAIS between 9-7 ka (>14 m) was about four times that originating from the AIS (3.7 m). The proportion of meltwater partitioning becomes even larger when we just concentrate on the time period between 9-8 ka, where we see a consistent mismatch between observation and model. Between 9-8 ka, according to this study, NAIS produced ~10 m of SLE compared to ~2 m from AIS, driving the meltwater partitioning between the two ice sheets, i.e. five times more. This suggests that NAIS was by far the largest contributor to global sea level rise during this time [for e.g. (Carlson et al., 2008; Nichols et al., 2019; Peltier et al., 2015; Whitehouse et al., 2012a)]. Combining the NAIS component of the widely used ICE-6G reconstruction with the best-fit AIS reconstruction in the present study, we show that the NAIS meltwater contribution from ICE-6G underpredicts the RSL rise rates in all four study areas (Fig 17). ICE-6G and ICE-5G have thinner ice-sheets for this time period compared to other ice models like Licciardi et al. (1998), which shows a NAIS contribution of 14 m between 9-7 ka, and ANU model (Lambeck et al., 2014). Commonly used models like ICE-6G, ICE-5G, and the average Tarasov et al. (2012) models predicts a comparatively lower amount of meltwater to the oceans between 9-7 ka, whereas this study presents evidence that during the same time period, a minimum of ~18 m of SLE was contributed to the RSL rise around the global coasts, and the bulk of it coming from the NAIS (a minimum of 14 m) (Fig 18).

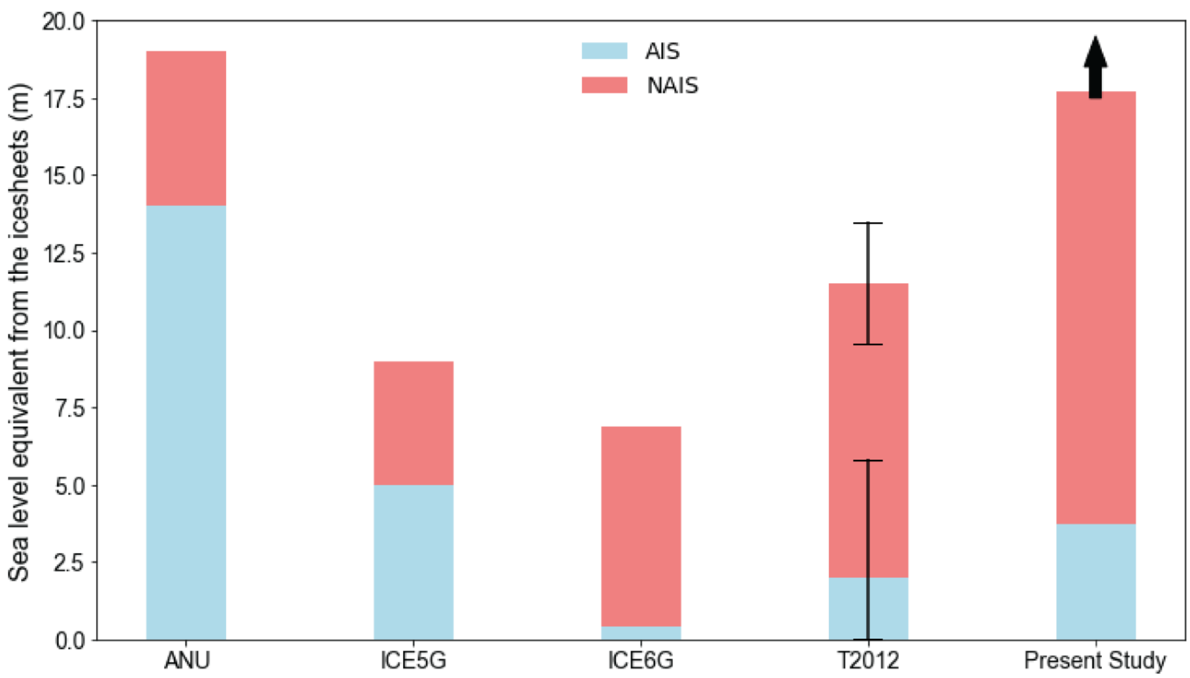

Figure 16 Comparison of the proportion of NAIS vs AIS sea level equivalent contribution to global sea level rise for the time period 9-7 ka between the different ice sheet models ANU (Lambeck et al., 2017; Lambeck et al., 2014a), ICE-5G ((Peltier, 2004), ICE-6G (Argus et al., 2014; Stuhne and Peltier, 2017), average NAIS models from Tarasov et al.

(2012), mentioned here as T2012, and Lecavalier and Tarasov(manuscript in prep.) and the present study. The AIS component for the ANU model was calculated by subtracting the NAIS component as reported in Lambeck et al. (2017) from the total sea level equivalent sea level change reported in Lambeck et al. (2014) for the 9-7 ka time period. The vertical black lines for T2012 is the 1б standard deviation for the different configurations of the NAIS models reported in Tarasov et al. (2012). The arrow at the top of the bars represents that the estimates for the portioning of AIS vs NAIS sea level equivalents are only a minimum constraint and the actual ice melt volume might have been higher.

However, the difference lies not only in the amount of meltwater, but also in the rate of NAIS melting through this time period. Compared to an average SLR rate of ~5 mm/yr from the NAIS between 9-8 ka (Carlson et al., 2008), the best-fit NAIS model used here yields a SLR rate of ~10 mm/yr during the same time period. Our best-fit AIS model yields a rate of ~2 mm/yr of SLR rise between 9-8 ka. According to this calculation, significantly more meltwater was added to the North Atlantic Ocean from a rapidly melting NAIS during the early Holocene. Since the best-fit NAIS model only fits the lower bounds of the data in the Asian study areas, we propose these values as a minimum estimate for the amount of meltwater that must have been released from the NAIS during 9-8 ka.

The 'missing ice problem' at the beginning of the deglaciation (for eg,.(Andrews, 1992; Clark and Tarasov, 2014; Simms et al., 2019) has been a well-documented question in the paleo sea level community, but the data-model comparison carried out during this work has brought into light a that there was a larger amount of ice melting from NAIS at the very end of the deglaciation as well. The estimates of SLR during the post-LGM deglaciation and that of the total ice melted during this same time shows a prominent offset, with the 'missing ice' accounting for about 18.1 ± 9.6 m of GMSL rise since the LGM [for eg., (Clark and Tarasov, 2014; Simms et al., 2019)]. A number of studies have sought to estimate the volume of LGM AIS using both geological constrains [for e.g. (Clark et al., 2009)] as well as numerical modeling (for e.g. (Austermann et al., 2013; Golledge et al., 2013; Ivins et al., 2013; Whitehouse et al., 2012b). They typically yield lower values for the AIS contribution as well (~9.9 ± 1.7 m SLE) (Simms et al., 2019). ICE-6G and ICE-5G show a post-glacial net loss of mass of 13.6 and 17.6 m, respectively, which are higher estimates, more so for ICE5G, when compared to the other models mentioned earlier (Peltier, 2004; Peltier et al., 2015).

The ice melt from NAIS has been underestimated by at least ~5 m for the time period between 9-8 ka (Fig 16). This lack of knowledge about the precise amount of ice melt and the rate at which this meltwater was being added to the ocean during 9-7 ka has potential implications for the global SL history during most of the last deglaciation and begs us to question our understanding for everything that must have come before 9 ka as well. To address this issue, which has numerous implications including projections of future SLR, we need many more high-resolution RSL records from different parts of the world. However, published high resolution RSL records are difficult to find in the Southern Hemisphere, and future work needs to be concentrated in the pursuit of collecting these records globally, with a special focus on locations from the Southern Hemisphere to discern the AIS melt history and its effect on global SLR over the last deglaciation.

The effects of higher NAIS meltwater contribution on the 8.2 ka event

Abrupt climate change, like the 8.2 ka event which is the most prominent abrupt North American climate change during the Holocene, has been of interest to the paleoclimate and paleo sea level community in connection to its potential occurrence in a future warming world (Alley et al., 2003; Barber et al., 1999). The sea-level jump around 8.2 ka has been detected in a number of locations around the world, including the Mississippi Delta (Li et al., 2012; Törnqvist et al., 2004a), the Rhine-Meuse Delta (Hijma and Cohen, 2010), southwest Scotland (Lawrence et al., 2016), Asia (Hori and Saito, 2007) and in Guatemala (Obrist-Farner et al., 2022), but with variable amounts of RSLR during this event. The RSL jumps in the Rhine-Meuse delta and the Mississippi Delta have been recorded to be 3 ± 1.2 m, with a corresponding drainage volume of ~6-15 x 10^{14} m^3 (Hijma and Cohen, 2010) and 1.5 ± 0.7 m with a drainage volume of ~3-8 x 10^{14} m^3 (Li et al., 2012) respectively. The catastrophic collapse of an ice dam over Hudson Bay leading to the final drainage of proglacial Lakes Agassiz and Ojibway (LAO) into the Labrador Sea (Barber et al., 1999) resulted in the introduction of a large freshwater flux (FWF) into the North Atlantic Ocean. Evidence shows that the North Atlantic Ocean was undergoing preconditioning for this abrupt climate change by the way of additional FWF, with the draining of the LAO being the last straw (Carlson et al., 2009a; Carlson et al., 2008; Clark et al., 2001; Gregoire et al., 2012).

Since the estimated total volume of LAO (1.63×10^{14} m^3) (Kendall et al., 2008; Leverington et al., 2002; Törnqvist and Hijma, 2012) during the final episode of drainage is less than the estimates of the freshwater volume needed for the corresponding RSL rise, two other freshwater sources have been proposed for the 8.2 ka event - the change in continental North American routing (Carlson et al., 2009b; Clark et al., 2001), and the melting and retreat of NAIS (Carlson et al., 2008; Ullman et al., 2016). The amount of freshwater from the melting of NAIS is not as well constrained as the first two sources and this study provides new constraints. Matero et al. (2017) and Gregoire et al. (2012) have suggested that the collapse of an ice saddle connecting the Labrador and Baffin domes of the NAIS over Hudson Bay was the reason behind the significant FWF in the North Atlantic Ocean. A larger amount of ice in the NAIS during 9-8 ka, in turn providing additional FWF to the North Atlantic, supports the idea of an ice saddle collapse during this time. This work also shows that the amount of RSLR during this time was larger than what could have been produced from the LAO (Li et al., 2012). Studying RSL change in areas far away from the LAO and NAIS like the Malay Peninsula and Yangtze Delta is integral to discerning the sea level rise signal of the 8.2 ka event which can in turn help us in estimating total volume of freshwater that was added to the North Atlantic between 9-8 ka.

Climate models have reached the same conclusion that using just the LAO meltwater volume as a one-time FWF around 8.2 ka cannot explain the sustained 8.2 ka cooling event, and the addition of other FWFs are needed to explain the continued cooling for 100-200 years that seen in proxy records [for e.g. (Aguiar et al., 2021; Matero et al., 2017; Wagner et al., 2013; Wiersma et al., 2006)]. The majority of the older climate models have used a meltwater flux of 2.5 Sv for ~0.5 yr during the collapse of LAO, with a small background meltwater flux (~0.17 Sv) following this event for some of these models (Morrill et al., 2013; Renssen et al., 2001; Wiersma et al., 2006; Wiersma and Jongma, 2010). Wagner et al. (2013) and Matero et al. (2017) used a small baseline FWF of 0.05 Sv prior to the collapse of LAO, based on prior reconstructions of NAIS. Aguiar et al. (2021) tested multiple model scenarios for the 8.2 ka event and compared them with $\delta^{18}O$ and SST records. They concluded that a background flux of 0.066 Sv (~5 m SLE) over 1000 years (9-8 ka), possibly from the melting NAIS, with an intensification over 130 years, which was possibly from the re-routing of the continental runoff and drainage of LAO, could explain the paleoproxy anomalies. We compare these modeled FWF values from the literature to the flux that would be generated from the melting of the average Tarasov et al. (2012) models and the best-fit NAIS model from the present study (Fig 17). The NAIS reconstruction from the present study contributes a considerably higher rate of freshwater to the North Atlantic around 8.5 ka, right before the LAO drainage event, compared to the FWF contribution from the average Tarasov et al. (2012) models, which are quite similar to the different modeled FWF reconstruction done by Aguiar et al. (2021), Matero et al. (2017) and Wagner et al. (2013).

A much higher FWF in the North Atlantic during this time period has far-reaching implications for the mechanisms and processes related to the 8.2 ka event, including the sensitivity of the Atlantic Meridional Overturning Circulation (AMOC) to FWF. The AMOC has been shown to weaken recently (Bakker et al., 2016; Caesar et al., 2018; Thornalley et al., 2018) due to the enhanced FWF from the Arctic and Nordic seas due to melting glaciers and thickened sea ice. However, the sensitivity of the amount of freshwater forcing on AMOC is a source of uncertainty in climate models (for e.g., (Sgubin et al., 2017; Swingedouw et al., 2007). The present study points towards the evidence that during interglacial times, the AMOC is not as sensitive to freshwater fluxes, as has been shown by past studies [for e.g., (Törnqvist and Hijma, 2012)]. During the 8.2 ka event, even with more meltwater available, the North Atlantic Ocean was merely being set up for the final push in the form of the ice saddle collapse and the LAO drainage. Melting of the Greenland Ice Sheet is one of the major responses to global warming, which will add fresh water in the ocean and might destabilize AMOC in the future (Cazenave, 2006; Fettweis et al., 2017; Shepherd et al., 2020). Incorporating an excess amount of meltwater, close to the SLE of the Greenland ice sheet, in climate modeling for the 8.2 ka event, can also help us in understanding and predicting future changes in the climate.

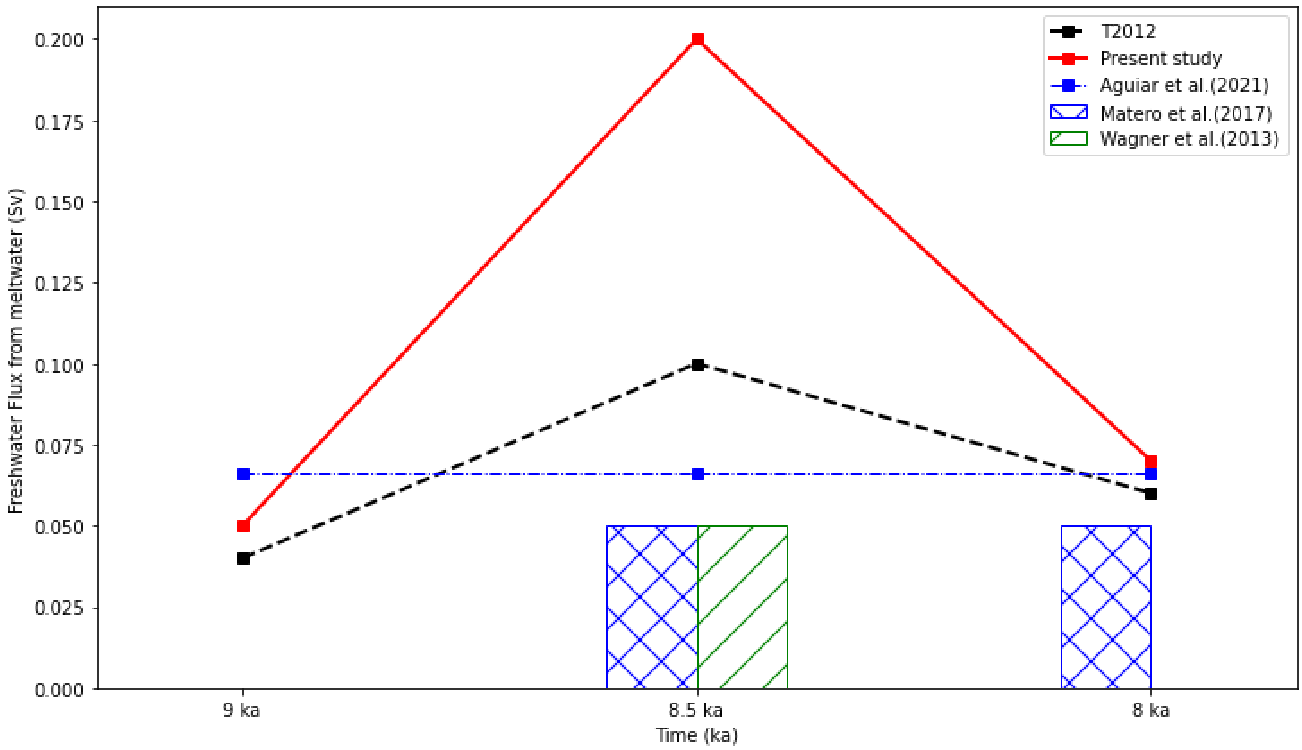

Figure 17 Comparison between the amount of freshwater flux that would have been generated from the different NAIS ice sheet reconstruction (present study which is the new NAIS model used here and Tarasov et al.,2012) and climate modeling studies which use a background freshwater flux from the NAIS melting in the North Atlantic Ocean before the 8.2 ka event (Aguiar et al., 2021; Matero et al., 2017; Wagner et al., 2013)

Aguiar, W., Meissner, K. J., Montenegro, A., Prado, L., Wainer, I., Carlson, A. E., and Mata, M. M., 2021, Magnitude of the 8.2 ka event freshwater forcing based on stable isotope modelling and comparison to future Greenland melting: Scientific reports, v. 11, no. 1, p. 1-10.

Albrecht, T., Winkelmann, R., and Levermann, A., 2020, Glacial-cycle simulations of the Antarctic Ice Sheet with the Parallel Ice Sheet Model (PISM) –Part 1: Boundary conditions and climatic forcing: The Cryosphere, v. 14, no. 2, p. 599-632.

Alley, R. B., Clark, P. U., Huybrechts, P., and Joughin, I., 2005, Ice-sheet and sea-level changes: science, v. 310, no. 5747, p. 456-460.

Alley, R. B., Marotzke, J., Nordhaus, W. D., Overpeck, J. T., Peteet, D. M., Pielke, R. A., Pierrehumbert, R. T., Rhines, P. B., Stocker, T. F., and Talley, L. D., 2003, Abrupt climate change: science, v. 299, no. 5615, p. 2005-2010.

Andrews, J. T., 1992, A case of missing water: Nature, v. 358, no. 6384, p. 281-281.

Argus, D. F., Peltier, W., Drummond, R., and Moore, A. W., 2014, The Antarctica component of postglacial rebound model ICE-6G_C (VM5a) based on GPS positioning, exposure age dating of ice thicknesses, and relative sea level histories: Geophysical Journal International, v. 198, no. 1, p. 537-563.

Ashe, E. L., Cahill, N., Hay, C., Khan, N. S., Kemp, A., Engelhart, S. E., Horton, B. P., Parnell, A. C., and Kopp, R. E., 2019, Statistical modeling of rates and trends in Holocene relative sea level: Quaternary Science Reviews, v. 204, p. 58-77.

Austermann, J., Mitrovica, J. X., Latychev, K., and Milne, G. A., 2013, Barbados-based estimate of ice volume at Last Glacial Maximum affected by subducted plate: Nature Geoscience, v. 6, no. 7, p. 553-557.

Bakker, P., Schmittner, A., Lenaerts, J., Abe-Ouchi, A., Bi, D., van den Broeke, M., Chan, W. L., Hu, A., Beadling, R., and Marsland, S., 2016, Fate of the Atlantic Meridional Overturning Circulation: Strong decline under continued warming and Greenland melting: Geophysical Research Letters, v. 43, no. 23, p. 12,252-212,260.

Barber, D. C., Dyke, A., Hillaire-Marcel, C., Jennings, A. E., Andrews, J. T., Kerwin, M. W., Bilodeau, G., McNeely, R., Southon, J., and Morehead, M. D., 1999, Forcing of the cold event of 8,200 years ago by catastrophic drainage of Laurentide lakes: Nature, v. 400, no. 6742, p. 344-348.

Barlow, N. L., McClymont, E. L., Whitehouse, P. L., Stokes, C. R., Jamieson, S. S., Woodroffe, S. A., Bentley, M. J., Callard, S. L., Cofaigh, C. Ó., and Evans, D. J., 2018, Lack of evidence for a substantial sea-level fluctuation within the Last Interglacial: Nature Geoscience, v. 11, no. 9, p. 627-634.

Bassett, S. E., Milne, G. A., Mitrovica, J. X., and Clark, P. U., 2005, Ice sheet and solid earth influences on far-field sea-level histories: Science, v. 309, no. 5736, p. 925-928.
Berendsen, H., Makaske, B., Plassche, O. v. d., Van Ree, M., Das, S., Dongen, M. v., Ploumen, S., and Schoenmakers, W., 2007, New groundwater-level rise data from the Rhine-Meuse delta–implications for the reconstruction of Holocene relative mean sea-level rise and differential land-level movements: Netherlands Journal of Geosciences/Geologie en Mijnbouw, v. 86, no. 4, p. 333-354.
Bird, M. I., Fifield, L. K., Chua, S., and Goh, B., 2004, Calculating sediment compaction for radiocarbon dating of intertidal sediments: Radiocarbon, v. 46, no. 1, p. 421-435.
Bird, P., 2003, An updated digital model of plate boundaries: Geochemistry, Geophysics, Geosystems, v. 4, no. 3.
Blanchon, P., Jones, B., and Ford, D. C., 2002, Discovery of a submerged relic reef and shoreline off Grand Cayman: further support for an early Holocene jump in sea level: Sedimentary Geology, v. 147, no. 3-4, p. 253-270.
Blanchon, P., and Shaw, J., 1995, Reef drowning during the last deglaciation: evidence for catastrophic sea-level rise and ice-sheet collapse: Geology, v. 23, no. 1, p. 4-8.
Brain, M. J., Long, A. J., Woodroffe, S. A., Petley, D. N., Milledge, D. G., and Parnell, A. C., 2012, Modelling the effects of sediment compaction on salt marsh reconstructions of recent sea-level rise: Earth and Planetary Science Letters, v. 345, p. 180-193.
Bronk Ramsey, C., 2009, Bayesian analysis of radiocarbon dates: Radiocarbon, v. 51, no. 1, p. 337-360.
-, 2017, OxCal 4.3. 2. 2017.
Caesar, L., Rahmstorf, S., Robinson, A., Feulner, G., and Saba, V., 2018, Observed fingerprint of a weakening Atlantic Ocean overturning circulation: Nature, v. 556, no. 7700, p. 191-196.
Cahill, N., Kemp, A. C., Horton, B. P., and Parnell, A. C., 2015, Modeling sea-level change using errors-in-variables integrated Gaussian processes: The Annals of Applied Statistics, v. 9, no. 2, p. 547-571.
-, 2016, A Bayesian hierarchical model for reconstructing relative sea level: from raw data to rates of change: Climate of the Past, v. 12, no. 2, p. 525-542.
Carlson, A., Anslow, F., Obbink, E., LeGrande, A., Ullman, D., and Licciardi, J., 2009a, Surface-melt driven Laurentide Ice Sheet retreat during the early Holocene: Geophysical Research Letters, v. 36, no. 24.
Carlson, A. E., and Clark, P. U., 2012, Ice sheet sources of sea level rise and freshwater discharge during the last deglaciation: Reviews of Geophysics, v. 50, no. 4.

Carlson, A. E., Clark, P. U., Haley, B. A., and Klinkhammer, G. P., 2009b, Routing of western Canadian Plains runoff during the 8.2 ka cold event: Geophysical Research Letters, v. 36, no. 14.

Carlson, A. E., LeGrande, A. N., Oppo, D. W., Came, R. E., Schmidt, G. A., Anslow, F. S., Licciardi, J. M., and Obbink, E. A., 2008, Rapid early Holocene deglaciation of the Laurentide ice sheet: Nature Geoscience, v. 1, no. 9, p. 620-624.

Cazenave, A., 2006, How fast are the ice sheets melting?: Science, v. 314, no. 5803, p. 1250-1252.

Cazenave, A., Dieng, H.-B., Meyssignac, B., Von Schuckmann, K., Decharme, B., and Berthier, E., 2014, The rate of sea-level rise: Nature Climate Change, v. 4, no. 5, p. 358-361.

Charbit, S., Ritz, C., Philippon, G., Peyaud, V., and Kageyama, M., 2007, Numerical reconstructions of the Northern Hemisphere ice sheets through the last glacial-interglacial cycle: Climate of the Past, v. 3, no. 1, p. 15-37.

Chua, S., Switzer, A. D., Li, T., Chen, H., Christie, M., Shaw, T. A., Khan, N. S., Bird, M. I., and Horton, B. P., 2021, A new Holocene sea-level record for Singapore: The Holocene, p. 09596836211019096.

Clark, P. U., Dyke, A. S., Shakun, J. D., Carlson, A. E., Clark, J., Wohlfarth, B., Mitrovica, J. X., Hostetler, S. W., and McCabe, A. M., 2009, The last glacial maximum: science, v. 325, no. 5941, p. 710-714.

Clark, P. U., Marshall, S. J., Clarke, G. K., Hostetler, S. W., Licciardi, J. M., and Teller, J. T., 2001, Freshwater forcing of abrupt climate change during the last glaciation: Science, v. 293, no. 5528, p. 283-287.

Clark, P. U., and Tarasov, L., 2014, Closing the sea level budget at the Last Glacial Maximum: Proceedings of the National Academy of Sciences, v. 111, no. 45, p. 15861-15862.

Dangendorf, S., Marcos, M., Wöppelmann, G., Conrad, C. P., Frederikse, T., and Riva, R., 2017, Reassessment of 20th century global mean sea level rise: Proceedings of the National Academy of Sciences, v. 114, no. 23, p. 5946-5951.

Dura, T., Cisternas, M., Horton, B. P., Ely, L. L., Nelson, A. R., Wesson, R. L., and Pilarczyk, J. E., 2015, Coastal evidence for Holocene subduction-zone earthquakes and tsunamis in central Chile: Quaternary Science Reviews, v. 113, p. 93-111.

Dutton, A., Carlson, A. E., Long, A., Milne, G. A., Clark, P. U., DeConto, R., Horton, B. P., Rahmstorf, S., and Raymo, M. E., 2015, Sea-level rise due to polar ice-sheet mass loss during past warm periods: science, v. 349, no. 6244, p. aaa4019.

Dutton, A., and Lambeck, K., 2012, Ice volume and sea level during the last interglacial: science, v. 337, no. 6091, p. 216-219.

Düsterhus, A., Tamisiea, M. E., and Jevrejeva, S., 2016, Estimating the sea level highstand during the last interglacial: a probabilistic massive ensemble approach: Geophysical Journal International, v. 206, no. 2, p. 900-920.

Ehlers, J., Gibbard, P., and Hughes, P., 2011, Quaternary glaciations-extent and chronology: a closer look, Elsevier.

Farrell, W., and Clark, J. A., 1976, On postglacial sea level: Geophysical Journal International, v. 46, no. 3, p. 647-667.

Fettweis, X., Box, J. E., Agosta, C., Amory, C., Kittel, C., Lang, C., van As, D., Machguth, H., and Gallée, H., 2017, Reconstructions of the 1900–2015 Greenland ice sheet surface mass balance using the regional climate MAR model: The Cryosphere, v. 11, no. 2, p. 1015-1033.

Frederikse, T., Landerer, F., Caron, L., Adhikari, S., Parkes, D., Humphrey, V. W., Dangendorf, S., Hogarth, P., Zanna, L., and Cheng, L., 2020, The causes of sea-level rise since 1900: Nature, v. 584, no. 7821, p. 393-397.

Gehrels, R., 2010, Sea-level changes since the Last Glacial Maximum: an appraisal of the IPCC Fourth Assessment Report: Journal of Quaternary Science, v. 25, no. 1, p. 26-38.

Geyh, M., Streif, H., and Kudrass, H.-R., 1979, Sea-level changes during the late Pleistocene and Holocene in the Strait of Malacca: Nature, v. 278, no. 5703, p. 441-443.

Golledge, N. R., Keller, E. D., Gomez, N., Naughten, K. A., Bernales, J., Trusel, L. D., and Edwards, T. L., 2019, Global environmental consequences of twenty-first-century ice-sheet melt: Nature, v. 566, no. 7742, p. 65-72.

Golledge, N. R., Levy, R. H., McKay, R. M., Fogwill, C. J., White, D. A., Graham, A. G., Smith, J. A., Hillenbrand, C.-D., Licht, K. J., and Denton, G. H., 2013, Glaciology and geological signature of the Last Glacial Maximum Antarctic ice sheet: Quaternary Science Reviews, v. 78, p. 225-247.

Golledge, N. R., Menviel, L., Carter, L., Fogwill, C. J., England, M. H., Cortese, G., and Levy, R. H., 2014, Antarctic contribution to meltwater pulse 1A from reduced Southern Ocean overturning: Nature communications, v. 5, no. 1, p. 1-10.

Gregoire, L. J., Payne, A. J., and Valdes, P. J., 2012, Deglacial rapid sea level rises caused by ice-sheet saddle collapses: Nature, v. 487, no. 7406, p. 219-222.

Gregory, J. M., Griffies, S. M., Hughes, C. W., Lowe, J. A., Church, J. A., Fukimori, I., Gomez, N., Kopp, R. E., Landerer, F., and Le Cozannet, G., 2019, Concepts and terminology for sea level: Mean, variability and change, both local and global: Surveys in Geophysics, v. 40, no. 6, p. 1251-1289.

Hamlington, B. D., Frederikse, T., Nerem, R. S., Fasullo, J. T., and Adhikari, S., 2020, Investigating the acceleration of regional sea level rise during the satellite altimeter era: Geophysical Research Letters, v. 47, no. 5, p. e2019GL086528.

Hijma, M. P., and Cohen, K. M., 2010, Timing and magnitude of the sea-level jump preluding the 8200 yr event: Geology, v. 38, no. 3, p. 275-278.

-, 2019, Holocene sea-level database for the Rhine-Meuse Delta, The Netherlands: Implications for the pre-8.2 ka sea-level jump: Quaternary Science Reviews, v. 214, p. 68-86.

Hijma, M. P., Engelhart, S. E., Törnqvist, T. E., Horton, B. P., Hu, P., and Hill, D. F., 2015, A protocol for a geological sea-level database: Handbook of Sea-Level Research, edited by: Shennan, I., Long, AJ, and Horton, BP, Wiley Blackwell, p. 536-553.

Hill, D., Griffiths, S., Peltier, W., Horton, B., and Törnqvist, T., 2011, High-resolution numerical modeling of tides in the western Atlantic, Gulf of Mexico, and Caribbean Sea during the Holocene: Journal of Geophysical Research: Oceans, v. 116, no. C10.

Hori, K., and Saito, Y., 2007, An early Holocene sea-level jump and delta initiation: Geophysical Research Letters, v. 34, no. 18.

Horton, B. P., Khan, N. S., Cahill, N., Lee, J. S., Shaw, T. A., Garner, A. J., Kemp, A. C., Engelhart, S. E., and Rahmstorf, S., 2020, Estimating global mean sea-level rise and its uncertainties by 2100 and 2300 from an expert survey: npj Climate and Atmospheric Science, v. 3, no. 1, p. 1-8.

Hu, P., 2010, Developing a quality-controlled postglacial sea-level database for coastal Louisiana to assess conflicting hypotheses of Gulf Coast sea-level change: Tulane University, New Orleans.

Hughes, A. L., Gyllencreutz, R., Lohne, Ø. S., Mangerud, J., and Svendsen, J. I., 2016, The last Eurasian ice sheets–a chronological database and time-slice reconstruction, DATED-1: Boreas, v. 45, no. 1, p. 1-45.

IMBIE, 2018, Mass balance of the Antarctic Ice Sheet from 1992 to 2017: Nature, v. 558, no. 7709, p. 219-222.

IMBIE, Shepherd, A., Ivins, E., Rignot, E., Smith, B., Van Den Broeke, M., Velicogna, I., Whitehouse, P., Briggs, K., Joughin, I., and Krinner, G., 2020, Mass balance of the Greenland Ice Sheet from 1992 to 2018: Nature, v. 579, no. 7798, p. 233-239.

Ivins, E. R., James, T. S., Wahr, J., O. Schrama, E. J., Landerer, F. W., and Simon, K. M., 2013, Antarctic contribution to sea level rise observed by GRACE with improved GIA correction: Journal of Geophysical Research: Solid Earth, v. 118, no. 6, p. 3126-3141.

Jelgersma, S., 1961, Holocene sea-level changes in the Netherlands: Ph. D. dissertation, Leiden Univ.

Joughin, I., Smith, B. E., and Medley, B., 2014, Marine ice sheet collapse potentially under way for the Thwaites Glacier Basin, West Antarctica: Science, v. 344, no. 6185, p. 735-738.

Kendall, R. A., Mitrovica, J. X., Milne, G. A., Törnqvist, T. E., and Li, Y., 2008, The sea-level fingerprint of the 8.2 ka climate event: Geology, v. 36, no. 5, p. 423-426.

Keogh, M. E., Törnqvist, T. E., Kolker, A. S., Erkens, G., and Bridgeman, J. G., 2021, Organic matter accretion, shallow subsidence, and river delta

sustainability: Journal of Geophysical Research: Earth Surface, v. 126, no. 12, p. e2021JF006231.
Khan, N. S., Horton, B. P., Engelhart, S., Rovere, A., Vacchi, M., Ashe, E. L., Törnqvist, T. E., Dutton, A., Hijma, M. P., and Shennan, I., 2019, Inception of a global atlas of sea levels since the Last Glacial Maximum: Quaternary Science Reviews, v. 220, p. 359-371.
Kuchar, J., Milne, G., Wolstencroft, M., Love, R., Tarasov, L., and Hijma, M., 2018, The influence of sediment isostatic adjustment on sea level change and land motion along the U.S. Gulf Coast: Journal of Geophysical Research: Solid Earth, v. 123, no. 1, p. 780-796.
Lambeck, K., 1995, Late Devensian and Holocene shorelines of the British Isles and North Sea from models of glacio-hydro-isostatic rebound: Journal of the Geological Society, v. 152, no. 3, p. 437-448.
Lambeck, K., Purcell, A., and Zhao, S., 2017, The North American Late Wisconsin ice sheet and mantle viscosity from glacial rebound analyses: Quaternary Science Reviews, v. 158, p. 172-210.
Lambeck, K., Rouby, H., Purcell, A., Sun, Y., and Sambridge, M., 2014a, Sea level and global ice volumes from the Last Glacial Maximum to the Holocene: Proceedings of the National Academy of Sciences of the United States of America, v. 111, no. 43, p. 15296-15303.
-, 2014b, Sea level and global ice volumes from the Last Glacial Maximum to the Holocene: Proceedings of the National Academy of Sciences, v. 111, no. 43, p. 15296-15303.
Lawrence, T., Long, A. J., Gehrels, W. R., Jackson, L. P., and Smith, D. E., 2016, Relative sea-level data from southwest Scotland constrain meltwater-driven sea-level jumps prior to the 8.2 kyr BP event: Quaternary science reviews, v. 151, p. 292-308.
Leverington, D. W., Mann, J. D., and Teller, J. T., 2002, Changes in the bathymetry and volume of glacial Lake Agassiz between 9200 and 7700 14C yr BP: Quaternary Research, v. 57, no. 2, p. 244-252.
Levermann, A., Clark, P. U., Marzeion, B., Milne, G. A., Pollard, D., Radic, V., and Robinson, A., 2013, The multimillennial sea-level commitment of global warming: Proceedings of the National Academy of Sciences, v. 110, no. 34, p. 13745-13750.
Lewis, S. E., Wüst, R. A., Webster, J. M., and Shields, G. A., 2008, Mid-late Holocene sea-level variability in eastern Australia: Terra Nova, v. 20, no. 1, p. 74-81.
Li, Y.-X., Törnqvist, T. E., Nevitt, J. M., and Kohl, B., 2012, Synchronizing a sea-level jump, final Lake Agassiz drainage, and abrupt cooling 8200 years ago: Earth and Planetary Science Letters, v. 315, p. 41-50.
Licciardi, J. M., Clark, P. U., Jenson, J. W., and Macayeal, D. R., 1998, Deglaciation of a soft-bedded Laurentide Ice Sheet: Quaternary Science Reviews, v. 17, no. 4-5, p. 427-448.

Love, R., Milne, G. A., Tarasov, L., Engelhart, S. E., Hijma, M. P., Latychev, K., Horton, B. P., and Törnqvist, T. E., 2016, The contribution of glacial isostatic adjustment to projections of sea-level change along the Atlantic and Gulf coasts of North America: Earth's Future, v. 4, no. 10, p. 440-464.

Marshall, S. J., Tarasov, L., Clarke, G. K., and Peltier, W. R., 2000, Glaciological reconstruction of the Laurentide Ice Sheet: physical processes and modelling challenges: Canadian Journal of Earth Sciences, v. 37, no. 5, p. 769-793.

Matero, I., Gregoire, L., Ivanovic, R., Tindall, J., and Haywood, A., 2017, The 8.2 ka cooling event caused by Laurentide ice saddle collapse: Earth and Planetary Science Letters, v. 473, p. 205-214.

Mauz, B., Vacchi, M., Green, A., Hoffmann, G., and Cooper, A., 2015, Beachrock: a tool for reconstructing relative sea level in the far-field: Marine Geology, v. 362, p. 1-16.

Milne, G., and Shennan, I., 2013, SEA LEVEL STUDIES | Isostasy: Glaciation-Induced Sea-Level Change.

Milne, G. A., Gehrels, W. R., Hughes, C. W., and Tamisiea, M. E., 2009, Identifying the causes of sea-level change: Nature Geoscience, v. 2, no. 7, p. 471-478.

Milne, G. A., and Peros, M., 2013, Data–model comparison of Holocene sea-level change in the circum-Caribbean region: Global and Planetary Change, v. 107, p. 119-131.

Mitrovica, J. X., and Milne, G. A., 2003, On post-glacial sea level: I. General theory: Geophysical Journal International, v. 154, no. 2, p. 253-267.

Moore, J. C., Grinsted, A., Zwinger, T., and Jevrejeva, S., 2013, Semiempirical and process-based global sea level projections: Reviews of Geophysics, v. 51, no. 3, p. 484-522.

Morrill, C., LeGrande, A. N., Renssen, H., Bakker, P., and Otto-Bliesner, B., 2013, Model sensitivity to North Atlantic freshwater forcing at 8.2 ka: Climate of the Past, v. 9, no. 2, p. 955-968.

Nichols, K. A., Goehring, B. M., Balco, G., Johnson, J. S., Hein, A. S., and Todd, C., 2019, New last glacial maximum ice thickness constraints for the Weddell Sea Embayment, Antarctica: The Cryosphere, v. 13, no. 11, p. 2935-2951.

Obrist-Farner, J., Brenner, M., Stone, J. R., Wojewódka-Przybył, M., Bauersachs, T., Eckert, A., Locmelis, M., Curtis, J. H., Zimmerman, S. R., and Correa-Metrio, A., 2022, New estimates of the magnitude of the sea-level jump during the 8.2 ka event: Geology, v. 50, no. 1, p. 86-90.

Palsea, 2010, The sea-level conundrum: case studies from palaeo-archives: Journal of Quaternary Science, v. 25, no. 1, p. 19-25.

Peltier, W., 1974, The impulse response of a Maxwell Earth: Reviews of Geophysics, v. 12, no. 4, p. 649-669.

Peltier, W. R., 2004, Global glacial isostasy and the surface of the ice-age Earth: the ICE-5G (VM2) model and GRACE: Annu. Rev. Earth Planet. Sci., v. 32, p. 111-149.

Peltier, W. R., Argus, D., and Drummond, R., 2015, Space geodesy constrains ice age terminal deglaciation: The global ICE-6G_C (VM5a) model: Journal of Geophysical Research: Solid Earth, v. 120, no. 1, p. 450-487.
Raymo, M. E., and Mitrovica, J. X., 2012, Collapse of polar ice sheets during the stage 11 interglacial: Nature, v. 483, no. 7390, p. 453-456.
Raymo, M. E., Mitrovica, J. X., O'Leary, M. J., DeConto, R. M., and Hearty, P. L., 2011, Departures from eustasy in Pliocene sea-level records: Nature Geoscience, v. 4, no. 5, p. 328-332.
Reimer, P. J., Austin, W. E., Bard, E., Bayliss, A., Blackwell, P. G., Ramsey, C. B., Butzin, M., Cheng, H., Edwards, R. L., and Friedrich, M., 2020, The IntCal20 Northern Hemisphere radiocarbon age calibration curve (0–55 cal kBP): Radiocarbon, v. 62, no. 4, p. 725-757.
Renssen, H., Goosse, H., Fichefet, T., and Campin, J. M., 2001, The 8.2 kyr BP event simulated by a global atmosphere—sea-ice—ocean model: Geophysical Research Letters, v. 28, no. 8, p. 1567-1570.
Rignot, E., Velicogna, I., van den Broeke, M. R., Monaghan, A., and Lenaerts, J. T., 2011, Acceleration of the contribution of the Greenland and Antarctic ice sheets to sea level rise: Geophysical Research Letters, v. 38, no. 5.
Roy, K., and Peltier, W., 2017, Space-geodetic and water level gauge constraints on continental uplift and tilting over North America: regional convergence of the ICE-6G_C (VM5a/VM6) models: Geophysical Journal International, v. 210, no. 2, p. 1115-1142.
Sefton, J., Woodroffe, S., and Ascough, P., 2021, Radiocarbon dating of mangrove sediments, Dynamic Sedimentary Environments of Mangrove Coasts, Elsevier, p. 199-215.
Sella, G. F., Stein, S., Dixon, T. H., Craymer, M., James, T. S., Mazzotti, S., and Dokka, R. K., 2007, Observation of glacial isostatic adjustment in “stable” North America with GPS: Geophysical Research Letters, v. 34, no. 2.
Sgubin, G., Swingedouw, D., Drijfhout, S., Mary, Y., and Bennabi, A., 2017, Abrupt cooling over the North Atlantic in modern climate models: Nature Communications, v. 8, no. 1, p. 1-12.
Shennan, I., 1982, Interpretation of Flandrian sea-level data from the Fenland, England: Proceedings of the Geologists' Association, v. 93, no. 1, p. 53-63.
Shepherd, A., Ivins, E., Rignot, E., Smith, B., Van Den Broeke, M., Velicogna, I., Whitehouse, P., Briggs, K., Joughin, I., and Krinner, G., 2020, Mass balance of the Greenland Ice Sheet from 1992 to 2018: Nature, v. 579, no. 7798, p. 233-239.
Shepherd, A., Ivins, E. R., Geruo, A., Barletta, V. R., Bentley, M. J., Bettadpur, S., Briggs, K. H., Bromwich, D. H., Forsberg, R., and Galin, N., 2012, A reconciled estimate of ice-sheet mass balance: Science, v. 338, no. 6111, p. 1183-1189.
Simms, A. R., Lambeck, K., Purcell, A., Anderson, J. B., and Rodriguez, A. B., 2007a, Sea-level history of the Gulf of Mexico since the Last Glacial

Maximum with implications for the melting history of the Laurentide Ice Sheet: Quaternary Science Reviews, v. 26, no. 7-8, p. 920-940.

-, 2007b, Sea-level history of the Gulf of Mexico since the Last Glacial Maximum with implications for the melting history of the Laurentide Ice Sheet: Quaternary Science Reviews, v. 26, p. 920-940.

Simms, A. R., Lisiecki, L., Gebbie, G., Whitehouse, P. L., and Clark, J. F., 2019, Balancing the last glacial maximum (LGM) sea-level budget: Quaternary Science Reviews, v. 205, p. 143-153.

Smith, D., Harrison, S., Firth, C. R., and Jordan, J. T., 2011, The early Holocene sea level rise: Quaternary Science Reviews, v. 30, no. 15-16, p. 1846-1860.

Stammer, D., Cazenave, A., Ponte, R. M., and Tamisiea, M. E., 2013, Causes for contemporary regional sea level changes: Annual review of marine science, v. 5, p. 21-46.

Stocchi, P., and Spada, G., 2009, Influence of glacial isostatic adjustment upon current sea level variations in the Mediterranean: Tectonophysics, v. 474, no. 1-2, p. 56-68.

Stroeven, A. P., Hättestrand, C., Kleman, J., Heyman, J., Fabel, D., Fredin, O., Goodfellow, B. W., Harbor, J. M., Jansen, J. D., and Olsen, L., 2016, Deglaciation of fennoscandia: Quaternary Science Reviews, v. 147, p. 91-121.

Stuhne, G., and Peltier, W., 2017, Assimilating the ICE-6G_C reconstruction of the latest Quaternary ice age cycle into numerical simulations of the Laurentide and Fennoscandian ice sheets: Journal of Geophysical Research: Earth Surface, v. 122, no. 12, p. 2324-2347.

Stuiver, M., and Polach, H. A., 1977, Discussion reporting of 14C data: Radiocarbon, v. 19, no. 3, p. 355-363.

Swingedouw, D., Braconnot, P., Delécluse, P., Guilyardi, E., and Marti, O., 2007, Quantifying the AMOC feedbacks during a 2× CO 2 stabilization experiment with land-ice melting: Climate dynamics, v. 29, no. 5, p. 521-534.

Tapley, B. D., Watkins, M. M., Flechtner, F., Reigber, C., Bettadpur, S., Rodell, M., Sasgen, I., Famiglietti, J. S., Landerer, F. W., and Chambers, D. P., 2019, Contributions of GRACE to understanding climate change: Nature climate change, v. 9, no. 5, p. 358-369.

Tarasov, L., Dyke, A. S., Neal, R. M., and Peltier, W. R., 2012, A data-calibrated distribution of deglacial chronologies for the North American ice complex from glaciological modeling: Earth and Planetary Science Letters, v. 315, p. 30-40.

Thornalley, D. J., Oppo, D. W., Ortega, P., Robson, J. I., Brierley, C. M., Davis, R., Hall, I. R., Moffa-Sanchez, P., Rose, N. L., and Spooner, P. T., 2018, Anomalously weak Labrador Sea convection and Atlantic overturning during the past 150 years: Nature, v. 556, no. 7700, p. 227-230.

Tornqvist, T. E., Wallace, D. J., Storms, J. E. A., Wallinga, J., Van Dam, R. L., Blaauw, M., Derksen, M. S., Klerks, C. J. W., Meijneken, C., and Snijders, E. A., 2008, Mississippi Delta subsidence primarily caused by compation of Holocene strata: Nature Geosciences.

Törnqvist, T. E., Bick, S. J., González, J. L., van der Borg, K., and de Jong, A. F., 2004a, Tracking the sea-level signature of the 8.2 ka cooling event: new constraints from the Mississippi Delta: Geophysical Research Letters, v. 31, no. 23.

Törnqvist, T. E., González, J. L., Newsom, L. A., Van der Borg, K., De Jong, A. F. M., and Kurnik, C. W., 2004b, Deciphering Holocene sea-level history on the U.S. Gulf Coast: A high-resolution record from the Mississippi Delta: Geological Society of America Bulletin, v. 116, p. 1026-1039.

Törnqvist, T. E., and Hijma, M. P., 2012, Links between early Holocene ice-sheet decay, sea-level rise and abrupt climate change: Nature Geoscience, v. 5, no. 9, p. 601-606.

Uehara, K., Saito, Y., and Hori, K., 2002, Paleotidal regime in the Changjiang (Yangtze) Estuary, the East China Sea, and the Yellow Sea at 6 ka and 10 ka estimated from a numerical model: Marine Geology, v. 183, no. 1-4, p. 179-192.

Uehara, K., Scourse, J. D., Horsburgh, K. J., Lambeck, K., and Purcell, A. P., 2006, Tidal evolution of the northwest European shelf seas from the Last Glacial Maximum to the present: Journal of Geophysical Research: Oceans, v. 111, no. C9.

Ullman, D. J., Carlson, A. E., Hostetler, S. W., Clark, P. U., Cuzzone, J., Milne, G. A., Winsor, K., and Caffee, M., 2016, Final Laurentide ice-sheet deglaciation and Holocene climate-sea level change: Quaternary Science Reviews, v. 152, p. 49-59.

Van Asselen, S., Stouthamer, E., and Van Asch, T. W., 2009, Effects of peat compaction on delta evolution: a review on processes, responses, measuring and modeling: Earth-Science Reviews, v. 92, no. 1-2, p. 35-51.

van de Plassche, O., 1982, Sea-level change and water-level movements in the Netherlands during the Holocene: Ph. D. dissertation, Vrije Universiteit Amsterdam.

-, 1995, Evolution of the intra-coastal tidal range in the Rhine-Meuse delta and Flevo Lagoon, 5700-3000 yrs cal BC: Marine Geology, v. 124, no. 1-4, p. 113-128.

Van de Plassche, O., Makaske, B., Hoek, W., Konert, M., and Van der Plicht, J., 2010, Mid-Holocene water-level changes in the lower Rhine-Meuse delta (western Netherlands): implications for the reconstruction of relative mean sea-level rise, palaeoriver-gradients and coastal evolution: Netherlands Journal of Geosciences, v. 89, no. 1, p. 3-20.

van den Broeke, M., Bamber, J., Ettema, J., Rignot, E., Schrama, E., van de Berg, W. J., van Meijgaard, E., Velicogna, I., and Wouters, B., 2009, Partitioning recent Greenland mass loss: science, v. 326, no. 5955, p. 984-986.

Vetter, L., Rosenheim, B. E., Fernandez, A., and Törnqvist, T. E., 2017, Short organic carbon turnover time and narrow ^{14}C age spectra in early Holocene wetland paleosols: Geochemistry, Geophysics, Geosystems, v. 18, no. 1, p. 142-155.

Vos, P., 2013, Geologisch en paleolandschappelijk onderzoek Yangtzehaven (Maasvlakte, Rotterdam). Toegepast geoarcheologisch onderzoek ten behoeve van de archeologische prospectie in Vroeg Holocene deltaïsche afzettingen van Rijn en Maas in het Maasvlaktegebied, Utrecht (Deltares-rapport 1206788-000-BGS-0001).

Vos, P., and Cohen, K., Landscape genesis and palaeogeography2015, Gemeente Rotterdam.

Vos, P. C., Bunnik, F. P., Cohen, K. M., and Cremer, H., 2015, A staged geogenetic approach to underwater archaeological prospection in the Port of Rotterdam (Yangtzehaven, Maasvlakte, The Netherlands): A geological and palaeoenvironmental case study for local mapping of Mesolithic lowland landscapes: Quaternary International, v. 367, p. 4-31.

Wagner, A. J., Morrill, C., Otto-Bliesner, B. L., Rosenbloom, N., and Watkins, K. R., 2013, Model support for forcing of the 8.2 ka event by meltwater from the Hudson Bay ice dome: Climate dynamics, v. 41, no. 11, p. 2855-2873.

Wang, Z., Ryves, D. B., Lei, S., Nian, X., Lv, Y., Tang, L., Wang, L., Wang, J., and Chen, J., 2018, Middle Holocene marine flooding and human response in the south Yangtze coastal plain, East China: Quaternary Science Reviews, v. 187, p. 80-93.

Wang, Z., Zhan, Q., Long, H., Saito, Y., Gao, X., Wu, X., Li, L., and Zhao, Y., 2013, Early to mid-H olocene rapid sea-level rise and coastal response on the southern Yangtze delta plain, China: Journal of Quaternary Science, v. 28, no. 7, p. 659-672.

Whitehouse, P. L., 2018, Glacial isostatic adjustment modelling: historical perspectives, recent advances, and future directions: Earth Surface Dynamics, v. 6, no. 2, p. 401.

Whitehouse, P. L., Bentley, M. J., and Le Brocq, A. M., 2012a, A deglacial model for Antarctica: geological constraints and glaciological modelling as a basis for a new model of Antarctic glacial isostatic adjustment: Quaternary Science Reviews, v. 32, p. 1-24.

Whitehouse, P. L., Bentley, M. J., Milne, G. A., King, M. A., and Thomas, I. D., 2012b, A new glacial isostatic adjustment model for Antarctica: calibrated and tested using observations of relative sea-level change and present-day uplift rates: Geophysical Journal International, v. 190, no. 3, p. 1464-1482.

Wiersma, A., Renssen, H., Goosse, H., and Fichefet, T., 2006, Evaluation of different freshwater forcing scenarios for the 8.2 ka BP event in a coupled climate model: Climate Dynamics, v. 27, no. 7, p. 831-849.

Wiersma, A. P., and Jongma, J. I., 2010, A role for icebergs in the 8.2 ka climate event: Climate dynamics, v. 35, no. 2, p. 535-549.

Wolstencroft, M., Shen, Z., Törnqvist, T. E., Milne, G. A., and Kulp, M., 2014, Understanding subsidence in the Mississippi Delta region due to sediment, ice, and ocean loading: Insights from geophysical modeling: Journal of Geophysical Research: Solid Earth, v. 119, no. 4, p. 3838-3856.

Woodroffe, S. A., Long, A. J., Punwong, P., Selby, K., Bryant, C. L., and Marchant, R., 2015, Radiocarbon dating of mangrove sediments to constrain Holocene relative sea-level change on Zanzibar in the southwest Indian Ocean: The Holocene, v. 25, no. 5, p. 820-831.

Yu, S.-Y., Berglund, B. r. E., Sandgren, P., and Lambeck, K., 2007, Evidence for a rapid sea-level rise 7600 yr ago: Geology, v. 35, no. 10, p. 891-894.

Yu, S.-Y., Törnqvist, T. E., and Hu, P., 2012, Quantifying Holocene lithospheric subsidence rates underneath the Mississippi Delta: Earth and Planetary Science Letters, v. 331-332, p. 21-30.

Zong, Y., Innes, J. B., Wang, Z., and Chen, Z., 2011, Mid-Holocene coastal hydrology and salinity changes in the east Taihu area of the lower Yangtze wetlands, China: Quaternary Research, v. 76, no. 1, p. 69-82.

Fox-Kemper, B., H. T. Hewitt, C. Xiao, G. Aðalgeirsdóttir, S. S. Drijfhout, T. L. Edwards, N. R. Golledge, M. Hemer, R. E. Kopp, G. Krinner, A. Mix, D. Notz, S. Nowicki, I. S. Nurhati, L. Ruiz, J-B. Sallée, A. B. A. Slangen, Y. Yu, 2021, Ocean, Cryosphere and Sea Level Change. In: Climate Change 2021: The Physical Science Basis. Contribution of Working Group I to the Sixth Assessment Report of the Intergovernmental Panel on Climate Change [Masson-Delmotte, V., P. Zhai, A. Pirani, S. L. Connors, C. Péan, S. Berger, N. Caud, Y. Chen, L. Goldfarb, M. I. Gomis, M. Huang, K. Leitzell, E. Lonnoy, J.B.R. Matthews, T. K. Maycock, T. Waterfield, O. Yelekçi, R. Yu and B. Zhou (eds.)]. Cambridge University Press. In Press

CHAPTER 2: What controlled sediment transport across the continental shelf edge during the Last Glacial Maximum? A case-study from the South African continental margin

ABSTRACT

Source to sink (S2S) research has come to the forefront as a holistic paradigm of sediment transport and stratigraphic studies as well as for implications on biogeochemical cycles. In this chapter my aim is to understand the influence of sediment flux, be it from a single large source or multiple point-sources available, and the distance between the shoreline and the continental shelf edge during RSL lowstand on the formation and progradation of the shelf-edge. The eastern and western shelves off southern Africa not only have different morphologies, but also exhibit a difference in climate, precipitation, relief, type of sediment transport, and size of drainage basins, thus giving us an appropriate study area to test our research questions. We use a glacio-isostatic adjustment model of the southern African continental shelf to recreate the paleo-elevation of the region during the Last Glacial Maximum (LGM, ~21 ka) to recreate the LGM shoreline and the shelf edge. The interaction between the shoreline and the shelf edge during the LGM shows different extents of exposure of the continental shelf in different portions of the area. The sediment flux transported by rivers to the two shelves are also different. Using relatively simple geomorphic parameters involving the morphology of the shelf edge, the project seeks to answer questions

about whether riverine sediments can reach the deeper marine sinks during RSL lowstands and prograde the continental shelf edge.

2.1 Introduction

Source to sink (S2S) research has come to the forefront as a holistic paradigm of sediment transport and stratigraphic studies. Borrowing from the ideas of Hutton (1788), S2S research can be defined as an approach to link areas of sediment production to the transport-limited parts of the system and the sinks, and it aims to quantify earth-surface processes in a budgetary manner (Walsh et al., 2016). Typically, a sedimentary system can be subdivided into three spatial zones based on the dominant mass-flux behavior active at that point in the system, namely, denudation/erosion, transfer, and accumulation/ deposition (Schumm, 1977). Instead of looking at these different domains of sediment transport systems individually, as is done in traditional sedimentology and stratigraphy, the S2S concept focuses on integration and quantification of the various components of the siliciclastic sedimentary system.

Boundaries like the continental shelf edge (CSE) are important components of S2S studies, because the CSE plays a significant role in the partitioning of sediments between shelf and deep-water environments. The CSE acts as the transition zone between mixed marine and terrestrial sediments, driven in part by shelf currents and fluvial processes, to predominantly deep marine sedimentation, generally carved out by gravity driven processes (Laugier and Plink-Björklund, 2016). The continental shelf is the only area where there is a probability of the formation of all the seven different types of sequence stratigraphic surfaces, influenced by the change in shoreline trajectory (Catuneanu et al., 2009b).

The sediment transport mechanism active in the shelf-slope system is important for several distinct reasons. Submergence of the shelf and the CSE depends on relative sea level (RSL) and sediment supply, thus making the CSE a variable but significant component in the S2S system. During high-amplitude lowstand conditions, individual river basins merge to decrease the number of point sources of sediment emptying into deep-marine basins, typically increasing the amount of sediment being supplied at the single point source that flows across the exposed broad shelf to the CSE. The process of channel migration and valley widening on the shelf after incision also increases the sediment flux flowing into the basin (Blum et al., 2013). Formation and maintenance of the characteristic topography of the shelf and CSE is dependent solely on sedimentation or a combination of both sedimentation and tectonics (Helland-Hansen et al., 2012). It has also been proposed that the smaller the river system flowing onto the shelf, the easier it is for the shelf system to maintain a steeper and narrower shelf, making it easier for the sediments to bypass the shelf (Sømme et al., 2009). However, Nyberg et al. (2018) argue against this because of a weak power-law correlation between sediment discharge and shelf width.

Most traditional sequence-stratigraphic models explain deep-marine sedimentation to occur during lowstand conditions (Catuneanu et al., 2009b; Porębski and Steel, 2003; Posamentier and Vail, 1988a). But a number of other studies talk about the caveat to these models and the possibility of deep-marine deposition during highstand (Burgess and Hovius, 1998; Posamentier, 2001). In traditional sequence-stratigraphic models, cross-shelf paleovalleys (Blum et al., 2013; Zaitlin et al., 1994) are considered to be the transport systems through which, during RSL lowstands, sediment supply from the continents can be transported over the shelf, which aids in deep-marine sedimentation by formation of submarine channel and fan systems (Catuneanu et al., 2009b; Posamentier et al., 1992). These models suggest that valley cutting is an immediate result of RSL fall at the CSECSE (Posamentier and Vail, 1988b). There is a need to understand and quantify how, when and where paleovalleys are created due to RSL fall. Paleovalleys are important constituents of the sequence stratigraphic framework, as they are used to define sequence boundaries. The relationship between RSL change and valley formation, is a critical parameter that needs to be studied in detail, as are the issues of the nature of CSE evolution and their biogeochemical implications.

The complexity of spatiotemporal relations between RSL change and valley formation has been studied by a number of researchers (e.g.,(Amorosi et al., 2016; Blum et al., 2013; Blum and Törnqvist, 2000; Catuneanu et al., 2009b; Schumm, 1993; Törnqvist et al., 2000; Wallinga et al., 2004). In particular, the question of whether RSL drops below the CSE is a critical one. The width of exposed continental shelf during an RSL lowstand depends on the CSE morphology and extent of RSL fall, which, in turn, determine the formation of paleovalleys. The position of the lowstand shoreline with respect to the CSE depends on the depth and morphology of the CSE (Fig 18). To investigate how the relationship between the CSE and the Last Glacial Maximum (LGM) shoreline influences the formation of paleovalleys that could have aided in sediment transport to the deep marine environment during the LGM, Törnqvist et. al. (2006) selected two contrasting CSE systems, the Gulf of Mexico, more

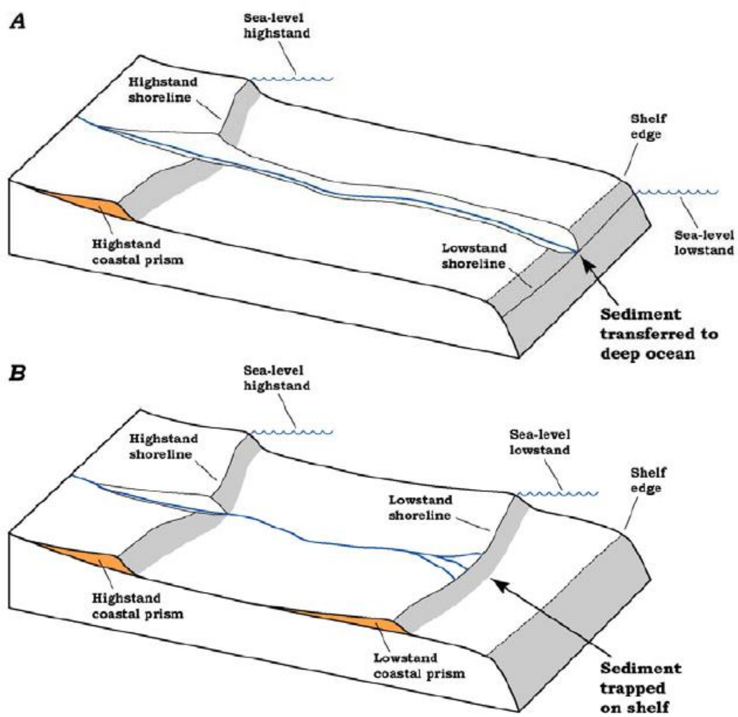

Figure 18 Contrasting scenarios of lowstand shoreline position and fluvial incision. (after Törnqvist et al., 2006). A describes a scenario where the lowstand sea-level falls below the CSE, transporting sediments to the deep ocean. B shows a situation where the lowstand shoreline remains on the shelf, trapping sediments on the shelf.

specifically the US Gulf Coast, and the Bay of Biscay. To recreate the paleo-topography of the two areas, a glacial isostatic adjustment (GIA) model was used. The two areas were strikingly different, as the modeled lowstand shoreline in the Gulf of Mexico was located seaward of the CSE, whereas in the case of the Bay of Biscay, the modeled lowstand shoreline was located well updip on the shelf. Due to the exposure of the Gulf of Mexico shelf during LGM, evidence of widespread fluvial incision can be found all across the shelf (Anderson et al., 2016; Suter and Berryhill Jr, 1985). But in the Bay of Biscay, because the CSE and parts of the shelf remained submerged during RSL lowstand, fluvial incision was limited to the highstand coastal prism.

The contrasting scenarios between the Bay of Biscay and the Gulf of Mexico imply that the conventional sequence-stratigraphic models need to be reevaluated to consider stratigraphic conditions where the continental and deep marine sections of a transport system remain detached. Passive margins with differing sediment flux will also differ in the way they maintain and prograde their shape. I hypothesize that, in a passive margin setting, the progradation of the shelf edge depends on the amount of relative sea-level (RSL) fall leading to exposure of the shelf which in turn influences paleovalley incision that plays a big part in transporting sediments across the shelf edge. It also depends on the total amount of sediment flux coming from the hinterland, be it one large transport system or multiple point sources.

The wider and deeper the continental shelf-slope system, the greater the chance of a separation between the lowstand shoreline and the CSE. Fluvial incision occurring in such a condition will most likely be focused only on the shelf (Fig 18B) and will not be able to cross over to the slope system, thus depositing most of the sediment on the shelf. Moreover, depending on the amount of sediment coming into the shelf, the paleovalley that is incised can differ in dimensions and their ability to reach the CSE (Schumm, 1993). Depending on whether the sediment load bypasses the shelf or remains trapped on the shelf, it will have a prominent role to play in the formation and maintenance of the CSE geometry, as sedimentation is a primary factor in CSE morphology (Helland-Hansen et al., 2012).

Compared to other parts of the world, the African shelf is not as well studied (Chiocci and Chivas, 2014). However, the interaction between the shelf and CSE geometry, RSL change, and differing sedimentation makes southern Africa extremely interesting to conduct a study like this. The eastern and western shelves of southern Africa are distinctly different in morphology, the eastern shelf being <5 km wide at places. The eastern shelf is also steeper than the western shelf. Paleovalleys from the LGM have been reported from the eastern shelf (Green and Uken, 2005). The eastern shelf receives more sediment from a number of smaller rivers as well as the Limpopo River, compared to the western shelf which is drained by the Orange River.

This project can help in understanding global carbon cycling (Leithold et al., 2016). Of the 200 Tg of particulate organic carbon (OC) being delivered every year to the oceans, continental shelves store about 10-25% particulate OC, along with the particulate OC originating from marine production (Blair and Aller, 2012; Burdige, 2005; Galy et al., 2007; Ludwig et al., 1996). Understanding how sediments are delivered to the deeper ocean, bypassing the shelf, can also have implication in our understanding of carbon storage in the continental shelf during the last 20 kyr.

In this study we determine the distance between the LGM shoreline and the CSE using the paleotopography generated from a GIA model, which has been calibrated using a RSL database. A critical look at the available RSL data from southern Africa is necessary to understand the regional RSL history. Such a database is needed to calibrate and test the RSL change of the study area as calculated from GIA modeling. During the past ~20 kyr, through which the Earth has undergone major and complex changes in RSL due to melting ice sheets, changes in RSL in southern Africa are mostly the result of glacio-eustasy and vertical land motion due to GIA, with other vertical movements like tectonics playing a smaller part (Wildman et al., 2016) in the total vertical movement of the crust in this region. Ocean steric and dynamic effects are also assumed to be small over these timescales. The vertical movements caused by GIA are spatially variable around the globe due to the difference in the proximity to the ice sheets and earth rheology, and the change in RSL in a far-field location like southern

Africa is affected by the earth rheology and the volume of meltwater being added to the ocean (Milne and Mitrovica, 2008; Lambeck et al., 2014).

2.2Study area

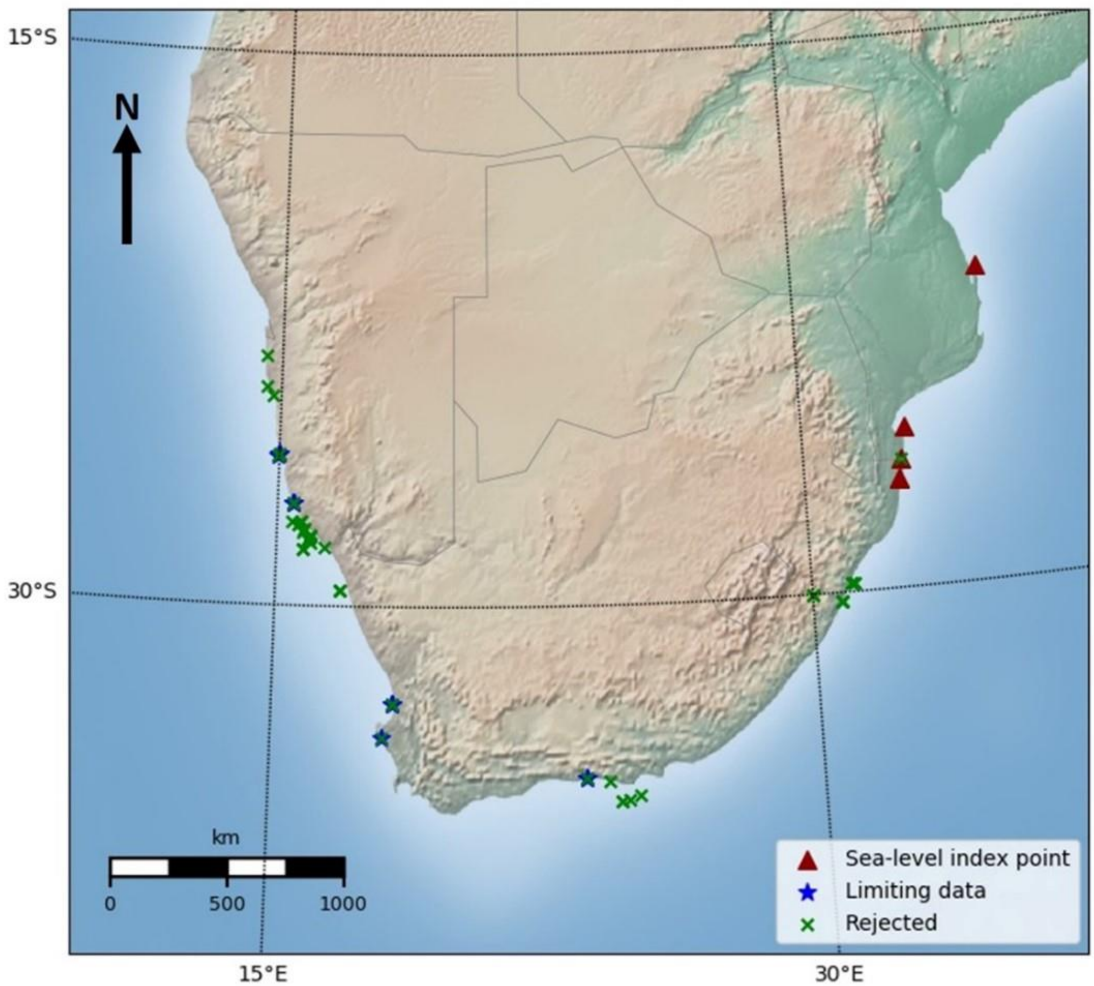

Figure 19 A topographic map of southern Africa, indicating the study area. The locations of the sea-level indicators used here are marked by the various symbols, as shown in the legend.

The study area (Figure 19) consists of the southernmost part of the African continent. Tectonically, the southern African shelf is a passive margin and was also non-glaciated. The elevated southern African interior plateau is believed to have been formed due to deep mantle activity, due to the absence of collisional tectonism and the presence of a large low shear velocity province (Ritsema et al., 1998; Sun and Miller, 2013). The flanks of the southern African plateau is characterized by higher relief near the coast, with higher elevations along the eastern coast compared to the western coast (Amante and Eakins, 2009; Stanley et al., 2021).Thermochronological studies (apatite fission track and U-Th-Sm/He thermochronology), landscape-evolution modeling, stratigraphic data, as well as cosmogenic dating show that the major epeirogenic uplift and subsequent denudation of the southern African plateau happened mainly during the Cretaceous and possibly during the mid-Cenozoic, with only ~1 km of elevation denuded during the Cenozoic (Braun et al., 2014; De Wit, 2007; Stanley et al., 2021; Tinker et al., 2008; Wildman et al., 2016; Wildman et al., 2017). Due to the low isostatic gravity anomaly and free-air gravity anomaly, it has been proposed that the influence of dynamic topography in this area may have been small (Molnar et al., 2015) and this area has sustained a high elevation since the Cretaceous. Thus, this area was not affected by much vertical movement during the past 20 kyr.

The eastern shelf is <5 km wide in places, compared to the global average width of the shelf of 50 km (Shepard, 1963). O'Grady et al. (2000) classified parts of this shelf as a Type 2 sigmoid type, with a constantly increasing slopes till a certain maximum slope, followed by a decrease in slope. The eastern continental shelf is also steeper than the western continental shelf. The sequence boundary reported from the east coast of South Africa formed during the LGM and is defined by narrow paleovalleys which were formed during the exposure of the continental shelf because of the RSL fall. These valleys were later infilled with sediments when RSL started rising again (Green, 2009). All of these factors add up to formation of a characteristic narrow shelf. Inability to preserve entire sequences and high amplitude of RSL change can be a product of the narrow shelf, which is a characteristic of the eastern South African coast (Green, 2009).

The western coast extends from the Atlantic Ocean in the west to the mountains of the Great Escarpment in the east. It is a low-relief plain varying in width from ~20 km in the north to ~60 km in the south. The shelf margin is gentle and smooth with the slope of the shelf <2°, and O'Grady et al. (2000) classified this as a Type 1 or a gentle and smooth margin. The western coast of southern Africa mainly was influenced by sedimentation from the hinterland, with the southern part of the coast getting more deposits and northern part having thinner deposits due to the presence of mostly ephemeral streams in the arid Namib sand sea (Chase and Thomas, 2006).

The northern part of the western shelf receives very little sediment from the eolian processes in the Namib desert, whereas the eastern shelf and the southern part of the western shelf receives considerable sediment flux from the Limpopo (880 kg/s) and the Orange (725 kg/s) rivers, respectively (Cohen et al., 2014). A number of smaller rivers also flow into the eastern shelf, compared to the western shelf which only has a handful of rivers flowing into it (Fig 20).

Cosmogenic nuclide derived erosion rates for the study area is quite slow for the

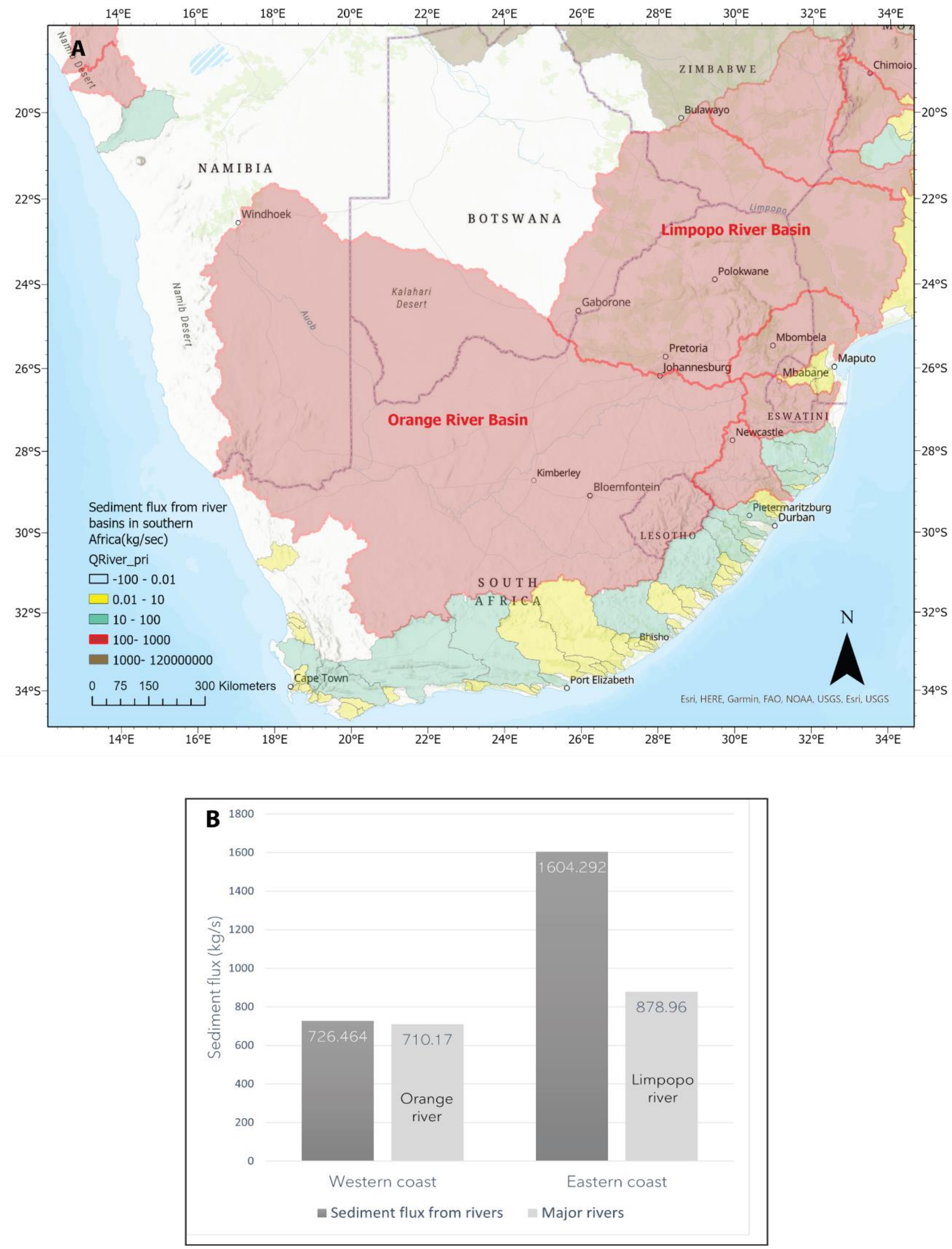

Figure 20. Comparison of sediment flux entering the coasts of southern Africa. Panel A shows the distribution of drainage basins in the study area, with the Orange and the Limpopo river basins marked in bold. All the river basins are colored according to their amount of riverine sediment flux. Panel B shows a plot showing a comparison of the riverine sediment flux. The western shelf presently receives ~55% less sediment than the eastern shelf. The sediment flux data have been collected from Nienhuis et al. (2020) and Cohen et al. (2014).

coastal plains as well as the inland plateau, averaging <10 m/Myr (Bierman et al., 2014; Chadwick et al., 2013; Cockburn et al., 2000; Makhubela et al., 2019).

2.3Data and methods

3.1 Southern African RSL database

The southern African RSL record published by Ramsay and Cooper (2002) is a compilation of a number of radiocarbon and U/Th ages for Pleistocene and Holocene RSL elevations from various parts of South Africa. However, these data do not have well-quantified uncertainties associated with them, nor are they presented in the form of a rigorous database. A recent Quaternary RSL record (Cooper et al., 2018) from South Africa is based on an RSL database using the HOLSEA protocol (Khan et al., 2019) similar to Hijma et al. (2015). A detailed look at this database raises a number of questions regarding the assignment of indicative meaning to the RSL data usage of various materials as RSL indicators, and the reservoir age correction in specific parts of the study area.

A new RSL database is presented here following the well-defined protocol of Hijma et al. (2015). The criteria for acceptance of datapoints and the database protocol are discussed in greater detail in Chapter 1 of this thesis. The dataset presented here is from the ~3000 km long southern African coastline and covers its eastern and western portions (Fig. 19). The western coast has a large number of samples reported from offshore whereas the data reported from the eastern coast are mostly onshore.

Articulated shells are the most common samples that have been dated (42%), followed by beachrock, other marine organisms and non-articulated shells (Fig. 21). Most of the articulated shells that have been dated do not have a very well-defined IR (Branch, 1981), disqualifying them as SLIPs. A summary of the indicative meanings for the different sample types accepted in the database is provided in Table 1. Bivalves like *Loripes clausus, Lutraria lutraria* and *Assiminea ovata* have been reported from the southern and western parts of the region. *Loripes clausus* is an estuarine species that occurs in the middle intertidal to subtidal zone and was sampled from the Keurbooms estuary (Reddering, 1988). *L. lutraria* and *A. ovata* are both marine species which occur on the continental shelf and thus can be used as lower LDPs. A fixed biological indicator in the form of an articulated barnacle (*Austromegabalanus cylindricus*) has been reported from Namibia (Compton, 2007), which is being treated as a lower LDP as well.

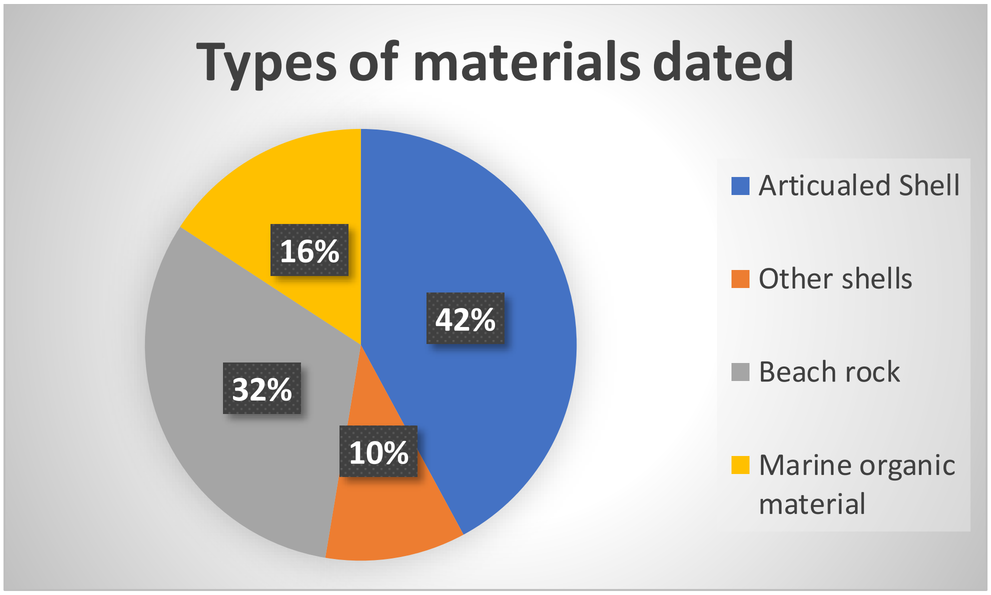

Figure 21 Proportion of different types of samples which have been used for this RSL database

The other major category of samples in this part of the world are beachrock deposits. A beachrock can be assigned as a SLIP only when a detailed description of its cement, sedimentary structures, location and sampling elevation are known, along with its age, obtained using either radiocarbon or OSL techniques (Mauz et al., 2015). The beachrock specimens that have been reported in South Africa mostly lack the necessary information about cement and sedimentary structures in the relevant publications. However, these beachrocks formed very close to MSL in the microtidal southern African coast with a narrow zone of contact between freshwater and seawater, which is a necessary condition for beachrock formation. Moreover, the type of cement and modern day beachrock analogues from the region also suggest their indicative meaning to be SLIPs (Green, *pers. comm.*, 2018) and thus the samples that were dated using the correct protocol have been classified as SLIPs in this database. The indicative meanings for the sea level indicators used for southern Africa are detailed in Table 2.2.

Table 2 Summary of the indicative meanings of the different sample types in southern Africa that have been accepted in the database

Sample type	Indicative meaning	Reference water level	Indicative range
Beachrock	Sea Level Index Points (SLIPs)	MLW	(HAT-LAT)/2
Life-position articulated bivalve	Lower LDP	MTL	-
Bulk marine OM	Lower LDP	MTL	-

Dating

Almost all the samples have been dated using ^{14}C, except one beachrock sample which was dated using U/Th and two beachrock samples using OSL. The ^{14}C ages have been reported in the publications using three different conventions. For about 50% of the ages reported, only the isotopic fractionation correction had been performed but not the reservoir age correction, which makes it easier to control the reservoir age correction at a later time, when there is better data regarding the reservoir age of the area. The marine reservoir effect depends on the prevalence of upwelling, sea surface temperature and depth of the mixed layer of water (Stuiver et al., 1986). Wood samples do not require reservoir corrections and their ages were only corrected for isotopic fractionation, and then calibrated using ShCal13, which is the calibration curve used for samples from the Southern Hemisphere (Reimer et al., 2013). I used the average ΔR of 146 ^{14}C yr following Dewar et al. (2012) for calculating the corrected ^{14}C age for the samples from the western coast of South Africa. However, this paper concerns the late Holocene, and a number of our samples are much older, so a reservoir age uncertainty of 200 ^{14}C yr has been used here instead of 85 ^{14}C yr as was reported. For the southern and eastern coasts, in almost all the publications concerning this area, the standard average reservoir age of 400 ^{14}C yr (i.e, $\Delta R=0$) has been used. However, a number of modeling studies like Franke et al. (2008) and Butzin et al. (2017) suggest that the ΔR for the eastern and southern shelf of southern Africa cannot be zero and there must be an error associated with the reservoir age. Compared to the western South African coast, which is characterized by upwelling and thus has a high ΔR, the eastern and southern coasts will have a much lower reservoir age error which was assumed to be 20±200 ^{14}C yr in this study, following the maximum and minimum variations of reservoir ages in a time-span of the last ~10 kyr that can be seen from the time series plots of reservoir age modeling studies (Butzin et al., 2017).

Once all the ages were corrected, I used OxCal (Bronk Ramsey, 2009, 2017) for calibrating the ^{14}C ages to calendar years, using the Marine13 (Reimer et al., 2013) calibration curve for the marine and estuarine samples and a combination of Marine13 and Shcal13 (Reimer et al., 2013) calibration curves for the beachrocks. The weighted mean calibrated ages were used. The 2σ age errors, rounded to the nearest 10 years are reported for both ^{14}C and OSL ages. The corrected U/Th age of the beachrock sample has been reported as is, rounded to the nearest 100 years, in absence of the raw U/Th age.

3.2 GIA model

To understand the shoreline position during the LGM in the study area, a GIA model has been utilized. A GIA model is a geophysical model used to calculate and predict past and future RSL curves, suitably adjusted for isostatic movements caused by glaciation and deglaciation (Bassett et al., 2005; Milne, 2015). During the Quaternary, the major influence on RSL change came from the mass exchange of water with continental ice sheets, due to the oscillation in ice volumes caused by Milankovich cycles.

Fourteen GIA model runs have been carried out with seven Earth models and two ice models, namely ICE-6G (Peltier et al., 2015) and the Bradley et al.

(2016) model, referred to here as EUST. A spherically symmetric Maxwell viscoelastic Earth model was used, with a number of combinations of lithospheric thickness and upper and lower mantle viscosities as shown in Table 2. These parameters were decided upon after careful consideration of the Earth model configurations used in the literature [e.g. (Bassett et al., 2005; Lambeck et al., 2014a; Milne and Peros, 2013; Mitrovica and Forte, 2004)].

Table 3. Earth model parameters used for the glacial isostatic adjustment.

Earth model Parameters	Values tested		
Lithospheric thickness (LT) (km)	71	96	120
Upper mantle viscosity (UMV) ($x10^{21}$ Pa s)	0.1	0.5	1
Lower mantle viscosity (LMV) ($x10^{22}$ Pa s)	1	10	50

3.3 Modeling the LGM shoreline and CSE

A paleo elevation dataset of the study area corresponding to 21 ka is generated from the GIA model, which was exported to the ArcGIS Pro software as a raster and then interpolated into a DEM using the Africa Albers equal area conic projection. The LGM shoreline for the study area is calculated from the 0 m depth contour. For the purposes of this thesis, the CSE is defined to be the first major downdip increase in slope from the continental shelf, as that will be the area first affected by fluvial incision, in the event of a RSL fall below it. Since it is impossible to assign one depth contour to the CSE, the first derivative of elevation, i.e., slope was calculated next using the ArcGIS Slope algorithm in the Spatial Analyst toolbar and it was seen that though a slope contour of 1 percent covers a major part of the CSE, it is not continuous enough to quantify the CSE in the entire study area. The rate of change of the slope with distance, i.e., the curvature was then calculated and the dip component (profile curvature) of the curvature values were contoured to choose the best suited value to quantify the CSE in the study area. Negative curvature values imply convex-up surfaces. Curvature serves to identify the location of the CSECSE in an objective and quantitative way. Once the curvature was calculated, the parameter was contoured to give us a straightforward way to quantify and compare CSE morphology. The entire southern African CSE can be quantified by a single curvature value, irrespective of the varying depth and morphology of the shelf, contrary to Törnqvist et.al. (2006) who found that curvature values had to differ significantly for morphologically different passive margins.

Creating topographic/bathymetric profiles along the southern African coast to understand the relationship between the LGM shoreline and the CSE is the next step to quantify the difference in horizontal and vertical distance between the shoreline and the CSE, and the change in elevation in the different parts of the study area. With respect to a reference frame, which in this case is a smooth baseline following the outline of the LGM shoreline, multiple perpendicular transects were projected intersecting the LGM shoreline and the CSE. The difference in both horizontal and vertical distance between the shoreline and CSE can be calculated once the topographic profiles are available.

Some processes, like morphological changes due to sedimentation, erosion or local tectonics since the LGM that affect topographic evolution of land/seascapes cannot be considered during this study. However, the study area is a quiescent passive margin [e.g. (De Wit, 2007; Tinker et al., 2008; Wildman et al., 2016; Wildman et al., 2017) and does not contain major depocenters. Nevertheless, we should be careful about these assumptions while analyzing the results from the topographic profiles.

Multiple topographic profiles (~60) were constructed in the study area connecting the LGM shoreline and CSE (the workflow is shown in Fig 22), and the locations of these transects are shown in the inset of Fig 6. These profiles were constructed both as a method to verify the location of the calculated LGM shelf edge (Fig 9) as well as to determine the distance between the CSE and the shoreline along the coast (Fig 10). In order to generate the transects needed to build the topographic/bathymetric profiles, a baseline was constructed by tracing a smoothed copy of the LGM shoreline 50 km inland from which the transects originated. From this baseline, using appropriate ArcGIS tools, 60 transects were created to cover the entire study area. The transects are long enough that they extend past both the CSE and shoreline.

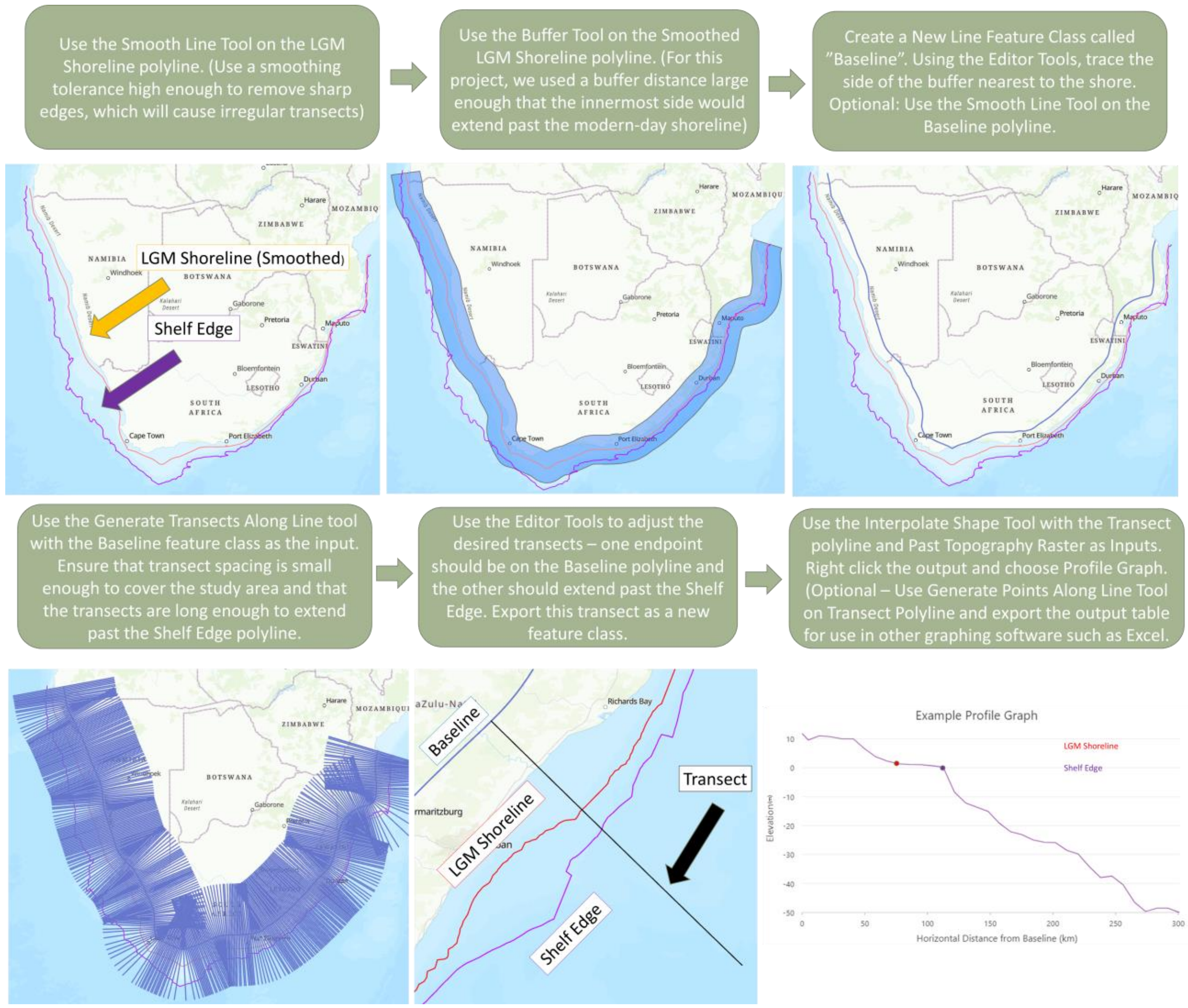

Figure 22 Workflow for generating transects along the coast of southern Africa

2.4Results and Discussion

<u>*Southern African RSL history*</u>

The RSL history of the area (Fig. 22) as seen from this dataset is restricted to the period between ~10 and ~5 ka, due to the absence of any suitable data before that time. A number of publications like Cooper et al. (2018) have attempted to describe the change in RSL during the time before 10 ka but most of these data are from geomorphic features on the submerged continental shelf which have not been dated. Using the protocol described in Chapter 1 of this thesis, the samples that are accepted are *in situ* and relatively uncompacted SLIPs as well as LDPs. The criteria for 2σ vertical and horizontal resolution have been relaxed in the case of the SLIPs and LDPs of southern Africa because the aim of this project is to mainly reconstruct an RSL history for the study area between 21 and 5 ka and then use that to choose the best performing GIA model as the paleotopographic dataset. The RSL database contains 61 data points from both the eastern and the western coasts of South Africa dating from 21 to 5 ka, collated from various published works spanning from 1971 to 2002. Out of these, only 17 data points can be used confidently to reconstruct the RSL history of the area (Fig. 22). The rest is unsuitable for this exercise and have been discarded mainly due to issues regarding sampling, dating and documentation, since they *do not* follow our protocol (as discussed in Chapter 1). The RSL history in the western and southern parts of the study area are mainly described using biological samples as LDPs, while the SLIPs are the beachrock samples from the eastern coast. In Fig 22, the SLIPs are represented by crosses, with the horizontal bar representing the 2σ age range and the vertical bar representing the upward and downward errors of elevation. For the T-shaped lower LDPs, the horizontal bar represents the 2σ age range, but the vertical bar represents the sum of the upward and downward errorss.

A number of shells whose ages are in the range of ~21 to ~14 ka have been collected from the continental shelf in this region, but they are also not considered because they are most certainly *ex situ*. Between 14 ka and 5 ka, the RSL plots from Cooper et al. (2018) show 17 SLIPs and 11 lower LDPs, from both the eastern and western coasts of the area (Fig. 23). It is quite impossible to track down each of these data points in their database, because of the lack of clarity about their definition of SLIPs and LDPs. In their spreadsheet, none of their data are clearly marked as SLIPs or LDP. Such a drastic difference in the number of SLIPs in the two databases introduces conservative uncertainty to the RSL history described by the present database. Apart from the issue of documentation, the present dataset uses different criteria than the Cooper et al. (2018) dataset for defining SLIPs and lower LDP, which is the major reason behind the differences in the two databases. Differences have also arisen due to the different reservoir ages used and inaccessibility to certain data for the present database.

Most of the publications define the LGM in South Africa using shells which are dredged from the continental shelf (Vogel and Marais, 1971; Pether, 1994; Ramsay and Cooper, 2002) or from undated submerged beach ridges at -120 m (Green and Uken, 2005; Cooper et al., 2018), which are discarded here. Also, the RSL history of the eastern coast of the study area is described by 5 SLIPs assigned to beachrocks dated with radiocarbon and OSL, while the one U/Th dated beachrock has been disregarded in this dataset since it was a whole rock date which is not useful in case of RSL studies from beachrocks, due to significant geochemical alterations (Mauz et al., 2015).

From 10 to 8.5 ka, RSL rose by ~9m as seen from the SLIPs on the eastern coast. Between ~8.5 ka and ~7.2 ka, the RSL rise slows down a little. Following this period, until ~6 ka, the RSL data show a highstand ~1.5 m above present MSL at ~6 ka, signifying the mid-Holocene highstand, which is expected in an equatorial ocean basin like the one discussed here (Cooper et al., 2018; Mitrovica and Milne, 2002). The time period from 6 to 5 ka are only described in the present database with lower LDPs. In Cooper et al. (2018), the RSL history shows a rise between 6 ka and 5 ka, based on a few SLIPs, which is not seen in the present database (Fig. 24).

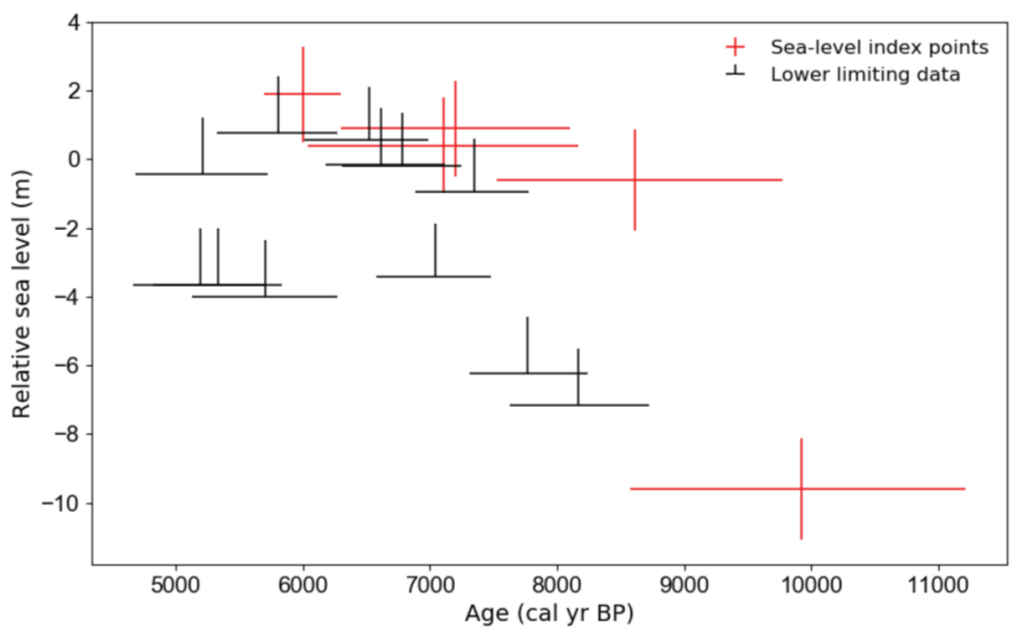

Figure 23 Relative RSL plot from southern Africa

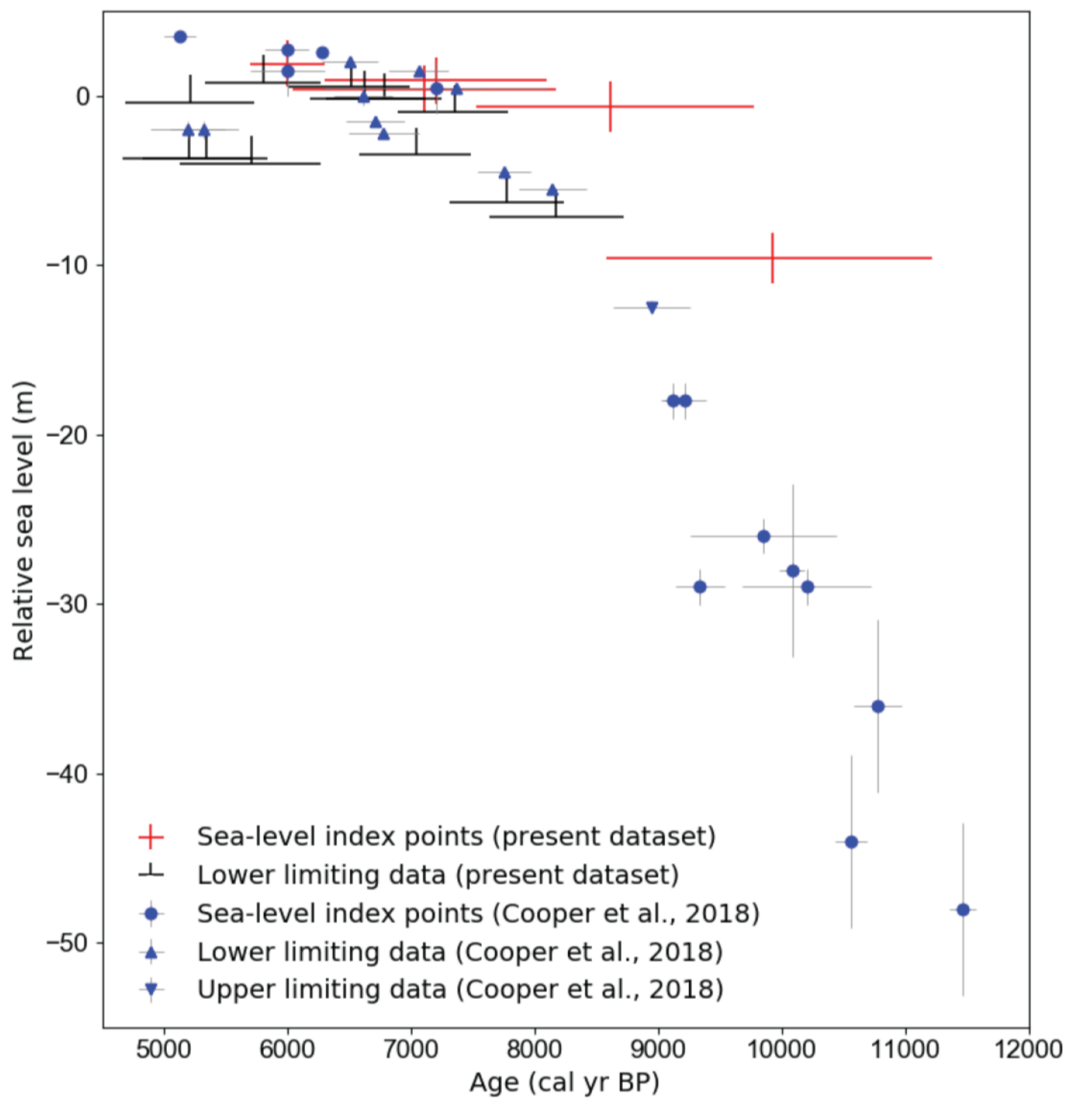

Figure 24 Comparison between the present database, shown in red and Cooper et al. (2018) database, shown in black

Data-model comparison

Using the RSL history from the database as described in the previous section, an RSL data-GIA model comparison has been done for the southern African region.

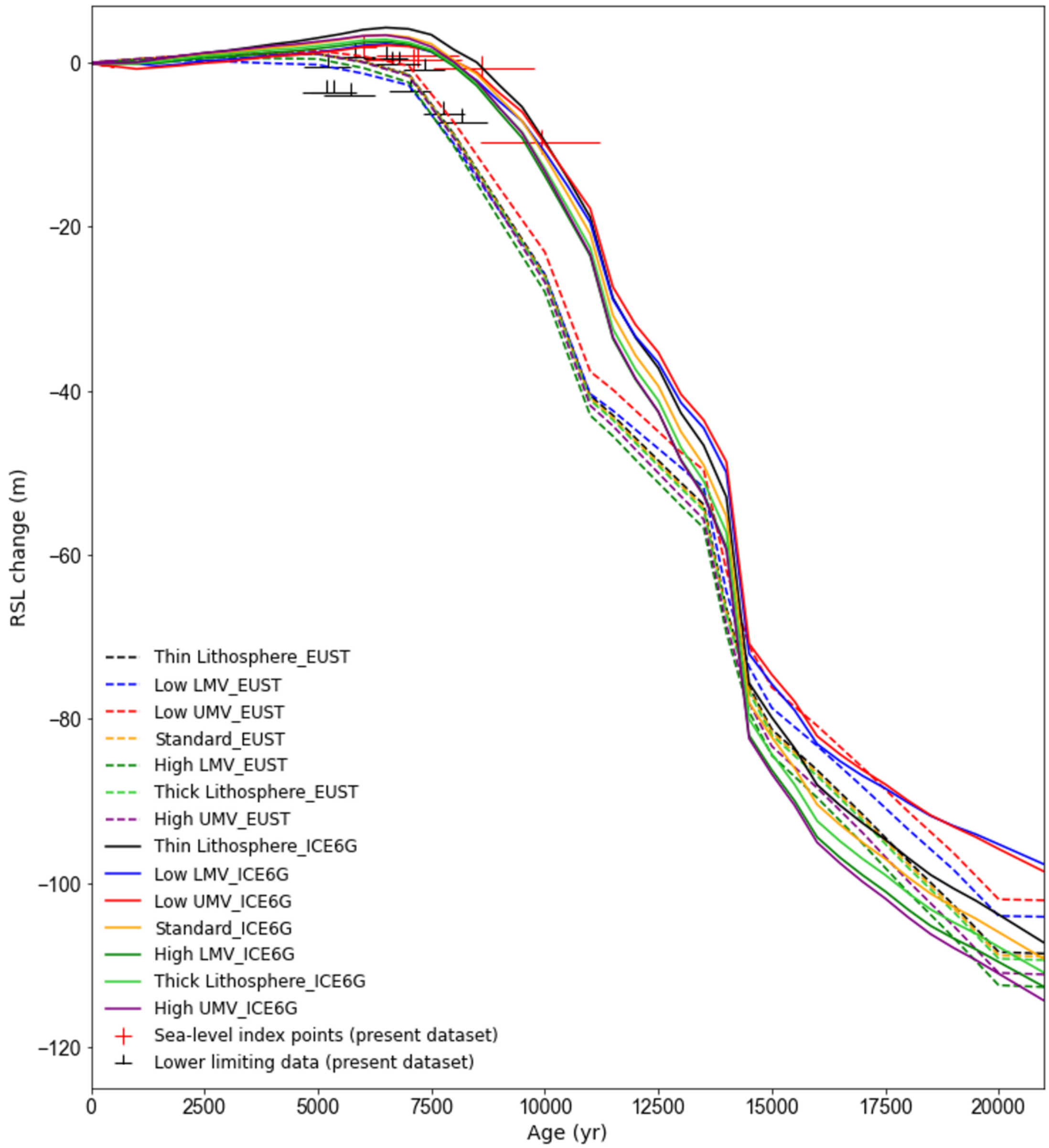

Figure 25 Comparison between the relative sea level history calculated from the data collected from the study area and the glacial isostatic adjustment models, using two different ice models and seven different Earth models.

The result of this data-model comparison is shown in Fig. 25. The GIA models using ICE-6G produce a better fit than the ones using EUST with the southern African RSL history, as reconstructed from the RSL database. All the five SLIPs from the database plot on the RSL predictions calculated from the GIA models using ICE-6G, irrespective of the Earth model used. The lower LDP also plots below these RSL predictions, signifying a good fit with the data. Even though in the first chapter of this thesis I have shown that ICE-6G falls short when it comes to understanding early Holocene meltwater partitioning, this ice model performs better in recreating the RSL history in southern Africa, as shown here. On the other hand, the RSL predictions from GIA models using the EUST ice model plots lower than the SLIPs from the RSL database, underpredicting the RSL history of southern Africa. Following this data-model comparison, to generate a paleotopography dataset from the GIA model, ICE-6G is used as the preferred ice model with a 96-km thick elastic lithosphere for the Earth's viscosity model, with an upper mantle viscosity of $5x10^{20}$ Pa s and a lower mantle viscosity of 10^{20} Pa s. However, the predicted RSL curves using different Earth models and ICE-6G show a wide spread of RSL values (~120-~100m) at LGM. Without well-constrained SLIPs from the LGM,we cannot choose the Earth model that will give us the best fit. This also affects the depth of the modeled LGM shoreline from the paleotopography generated and is a limitation of this study.

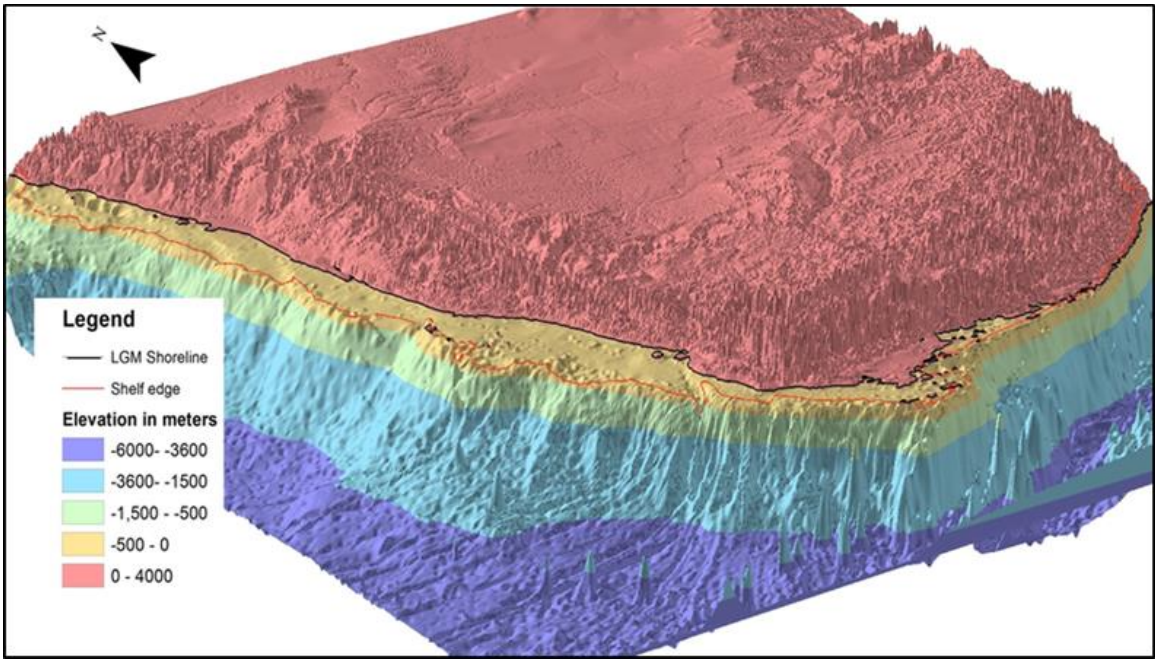

Figure 26 Three-dimensional view of the land/seascape of southern Africa with the LGM shoreline and the CSE which is outlined by the curvature contour of -3x10^{-5}. The 3D model has been 40% vertically exaggerated

Relationship between LGM shoreline and CSE

The LGM CSE and the shoreline were modeled for the western coast and eastern coast of southern Africa and the coast of Mozambique. As discussed in

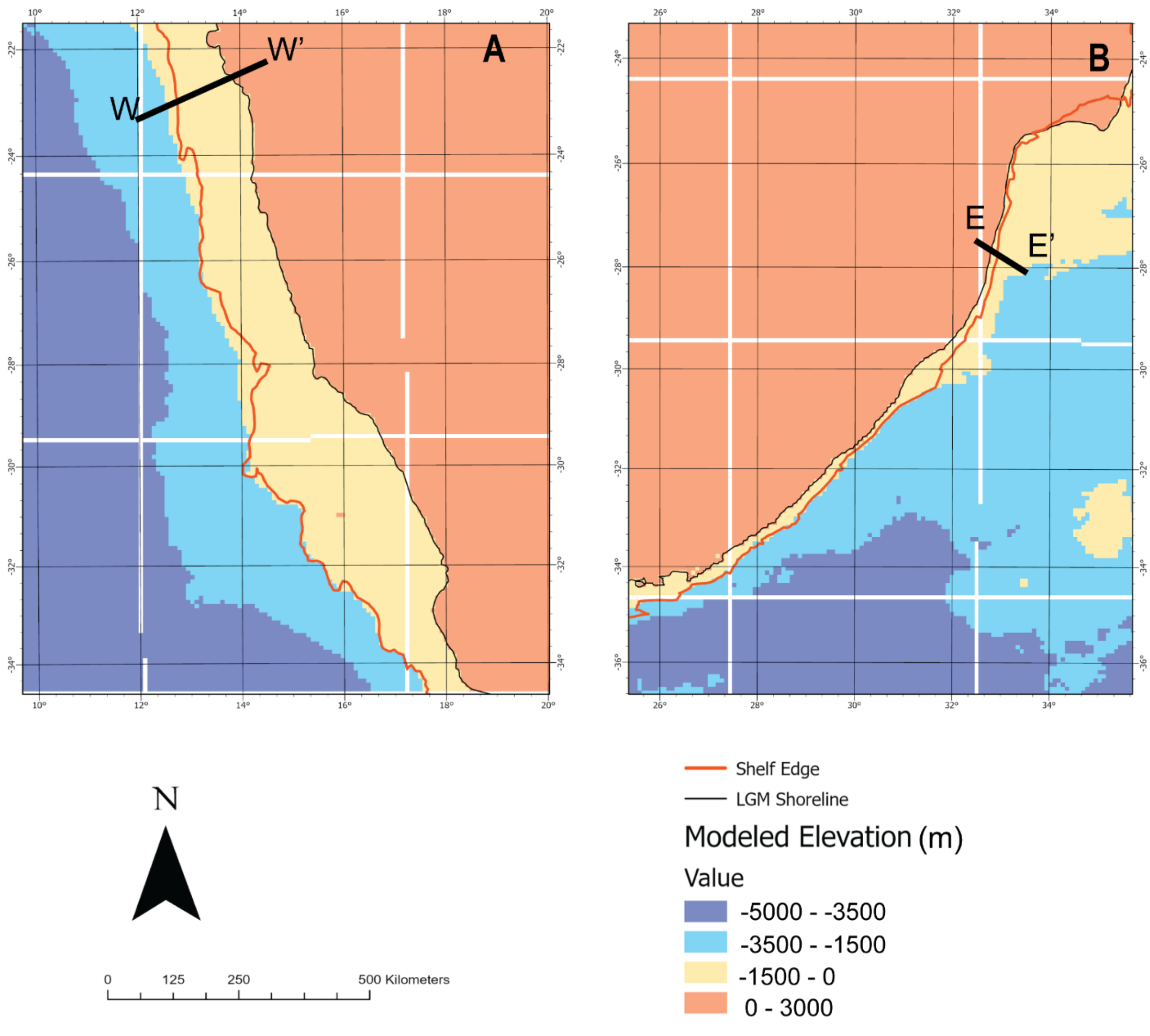

Figure 27 The relationship between shoreline and CSE during the LGM in different parts of southern Africa. A shows a view of the western shelf where the shoreline remained considerably landward from the shelf edge. B shows a view of the eastern shelf where the shoreline was very close to shelf edge and in the north, the sea-level fell below the shelf edge. The lines W-W' and E-E' in the figure show the position of the topographic profile plots shown in Fig 28

section 2.2, the present-day western shelf of Southern Africa is wider than the eastern shelf, and we can see that the situation was the same 20 kyr ago. In the

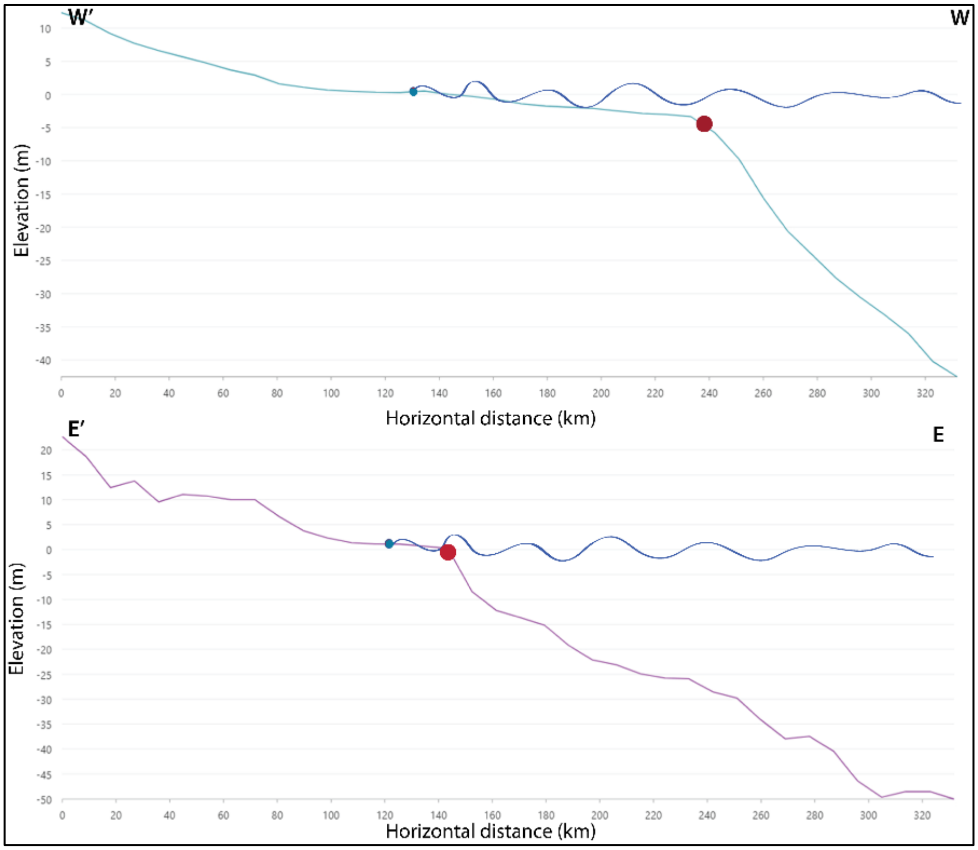

Figure 28 Topographic profiles the western coast (W-W')) in the top panel and for the eastern coast (E-E') in the bottom panel. The red dots in the plots show the position of the LGM continental shelf and the blue dot with the wave shows the position of the LGM shoreline

western part of the study area, there was a wide separation between the shoreline and the CSE during the LGM and the lowstand shoreline remained on the shelf (Fig 28A), the situation being comparable to Bay of Biscay and the one illustrated in Fig 18A. As expected, fluvial incision during the LGM is not reported from this part of Africa (Green and Uken, 2005). In contrast, the lowstand shoreline and the CSE were situated in proximity to each other in the eastern part of the study area (Fig 28B), at places the shoreline crossing the CSE and being positioned on the continental slope, similar to the situation portrayed in Fig 18B. As seen also in the Gulf of Mexico, this type of condition encourages fluvial incision and a number of cross-shelf paleovalleys are reported from eastern Africa from around 21 ka (Green, 2009; Green and Uken, 2005).

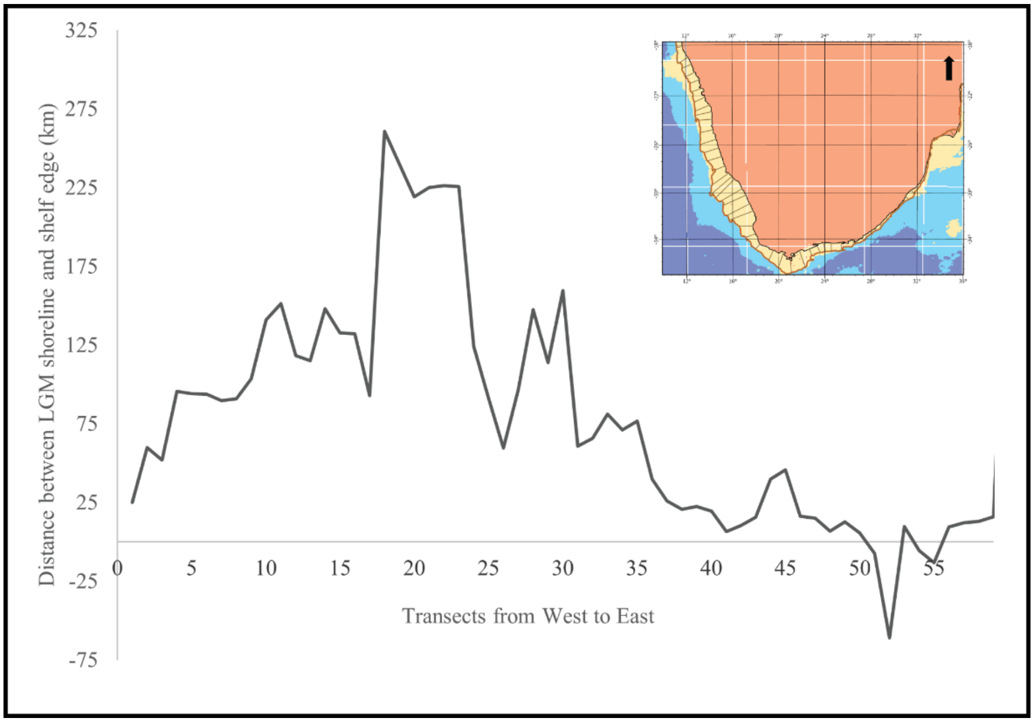

Figure 29 Plot showing the distance between the CSE and the LGM shoreline for the study area. The distances were measured for 60 transects, starting from the west to the east.

Fig 28A shows the topographic profile from the west coast of southern Africa (W-W′) where the shoreline was situated more than 100 km landward from the shelf edge. For the topographic profile from the east coast (E-E′), the LGM shoreline is only situated about 20 km landward from the CSE (Fig 28B). From Figs 27 and 29, we see that there are some locations along the eastern coast of southern Africa, where the LGM shoreline was situated seaward of the CSE. The average distance between the CSE and the shoreline for the western and eastern coast are ~130 km and ~20 km respectively, which are significantly different. It should also be pointed out that some LGM shoreline- CSE distances plotted in Fig 29 are shown as negative numbers which are the locations from the study area where the shoreline was situated seaward of the CSE during the LGM. The maximum and minimum distances between the two geomorphic features are ~260 km and ~-60 km respectively.

The different distances between the LGM CSE and shoreline in the two coasts of southern Africa adds to the idea that there are multiple situations that can arise during a lowstand sea level cycle and even though conventional sequence stratigraphic models predict it, a paleovalley may not be incised during this time at most locations, as has been also demonstrated earlier (Törnqvist et al., 2006). This also raises questions about the fate of sediments making it into the deeper parts of the ocean during lower sea level. During the LGM, rivers and their sediment loads were trapped on the continental shelves, instead of connecting the source to the subaqueous sinks. The numerical model study by Harris et al. (2018) also shows that the connection between sea level fall and deep marine sedimentation is not so simple as it does not take into account other factors including accommodation on the shelf. Even though the African coast is not as well-studied as other margins, seismic studies like Wenau et al. (2020) show the presence of a lowstand sediment wedge on the continental slope right offshore of the CSE, followed by deposition of sediments on the eastern CSE around the LGM. The inner western shelf, however, has been described as generally sediment-free and rocky with exposed Late Proterozoic rocks and with limited Cenozoic aggradation (Kirkpatrick et al., 2019). A number of smaller point sources of sediment, with the presence of the Limpopo River, would accumulate enough sediment to the eastern shelf to prograde the CSE, in comparison to the western shelf, which is nearly only fed by the Orange River. Our study shows that there is a possibility that the deeper ocean might not have received as much sediments as was expected during LGM. Extrapolating this to the ancient rock record, both interpretation of stratigraphic boundaries, more specifically sequence boundaries, as well as older eustatic cycles might be more complex than it is presumed. Using easily calculated geomorphic parameters involving the morphology of the CSE, this project seeks to answer questions about how the riverine sediments can reach the deeper marine sinks during sea-level low stands (Amorosi et al., 2016; Bhattacharya et al., 2016). These geomorphic parameters can also add to the ongoing morphometric analysis about the CSE (Harris and Macmillan-Lawler, 2016; O'Grady et al., 2000). Understanding deep-time S2S sedimentation can also be a potential outcome of this work (Bhattacharya et al., 2016; Nyberg et al., 2018).

The preservation of OC depends on how quickly the sediments are buried so as to reduce oxidation, which can be achieved by high rates of sediment accumulation on the continental shelf and in the deeper ocean. At present, in certain active margins, OC rapidly gets transferred to the deeper ocean where it is buried, resulting in low exposure to oxidation and thus preservation in the muddy facies [for e.g., (Kao et al., 2014; Leithold and Hope, 1999)]. Along the passive margins, however, with the present-day higher sea level and the wider shelves compared to LGM, rivers either form a shoreline bulge or a subaqueous deltaic clinoforms. Only in the areas where rapid sediment deposition is happening, OC is buried quickly enough to have a high OC burial efficiency (Galy et al., 2007; Goni et al., 2014; Leithold et al., 2016). During the LGM, the passive margin on the eastern coast of southern Africa had a really narrow shelf with the shoreline being close to the CSE. In situations like these, during RSL lowstand, the OC along with the sediments would have been able to be deposited in the deeper ocean, probably leading to higher burial efficiency and better preservation of the OC. But in case of a situation like the western coast, where the sediments would be stuck on the shelf, the OC might have been remineralized due to waves and currents resuspending them in the comparatively shallow water, especially during glacials with lower RSL. Some work has been done to report that during this time there was an increase in rate of upwelling for the Benguela current (Lavik, 2001; Little et al., 1997), which should cause higher resuspension due to stronger currents and wave activities.

An increase in the terrestrial carbon stock has also been proposed for the time between LGM to the pre-industrial period (Jeltsch-Thömmes et al., 2018; Köhler and Fischer, 2004). However, a number of variables about land carbon stock is still unresolved due to lack of effective reconstructions, both proxy-based or modeled, which can be speculative in nature. The modeling studies done to calculate the amount of carbon stored in the continental shelves are complicated by the different rates of relative sea-level rise and GIA, which would affect the actual area of the exposed shelves in the different parts of the world (Faure et al., 1996; Montenegro et al., 2006). The modeling studies done by Montenegro et al. (2006) uses ICE-5G to calculate the exposed shelf area. But a more accurate approach to calculate the shelf area would be the process we have followed here, which starts with reconstructing the RSL history of a study and using a GIA model whose RSL history matches the history reconstructed from the RSL data as a paleotopography dataset. The workflow developed using the southern African dataset can be used on other similar passive margins to answer these questions.

Conclusion

In this chapter, I show that higher sediment flux and smaller distance between the shoreline and CSE during lowstand sea level is essential for progradation of CSE. Using relatively simple parameters involving the morphology of the CSE, this work answers questions about whether riverine sediments always reach the deeper marine sinks during sea-level lowstands. This study has widespread implications including sequence stratigraphy and offshore burial of organic matter with possible implications for the global carbon cycle.

Amante, C., and Eakins, B. W., 2009, ETOPO1 arc-minute global relief model: procedures, data sources and analysis.
Amorosi, A., Maselli, V., and Trincardi, F., 2016, Onshore to offshore anatomy of a late Quaternary source-to-sink system (Po Plain–Adriatic Sea, Italy): Earth-Science Reviews, v. 153, p. 212-237.
Anderson, J. B., Wallace, D. J., Simms, A. R., Rodriguez, A. B., Weight, R. W., and Taha, Z. P., 2016, Recycling sediments between source and sink during a eustatic cycle: Systems of late Quaternary northwestern Gulf of Mexico Basin: Earth-science reviews, v. 153, p. 111-138.
Bassett, S. E., Milne, G. A., Mitrovica, J. X., and Clark, P. U., 2005, Ice sheet and solid earth influences on far-field sea-level histories: Science, v. 309, no. 5736, p. 925-928.
Bhattacharya, J. P., Copeland, P., Lawton, T. F., and Holbrook, J., 2016, Estimation of source area, river paleo-discharge, paleoslope, and sediment budgets of linked deep-time depositional systems and implications for hydrocarbon potential: Earth-Science Reviews, v. 153, p. 77-110.
Bierman, P. R., Coppersmith, R., Hanson, K., Neveling, J., Portenga, E. W., and Rood, D. H., 2014, A cosmogenic view of erosion, relief generation, and the age of faulting in southern Africa.
Blair, N. E., and Aller, R. C., 2012, The fate of terrestrial organic carbon in the marine environment: Annual review of marine science, v. 4, p. 401-423.
Blum, M., Martin, J., Milliken, K., and Garvin, M., 2013, Paleovalley systems: insights from Quaternary analogs and experiments: Earth-Science Reviews, v. 116, p. 128-169.
Blum, M. D., and Törnqvist, T. E., 2000, Fluvial responses to climate and sea-level change: a review and look forward: Sedimentology, v. 47, no. s1, p. 2-48.
Bradley, S. L., Milne, G. A., Horton, B. P., and Zong, Y., 2016, Modelling sea level data from China and Malay-Thailand to estimate Holocene ice-volume equivalent sea level change: Quaternary Science Reviews, v. 137, p. 54-68.
Branch, M., 1981, The living shores of southern Africa, Struik publishers.
Braun, J., Guillocheau, F., Robin, C., Baby, G., and Jelsma, H., 2014, Rapid erosion of the Southern African Plateau as it climbs over a mantle superswell: Journal of Geophysical Research: Solid Earth, v. 119, no. 7, p. 6093-6112.
Bronk Ramsey, C., 2009, Bayesian analysis of radiocarbon dates: Radiocarbon, v. 51, no. 1, p. 337-360.
-, 2017, OxCal 4.3. 2. 2017.
Burdige, D. J., 2005, Burial of terrestrial organic matter in marine sediments: A re-assessment: Global Biogeochemical Cycles, v. 19, no. 4.

Burgess, P. M., and Hovius, N., 1998, Rates of delta progradation during highstands: consequences for timing of deposition in deep-marine systems: Journal of the Geological Society, v. 155, no. 2, p. 217-222.

Butzin, M., Köhler, P., and Lohmann, G., 2017, Marine radiocarbon reservoir age simulations for the past 50,000 years: Geophysical Research Letters, v. 44, no. 16, p. 8473-8480.

Catuneanu, O., Abreu, V., Bhattacharya, J. P., Blum, M. D., Dalrymple, R. W., Eriksson, P. G., Fielding, C. R., Fisher, W. L., Galloway, W. E., Gibling, M. R., Giles, K. A., Holbrook, J. M., Jordan, R., Kendall, C. G. S. C., Macurda, B., Martinsen, O. J., Miall, A. D., Neal, J. E., Nummedal, D., Pomar, L., Posamentier, H. W., Pratt, B. R., Sarg, J. F., Shanley, K. W., Steel, R. J., Strasser, A., Tucker, M. E., and Winker, C., 2009, Towards the standardization of sequence stratigraphy: Earth-Science Reviews, v. 92, no. 1, p. 1-33.

Chadwick, O. A., Roering, J. J., Heimsath, A. M., Levick, S. R., Asner, G. P., and Khomo, L., 2013, Shaping post-orogenic landscapes by climate and chemical weathering: Geology, v. 41, no. 11, p. 1171-1174.

Chase, B. M., and Thomas, D. S., 2006, Late Quaternary dune accumulation along the western margin of South Africa: distinguishing forcing mechanisms through the analysis of migratory dune forms: Earth and Planetary Science Letters, v. 251, no. 3-4, p. 318-333.

Chiocci, F. L., and Chivas, A. R., 2014, An overview of the continental shelves of the world: Geological Society, London, Memoirs, v. 41, no. 1, p. 1-5.

Cockburn, H., Brown, R., Summerfield, M., and Seidl, M., 2000, Quantifying passive margin denudation and landscape development using a combined fission-track thermochronology and cosmogenic isotope analysis approach: Earth and Planetary Science Letters, v. 179, no. 3-4, p. 429-435.

Cohen, S., Kettner, A. J., and Syvitski, J. P., 2014, Global suspended sediment and water discharge dynamics between 1960 and 2010: Continental trends and intra-basin sensitivity: global and planetary change, v. 115, p. 44-58.

Compton, J. S., 2007, Holocene evolution of the Anichab Pan on the south-west coast of Namibia: Sedimentology, v. 54, no. 1, p. 55-70.

Cooper, J., Green, A., and Compton, J., 2018, Sea-level change in southern Africa since the Last Glacial Maximum: Quaternary Science Reviews, v. 201, p. 303-318.

De Wit, M., 2007, The Kalahari Epeirogeny and climate change: differentiating cause and effect from core to space: South African Journal of Geology, v. 110, no. 2-3, p. 367-392.

Dewar, G., Reimer, P. J., Sealy, J., and Woodborne, S., 2012, Late-Holocene marine radiocarbon reservoir correction (ΔR) for the west coast of South Africa: The Holocene, v. 22, no. 12, p. 1481-1489.

Faure, H., Adams, J., Debenay, J., Faure-Denard, L., Grants, D., Pirazzoli, P., Thomassin, B., Velichko, A., and Zazo, C., 1996, Carbon storage and continental land surface change since the last glacial maximum: Quaternary Science Reviews, v. 15, no. 8-9, p. 843-849.

Franke, J., Paul, A., and Schulz, M., 2008, Modeling variations of marine reservoir ages during the last 45 000 years: Climate of the Past Discussions, v. 4, no. 1, p. 81-110.

Galy, V., France-Lanord, C., Beyssac, O., Faure, P., Kudrass, H., and Palhol, F., 2007, Efficient organic carbon burial in the Bengal fan sustained by the Himalayan erosional system: Nature, v. 450, no. 7168, p. 407-410.

Goni, M. A., Moore, E., Kurtz, A., Portier, E., Alleau, Y., and Merrell, D., 2014, Organic matter compositions and loadings in soils and sediments along the Fly River, Papua New Guinea: Geochimica et Cosmochimica Acta, v. 140, p. 275-296.

Green, A., 2009, Palaeo-drainage, incised valley fills and transgressive systems tract sedimentation of the northern KwaZulu-Natal continental shelf, South Africa, SW Indian Ocean: Marine Geology, v. 263, no. 1-4, p. 46-63.

Green, A. N., and Uken, R., 2005, First observations of sea-level indicators related to glacial maxima at Sodwana Bay, northern KwaZulu-Natal: Research in action: South African Journal of Science, v. 101, no. 5-6, p. 236-238.

Harris, A. D., Baumgardner, S. E., Sun, T., and Granjeon, D., 2018, A Poor Relationship Between Sea Level and Deep-Water Sand Delivery: Sedimentary Geology, v. 370, p. 42-51.

Harris, P. T., and Macmillan-Lawler, M., 2016, Global Overview of Continental Shelf Geomorphology Based on the SRTM30_PLUS 30-Arc Second Database, *in* Finkl, C. W., and Makowski, C., eds., Seafloor Mapping along Continental Shelves: Research and Techniques for Visualizing Benthic Environments: Cham, Springer International Publishing, p. 169-190.

Helland-Hansen, W., Steel, R. J., and Sømme, T. O., 2012, Shelf genesis revisited: Journal of Sedimentary Research, v. 82, no. 3, p. 133-148.

Hijma, M. P., Engelhart, S. E., Törnqvist, T. E., Horton, B. P., Hu, P., and Hill, D. F., 2015, A protocol for a geological sea-level database: Handbook of Sea-Level Research, edited by: Shennan, I., Long, AJ, and Horton, BP, Wiley Blackwell, p. 536-553.

Hutton, J., 1788, X. Theory of the Earth; or an Investigation of the Laws observable in the Composition, Dissolution, and Restoration of Land upon the Globe: Earth and Environmental Science Transactions of The Royal Society of Edinburgh, v. 1, no. 2, p. 209-304.

Jeltsch-Thömmes, A., Battaglia, G., Cartapanis, O., Jaccard, S. L., and Joos, F., 2018, A large increase in the carbon inventory of the land biosphere since the Last Glacial Maximum: constraints from multi-proxy data.

Kao, S.-J., Hilton, R., Selvaraj, K., Dai, M., Zehetner, F., Huang, J.-C., Hsu, S.-C., Sparkes, R., Liu, J., and Lee, T.-Y., 2014, Preservation of terrestrial organic carbon in marine sediments offshore Taiwan: mountain building and atmospheric carbon dioxide sequestration: Earth Surface Dynamics, v. 2, no. 1, p. 127-139.

Kirkpatrick, L. H., Green, A. N., and Pether, J., 2019, The seismic stratigraphy of the inner shelf of southern Namibia: the development of an unusual nearshore shelf stratigraphy: Marine Geology, v. 408, p. 18-35.

Köhler, P., and Fischer, H., 2004, Simulating changes in the terrestrial biosphere during the last glacial/interglacial transition: Global and Planetary Change, v. 43, no. 1-2, p. 33-55.

Lambeck, K., Rouby, H., Purcell, A., Sun, Y., and Sambridge, M., 2014, Sea level and global ice volumes from the Last Glacial Maximum to the Holocene: Proceedings of the National Academy of Sciences, v. 111, no. 43, p. 15296-15303.

Laugier, F. J., and Plink-Björklund, P., 2016, Defining the shelf edge and the three-dimensional shelf edge to slope facies variability in shelf-edge deltas: Sedimentology, v. 63, no. 5, p. 1280-1320.

Lavik, G., 2001, Nitrogen isotopes of sinking matter and sediments in the South Atlantic.

Leithold, E. L., Blair, N. E., and Wegmann, K. W., 2016, Source-to-sink sedimentary systems and global carbon burial: A river runs through it: Earth-Science Reviews, v. 153, p. 30-42.

Leithold, E. L., and Hope, R. S., 1999, Deposition and modification of a flood layer on the northern California shelf: lessons from and about the fate of terrestrial particulate organic carbon: Marine Geology, v. 154, no. 1-4, p. 183-195.

Little, M. G., Schneider, R. R., Kroon, D., Price, B., Summerhayes, C. P., and Segl, M., 1997, Trade wind forcing of upwelling, seasonally, and Heinrich events as a response to sub-Milankovitch climate variability: Paleoceanography, v. 12, no. 4, p. 568-576.

Ludwig, W., Probst, J. L., and Kempe, S., 1996, Predicting the oceanic input of organic carbon by continental erosion: Global Biogeochemical Cycles, v. 10, no. 1, p. 23-41.

Makhubela, T., Kramers, J., Scherler, D., Wittmann, H., Dirks, P., and Winkler, S., 2019, Effects of long soil surface residence times on apparent cosmogenic nuclide denudation rates and burial ages in the Cradle of Humankind, South Africa: Earth Surface Processes and Landforms, v. 44, no. 15, p. 2968-2981.

Milne, G. A., 2015, Glacial isostatic adjustment: Handbook of sea-level research. Wiley, Chichester, p. 421-437.

Milne, G. A., and Peros, M., 2013, Data–model comparison of Holocene sea-level change in the circum-Caribbean region: Global and Planetary Change, v. 107, p. 119-131.

Mitrovica, J., and Milne, G., 2002, On the origin of late Holocene sea-level highstands within equatorial ocean basins: Quaternary Science Reviews, v. 21, no. 20-22, p. 2179-2190.

Mitrovica, J. X., and Forte, A. M., 2004, A new inference of mantle viscosity based upon joint inversion of convection and glacial isostatic adjustment data: Earth and Planetary Science Letters, v. 225, no. 1, p. 177-189.

Molnar, P., England, P. C., and Jones, C. H., 2015, Mantle dynamics, isostasy, and the support of high terrain: Journal of Geophysical Research: Solid Earth, v. 120, no. 3, p. 1932-1957.

Montenegro, A., Eby, M., Kaplan, J. O., Meissner, K. J., and Weaver, A. J., 2006, Carbon storage on exposed continental shelves during the glacial-interglacial transition: Geophysical Research Letters, v. 33, no. 8.

Nienhuis, J. H., Ashton, A. D., Edmonds, D. A., Hoitink, A., Kettner, A. J., Rowland, J. C., and Törnqvist, T. E., 2020, Global-scale human impact on delta morphology has led to net land area gain: Nature, v. 577, no. 7791, p. 514-518.

Nyberg, B., Helland-Hansen, W., Gawthorpe, R. L., Sandbakken, P., Eide, C. H., Sømme, T., Hadler-Jacobsen, F., and Leiknes, S., 2018, Revisiting morphological relationships of modern source-to-sink segments as a first-order approach to scale ancient sedimentary systems: Sedimentary Geology, v. 373, p. 111-133.

O'Grady, D. B., Syvitski, J. P., Pratson, L. F., and Sarg, J., 2000, Categorizing the morphologic variability of siliciclastic passive continental margins: Geology, v. 28, no. 3, p. 207-210.

Peltier, W. R., Argus, D., and Drummond, R., 2015, Space geodesy constrains ice age terminal deglaciation: The global ICE-6G_C (VM5a) model: Journal of Geophysical Research: Solid Earth, v. 120, no. 1, p. 450-487.

Porębski, S. J., and Steel, R. J., 2003, Shelf-margin deltas: their stratigraphic significance and relation to deepwater sands: Earth-Science Reviews, v. 62, no. 3-4, p. 283-326.

Posamentier, H., Allen, G., and James, D., 1992, Forced regressions in a sequence stratigraphic framework: concepts, examples, and exploration significance (1): The American Association of Petroleum Geologists Bulletin, v. 76, no. 11, p. 1687-1709.

Posamentier, H. W., 2001, Lowstand alluvial bypass systems: incised vs. unincised: AAPG bulletin, v. 85, no. 10, p. 1771-1793.

Posamentier, H. W., and Vail, P. R., 1988a, Eustatic controls on clastic deposition II - sequence and systems tract models, *in* Wilgus, C. K., Hastings, B. S., Posamentier, H. P., Van Wagoner, J. V., Ross, C. A., and Kendall, C. G. S. C., eds., Sea-Level Changes, SEPM special publicaiton 42, p. 125-154.

-, 1988b, Eustatic Controls on Clastic Deposition II—sequence and Systems Tract Models: SEPM Special Publications, p. 125-154.

Reddering, J., 1988, Evidence for a middle Holocene transgression, Keurbooms estuary, South Africa: Palaeoecology of Africa, v. 19, p. 79-86.

Reimer, P. J., Bard, E., Bayliss, A., Beck, J. W., Blackwell, P. G., Ramsey, C. B., Buck, C. E., Cheng, H., Edwards, R. L., and Friedrich, M., 2013, IntCal13 and Marine13 radiocarbon age calibration curves 0–50,000 years cal BP: Radiocarbon, v. 55, no. 4, p. 1869-1887.

Ritsema, J., Ni, S., Helmberger, D. V., and Crotwell, H. P., 1998, Evidence for strong shear velocity reductions and velocity gradients in the lower mantle beneath Africa: Geophysical Research Letters, v. 25, no. 23, p. 4245-4248.

Schumm, S., 1993, River response to baselevel change: implications for sequence stratigraphy: The Journal of Geology, v. 101, no. 2, p. 279-294.

Schumm, S. A., 1977, The fluvial system, Wiley New York.

Shepard, F. P., 1963, Importance of submarine valleys in funneling sediments to the deep sea: Progress in oceanography, v. 3, p. 321-332.

Stanley, J. R., Braun, J., Baby, G., Guillocheau, F., Robin, C., Flowers, R. M., Brown, R., Wildman, M., and Beucher, R., 2021, Constraining plateau uplift in southern Africa by combining thermochronology, sediment flux, topography, and landscape evolution modeling: Journal of Geophysical Research: Solid Earth, v. 126, no. 7, p. e2020JB021243.

Stuiver, M., Pearson, G. W., and Braziunas, T., 1986, Radiocarbon age calibration of marine samples back to 9000 cal yr BP: Radiocarbon, v. 28, no. 2B, p. 980-1021.

Sun, D., and Miller, M. S., 2013, Study of the western edge of the African large low shear velocity province: Geochemistry, Geophysics, Geosystems, v. 14, no. 8, p. 3109-3125.

Suter, J. R., and Berryhill Jr, H. L., 1985, Late Quaternary shelf-margin deltas, northwest Gulf of Mexico: AAPG Bulletin, v. 69, no. 1, p. 77-91.

Sømme, T. O., Helland-Hansen, W., and Granjeon, D., 2009, Impact of eustatic amplitude variations on shelf morphology, sediment dispersal, and sequence stratigraphic interpretation: Icehouse versus greenhouse systems: Geology, v. 37, no. 7, p. 587-590.

Tinker, J., de Wit, M., and Brown, R., 2008, Mesozoic exhumation of the southern Cape, South Africa, quantified using apatite fission track thermochronology: Tectonophysics, v. 455, no. 1-4, p. 77-93.

Törnqvist, T. E., Wallinga, J., Murray, A. S., De Wolf, H., Cleveringa, P., and De Gans, W., 2000, Response of the Rhine–Meuse system (west-central Netherlands) to the last Quaternary glacio-eustatic cycles: a first assessment: Global and Planetary Change, v. 27, no. 1-4, p. 89-111.

Törnqvist, T. E., Wortman, S. R., Mateo, Z. R. P., Milne, G. A., and Swenson, J. B., 2006, Did the last sea level lowstand always lead to cross-shelf valley formation and source-to-sink sediment flux?: Journal of Geophysical Research: Earth Surface, v. 111, no. F4.

Wallinga, J., Törnqvist, T. E., Busschers, F. S., and Weerts, H. J., 2004, Allogenic forcing of the late Quaternary Rhine–Meuse fluvial record: the interplay of sea-level change, climate change and crustal movements: Basin Research, v. 16, no. 4, p. 535-547.

Walsh, J. P., Wiberg, P. L., Aalto, R., Nittrouer, C. A., and Kuehl, S. A., 2016, Source-to-sink research: economy of the Earth's surface and its strata, Elsevier.

Wenau, S., Preu, B., and Spiess, V., 2020, Geological development of the Limpopo Shelf (southern Mozambique) during the last sealevel cycle: Geo-Marine Letters, v. 40, no. 3, p. 363-377.

Wildman, M., Brown, R., Beucher, R., Persano, C., Stuart, F., Gallagher, K., Schwanethal, J., and Carter, A., 2016, The chronology and tectonic style of landscape evolution along the elevated Atlantic continental margin of South Africa resolved by joint apatite fission track and (U-Th-Sm)/He thermochronology: Tectonics, v. 35, no. 3, p. 511-545.

Wildman, M., Brown, R., Persano, C., Beucher, R., Stuart, F. M., Mackintosh, V., Gallagher, K., Schwanethal, J., and Carter, A., 2017, Contrasting Mesozoic evolution across the boundary between on and off craton regions of the South African plateau inferred from apatite fission track and (U-Th-Sm)/He thermochronology: Journal of Geophysical Research: Solid Earth, v. 122, no. 2, p. 1517-1547.

Zaitlin, B. A., Dalrymple, R. W., and Boyd, R., 1994, The stratigraphic organization of incised-valley systems associated with relative sea-level change.

CHAPTER 3: Field testing autogenic storage thresholds for environmental signals in the strata of the Mississippi delta

Abstract

Sediments transported from source terrains to depositional sinks carry environmental signals, which may or may not be preserved in stratigraphy. Recently developed theory suggests storage thresholds for environmental signals are set by the internal dynamics of sediment transport systems. For the first time, we explore this theory by testing whether changes in relative sea level (RSL) of various scales produce signals stored in field scale stratigraphy. This field test builds on results from physical experiments where identifiable stratigraphic signals of RSL change were only produced from RSL cycles with magnitudes and/or periodicities greater than the spatial and temporal scales of the deltaic autogenic dynamics. Published long term sedimentation rates and sea level reconstructions suggest that the Mississippi River Delta (MRD) should be a good place to study sea level signal storage thresholds. We use publicly available seismic volumes from NAMSS-USGS and well-logs from the MRD to study how and if signals of paleo-sea level change are stored in strata of the MRD, comparing strata of the late Miocene (LM) and Early Quaternary (EQ). Comparison of the amplitude and period of cycles in these two time periods, constrained by micropaleontological data, suggest storage of RSL signals in EQ strata, but not in the LM strata. We focus on statistics of paleo-channels and

valleys interpreted in the 3-D seismic volumes and well logs and the dimensionless numbers for depth- and time-scales critical for estimating the storage potential of RSL cycles are calculated from these channel-body dimensions. We show here that larger amplitude Early Quaternary RSL signals are preserved in the MRD, but smaller amplitude Late Miocene signals are not preserved, which is in tune with the signal shredding theory. Differences in cycle period and amplitude of RSL change in the two time periods could also influence other stratigraphic characteristics like grain-size and sediment partitioning between the shelf and the deeper marine. At a time when we are starting to quantify the capacity of strata to store information about past climate change, this study adds field scale observations that quantify the intermingling of stratigraphic products of autogenic dynamics with products of RSL change over geological timescales.

Introduction

Relative sea level (RSL) change can be connected to climate change and is used as a proxy to reconstruct past change in global temperature, melting of ice sheets, tectonics and paleogeography (Alley et al., 2005; Clark et al., 2004; Fairbanks, 1989; Haq, 1991; Haq et al., 1987). Signals of sea level change through Earth history are stored in strata and decoding these signals can help us interpret paleo climate change and prediction of future RSL change. Changes in RSL also drive changes in the dynamics of Earth's surface (e.g., channel migration rate) which get recorded in strata. A branch of stratigraphy termed sequence stratigraphy focuses on connecting depositional patterns and erosional surfaces preserved in marginal marine strata to allogenic controls like RSL change (Catuneanu et al., 2009b; Posamentier and Vail, 1988a; Van Wagoner et al., 1988). Many paleo-environmental interpretations that utilize sequence stratigraphic methods emphasize landscape responses to RSL change to explain stratigraphic structure (Bhattacharya, 2011; Blum et al., 2013; Catuneanu et al., 2009a; Van Wagoner, 1995). The tug of RSL change is generally thought to be one of the strongest allogenic forcings effecting Earth-surface dynamics, deposition rates, and stratigraphic architecture of continental margin systems. Falling RSL is connected to incision, formation of valleys, and a basinward shift of depositional facies. In contrast, rising RSL is thought to shift deposition landward, with eventual valley filling and preservation of paleovalleys in the strata (Posamentier and Vail, 1988b).

Environmental signals like base-level change affect storage of sediments and scales of geomorphic features depositional basins (sinks), which has been a focus of study for sequence stratigraphy. Signals of changing sea level are thought to be abundant in marginal marine strata and have been studied for years. However, some recent work questions the ability of some basins to record signals of changing RSL. For example, Li et al. (2016) and Yu et al. (2017), using physical experiments, explored the destruction of RSL signals by processes that are intrinsic to the sediment transport systems (autogenic processes). This is in contrast to many sequence-stratigraphic work flows that emphasize deterministic system responses to past SL change and the resultant stratal architecture. However, even some deterministic models suggest that reconstruction of RSL from strata can be difficult. As proposed by Allen (2008), deterministic modeling of processes in sediment transport systems can lead to buffering of signals due to surface processes that sometimes can be conceptualized as diffusive. Buffering or diffusion of signals describes the phenomenon of propagation signals (either upstream or downstream) that decay with distance from source or time since signal generation. Examples of environmental forcings that initiate diffusive signals include change in the upstream sediment supply or a downstream boundary elevation (Armitage et al., 2018; Paola, 2000). However, this approach tends to miss other variable responses due to the exclusion of stochastic processes (Straub et al., 2020). While processes that are extrinsic to the transport system (allogenic processes, like tectonics and sea level change) can influence depositional patterns, stochastic autogenic processes which cause storage and release of sediments are also important during RSL cycles and can influence stratigraphic architecture. This can mean that sediments get deposited even during the net erosional RSL fall phase, and vice versa during the depositional RSL rise phase (Blum and Price, 1998; Strong and Paola, 2008).

In recent years, the community has started to explore how or when we might be able to differentiate allogenic from autogenic controls on sediment transport systems and their preservation potential, and, whether autogenic processes can create stratigraphic features of the same scale as allogenic features (Best and Ashworth, 1997; Ganti et al., 2019). Some observational work (e.g. (Trower et al., 2018)) has been done as an application of the signal shredding theory at field scale. The theory that describes how signals are destructed due to sediment storage and release is called signal shredding and it is still a comparatively new area of research. Both buffering and signal shredding can result from the intermingling of allogenic and autogenic surface processes, which adds complexity to the stratigraphic record. These include the insertion of temporal gaps in the strata, and the incompleteness of the stratigraphic record (Paola et al., 2018; Sadler, 1981).

Certain environmental signals can be spread both temporally as well as spatially in a source to sink system due to autogenics. This is referred to as 'smearing of signals' over landscapes as well as the strata (Jerolmack and Paola, 2010). First, due to temporary storage in landforms like bed and bar forms, and due to flux of sediment out of channels to depositional environments like floodplains, signals can get smeared over space as they propagate downstream. This temporary storage in a range of depositional environments also results in a smearing of signals in time, as sediment liberated during a rapid climate event, by both large-scale processes such as lobe switching, as well as smaller scale processes like ripple migration, might reach the terminus of the transport system over a wide swath of time. If this smearing of signals across time and space is significant, it becomes impossible to piece together the clues that exist in the form of deposited sediment grains to tie it back to the original sudden increased pulse in sediment flux. Even with a complete coverage of the study area, these shredded signals are still not interpretable.

Some environmental signals travel from the source to sink terrains and are imprinted in strata through the depositional products of channelized transport systems. An example might be changes in sediment flux resulting from source terrain changes in tectonics or climate. However, not all signals travel along the full length of the transport system before getting deposited. A good example of this type of environmental signal is a change in sea level, as it is felt by the transport systems first at the shoreline, from where a signal can be generated that propagates both up and down system. While signals can propagate horizontally along the transport path, signals can also travel vertically into strata. In the case of sea level change, this vertical signal propagation into the stratigraphic record can occur with no or limited horizontal propagation. During the burial process, signals first pass through the active layer (layer still susceptible to reworking via autogenic processes) where they still might be degraded, and if this degradation is significant, the resultant stratigraphy may not preserve any evidence of the changing RSL. Only when these deposits, imprinted with signals with scales in excess of the stratigraphic products of autogenic processes, are ultimately buried deep enough to be preserved in the immobile layer, are they safe from destruction from autogenic processes. We follow the language of Straub et al. (2020) and differentiate a “transport shredder” from a “stratigraphic shredder”.

The stratigraphic shredder is associated with the vertical burial of the signal. This work will focus on the stratigraphic shredder as RSL signals are buried very close to where the signal is first felt by the transport system (i.e. the shoreline). Several numerical models and physical experiments have been conducted over the last decade to understand signal storage in stratigraphy and specifically about the sediment flux signal in the preserved stratigraphy and the related signal-to-noise problems (Ciarletta et al., 2019; Jerolmack and Paola, 2010; Romans et al., 2016; Toby et al., 2019; Tofelde et al., 2019; Trampush and Hajek, 2017; Van De Wiel and Coulthard, 2010).

Studying stratigraphic signal storage with seismic data from the Mississippi delta

When it comes to exploration of signal shredding theory at field scales, little has been done because of want of 3D data of decent areal coverage to characterize signals. Earlier studies suggested that since larger systems have larger autogenic scales, they should be more effective at shredding signals. To witness preservation of signals, smaller systems should be studied, but to test signal shredding a larger system like the MRD should be used. Signals of Early Quaternary (EQ) scale RSL cycles are of larger amplitude, compared to the late Miocene (LM) RSL cycles which are smaller in amplitude. Since we want to test the thresholds to store Milankovitch scale RSL signals in sedimentary strata, a system that is large enough to shred the smaller RSL signals is needed. Studies by Li et al. (2016) and Yu et al. (2017) that tested signal shredding theory using physical experiments, suggested that MRD should be able to shred these smaller RSL signals, which makes this a good place to study RSL signal storage thresholds. We use publicly available seismic cubes from National Archive of Marine Seismic Survey, under USGS (NAMSS-USGS). Using a 3D seismic cube, we have interpreted the dimensions of a large number of stratigraphic features resulting from channelized flow in the stratigraphy of the Early Quaternary and the Late Miocene. These two time periods have different amplitudes and periods for the RSL change signal. This is the first field scale study to test the signal shredding theory.

The past physical and numerical experiments used to test the theory have assumed that the major trunk system in a sedimentary basin sets the fidelity of the entire basin. But we want to understand how much effect the smaller coastal systems have on shredding signals in a basin, compared to the trunk system. We hypothesize that the EQ RSL signals will be preserved in all small and large systems, whereas the LM RSL signals are expected to be preserved in only smaller systems, but not in a larger system like the Mississippi River Basin.

Study Area

The northern Gulf of Mexico is a stable divergent continental margin (Galloway, 1989) and has been the major sink for sediments sourced from the continental United States for the past 65 million years (Galloway et al., 2011) (Fig 30). The Mississippi River is a major source -to-sink system, draining into the Gulf of Mexico and the MRD has been active for most of the last 65 Myrs, except for the Eocene epoch, even though the sediment routing and drainage patterns have changed over time (Blum and Pecha, 2014; Blum et al., 2017; Galloway et al., 2011; Xu et al., 2017). Numerous studies have been conducted to understand the evolution as well as the depositional history of the Mississippi River through time (Blum, 2019; Fisk and McFarlan Jr, 1955; Saucier, 1994). During the LM and EQ time-periods, the terminus of the Mississippi River was one of the principal depocenters in the Gulf of Mexico, along with depocenters linked to the Tennessee and Red Rivers (Bentley Sr et al., 2016; Blum et al., 2017; Galloway et al., 2011; Wu, 2004; Xu et al., 2017).

This area has been impacted by shifts in climate and sea level change over millennial and longer time scale during the post-glacial history (Buzas-Stephens et al., 2014). Changes in sediment flux from the hinterland due to change in climate, tectonics and geology present in the drainage basins of the rivers influence sedimentation pattern in this area (Anderson et al., 2016). MRD is highly influenced by the variable regional basin subsidence mainly driven by sediment compaction, glacial and sedimentary isostatic adjustment during the timescales we are interested in. The rates and drivers of subsidence are highly debated [for eg., (Anderson et al., 2016; Frederick et al., 2019; Simms et al., 2013; Wolstencroft et al., 2014)]. Other factors that have influenced the shelf sedimentation and physiography in this area are the differential fluvial flux (Olariu and Steel, 2009) and oceanographic currents and circulation systems (Anderson et al., 2004; Anderson et al., 2016). However, even though all of these factors play their part in signal storage, RSL signals are significant and are applied to the sediments right at the shoreline where our study area is.

The present fluvial axis of the Mississippi River has been in place since the Miocene. During the Miocene, the shelf-edge prograded by ~200 km and the nucleus for the fluvial-alluvial system that we see today, with the deepwater system in the Gulf of Mexico, was set up (Galloway et al., 2011; Winker, 1982). During the Miocene, the major source of sediment for the Mississippi system switched from the Rockies to the Appalachian Mountains and the influence of climate and tectonics for this switch has been a topic of much discussion in the literature [for e.g.,(Chapin, 2008; McMillan et al., 2006; Zachos et al., 2001)]. Along with this change in sediment supply, the uplift and rifting of Rio Grande played a major role in shifting the major sink for sediment from the NW Gulf of Mexico to the north-central Gulf of Mexico margin where they exist through the present. This coastal and deepwater sediment accumulation led to the formation of a composite delta system in the central Gulf of Mexico, with a slope apron and a channelized lobate fan complex (Bentley Sr et al., 2016; Combellas-Bigott and

Galloway, 2006; Galloway et al., 2000; Galloway et al., 2011; Winker, 1982; Wu, 2004). During this time, RSL cycles relevant for our study ranged from ~10-20 m with a cycle period of ~40 kyr (Lisiecki and Raymo, 2005; Miller et al., 2005; Raymo et al., 2006).

Throughout much of the early Quaternary, RSL cycles were dominated by a 43 kyr period. This transitioned to a dominant period of 100 kyrs in the Pleistocene (Imbrie and Imbrie, 1980; Lisiecki and Raymo, 2005; Miller et al., 2005; Raymo et al., 2006). In the Gulf of Mexico, this transition from 43 kyr cycle to 100 kyr cycle has been categorized by the presence of the foraminifera *Trimosina* A in wells, typically dated at ~0.6 Ma (Galloway et al., 2000). The EQ RSL cycles relevant for our study had a range of ~60-70 m and a period of ~40 kyr (Lisiecki and Raymo, 2005; Miller et al., 2005; Raymo et al., 2006). During this period, even though the exact location of the shoreline moved around in response to the fluctuations in RSL, the mean Quaternary shoreline rested around the present-day mid-shelf (Blum et al., 2009). During this time, the major tributaries of Mississippi, Missouri and Ohio rivers, were rerouted into the Gulf of Mexico due to the advancement of ice into North American interior, and the Platte, the Tennessee, and the Cumberland rivers were also part of the Mississippi drainage (Bentley Sr et al., 2016; Licciardi et al., 1998). At the shelf, the Mississippi was joined by the sediments from the Red river, the Tennessee-Ohio system and the Arkansas River.(Bentley Sr et al., 2016; Feeley et al., 1990; Galloway et al., 2011; Saucier, 1994; Weimer, 1991).

In a coastal to shallow marine environment like the MRD, the landscape is generally covered by a multitude of channels. There is a trunk channel and its distributaries contributing significant sediment to the basin. But there are also numerous smaller coastal channel systems that contribute to the reworking of sediment and ultimate filling of a depocenter. These smaller channel systems are crucial in understanding landscape dynamics, understanding ancient stratigraphic records, importantly floodplains, and coastal hydrology (Swartz et al., 2022). A number of small and large rivers have been flowing into the MRD during the time this basin has been active. Thus, some of the channel bodies residing in the strata of the Mississippi River Basin come from the ancestral Mississippi River, but others represent deposits of these smaller coastal systems.

Over long timescales, depositional patterns in the GoM are influenced by structural processes, including deep-seated subsidence caused by cooling of basin's basement and movement of gravity tectonic structures (i.e. mobile salt, namely Jurassic Louann salt). These gravity tectonic structures are manifested by extensive growth-faulting, salt bodies like welds, diapirs, and basin-floor compressional fold belts (Galloway, 2008). The salt and the structures created by its movement add to the overall complexity of the GoM. Salt mobilization during the Cenozoic has been a major player behind the creation of accommodation space and rapid subsidence in the shelf and upper slope (Galloway, 2008). The entire continental shelf and slope of northern Gulf of Mexico is influenced by these salt dynamics, which have produced many isolated salt-bodies enclosed by interconnected minibasins near the shelf edge, which has affected the thickness of strata from the Mesozoic through the Quaternary (Combellas-Bigott and Galloway, 2006; Diegel et al., 1995; Galloway et al., 2000; Peel et al., 1995; Peel, 2014; Winker, 1982). Fig 31 shows the presence of a salt dome in the study area and care has been taken to exclude manifestations of the salt structures and faults during seismic interpretation.

Theoretical background

Following theory outlined by Li et al. (2016) and Yu et al. (2017), amplitude and time-periods of RSL cycles are compared with autogenic time and space scales for deltaic stratigraphy. H^*, the dimensionless length scale and T^*, the dimensionless timescale (Li et al., 2016; Yu et al., 2017) are defined as –

$$H^* = \frac{R_{RSL}}{H_C}$$

Equation 1

$$T^* = \frac{T_{RSL}}{T_C}$$

Equation 2

where R_{RSL} is the range of a RSL cycle (i.e. difference in elevation of sea-level between peak and trough), H_C is the depth of the largest autogenic channels, which can be as large as $3H_{mean}$ (Ganti et al., 2014), T_{RSL} is the period of an RSL cycle and T_C is the compensational time-scale, which is the time for deposits of autogenic surface processes to average out such that an isopach reflects a subsidence pattern (Wang et al., 2011). The compensational time-scale can be estimated using the equation

$$T_C = \frac{l}{\bar{r}},$$

Equation 3

Where $\bar{r}$ is the long-term sedimentation rate, and l is the maximum autogenic vertical roughness scale in a region of study. It has been approximated by H_C in several experimental studies. However, Trampush et al. (2017) showed that this scale for some settings might be larger than H_c, due to the presence of features like delta foresets that might introduce even larger roughness into a system. Results from physical experiments suggest that deltas experiencing RSL cycles characterized by H^* and/or $T^* >>1$ preserve sea level signals in their strata, but in systems where both H^* and $T^* <<1$, signals of RSL cycles are either absent or of similar scale to products of autogenic processes, making them difficult to detect.

Li et al. (2016) and Yu et al. (2017) calculated the preservation potential of RSL signals for a database of field scale deltaic systems. This analysis suggested that the present-day Mississippi Delta is a good place to test signal-shredding theory as H^* and T^* values calculated for the EQ suggest RSL signals should be preserved, while LM signals should be susceptible to shredding. We suggest that the structure of the present-day Mississippi river channel is largely the result of autogenic processes at play during the Holocene and as such morphometric scales from the modern system can be used to estimate autogenic scales. During this time period the channel has not experienced major RSL change. An estimate of a vertical scale of roughness for the MSD and a reported rate of subsidence are needed to calculate the average H^* and T^* values for this marginal marine system. For this, we use the present-day depth of the deepest segments (H_c) of the Mississippi river (~70 m) (Nittrouer, 2013) as the autogenic depth of the system and the long-term sedimentation rate from an area near the margin of the MRD ($\bar{r}$ = 0.23 m/kyr). This long-term sediment rate is reported near the mouth of the current mouth of the Mississippi River (Straub et al. 2009).

For the EQ, the H^* and T^* values for MSD are 1 and 0.1respectively, whereas for LM stratigraphy, H^* is 0.2and T^* is 0.1. Based on these values, we hypothesize that the EQ RSL signals will be preserved in all small and large systems in this basin, whereas the LM RSL signals are expected to be preserved in only smaller systems, but not in a larger river system like the main trunk of the Mississippi River Basin. Even though this framework has been tested in physical experiments (Li et al., 2016; Yu et al., 2017), to date no one has field tested this theory.

Data and Methods

Micropaleontological data

To meaningfully analyze the seismic data from our study area, we need to first ascertain and assign ages to the different stratigraphic packages represented in the data, so that we can focus our analysis on the packages from the time periods of interest. We acknowledge the limited age data for our study area, which constrains our ability to assign high resolution ages to the stratigraphy we are working with. However, for this study, we don't aim to identify the strata of a specific relative sea level cycle, but rather the strata deposited during periods in which cycles had similar periods and magnitudes. Thus, we only need to know the general age/depth range that a particular section of the stratigraphy is in, to characterize the deposits by RSL cycles of a certain amplitude and period. Micropaleontological data of planktonic foraminifera available from a well in the study area were used to generate an age-depth model for our study region (Fig 31). The planktonic microfossils were recovered from well API#177094078100, with data made publicly available by United States Department of the Interior Bureau of Ocean Energy Management. Using the depth ranges and age ranges of the microfossils *Lenticulina* and *Bigenerina floridana,* the stratigraphic units were assigned relative dates (Fig 31), which facilitates estimation of sedimentation rates for the study area (Fig 32). We also know the age of the current Earth surface (0 ma), which gives us three data points for estimating sedimentation rate of 0.54 m/ka. Using this long-term sedimentation rate for the study area, rather

than the rate presented for the terminus of the modern channel by Straub et al. (2009) for calculating the compensation timescale and the present-day depth of the deepest segments (H_C) of the Mississippi river (~70 m) (Nittrouer, 2013) as the autogenic depth of the system, we refined our estimation for the H^* and T^* values for MSD. For the EQ, the H^* and T^* values are 1 and 0.8 respectively, whereas for LM stratigraphy, H^* is 0.1 and T^* is 0.3.
This sedimentation rate and a typical seismic velocity for shallow stratigraphy was also used to characterize the EQ and LM stratigraphy. EQ was characterized as a unit above the presence of *Lenticulina*, more specifically a stratigraphic package which is about 0.5-1 km in depth, corresponding to an age range of approximately 1-0.8 Ma, whereas LM is characterized as the stratigraphic unit below the presence of *Bigenerina floridana* (BOEMRE, (Akers, 1955)). The LM sedimentary package in the study area corresponds to approximately 6-6.3 Ma and is at approximately 3.5-4 km in depth.

Seismic dataset

We focus on creating distributions to describe widths and depths of geobodies crafted by channelized processes in our two time periods of interest. A statistical comparison between the channel body widths and depths can help in quantifying if and how sea level cycles influenced MRD strata. We do this by mapping features in an industry grade seismic data set.

A publicly- available 3D seismic cube of ~980 sq km is used to study the strata from the EQ and LM time periods. (Fig. 30). This seismic volume covers a swath of the current continental shelf, just west of the Mississippi Canyon, which puts it near the center of the long-term MRD basin (Fig. 30), where it received sediments through the LM and EQ time-periods (Galloway, 2008; Galloway et al., 2000; Galloway et al., 2011). It was collected in 1993 for oil and gas exploration purposes. Following federal regulations, this data was submitted to the Bureau of Ocean Energy Management. After 25 years, the seismic cube was released to the public by the National Archive of Marine Seismic Survey, under USGS. The inline and crossline spacings are 25 m and the sample interval is 4 milliseconds. The frequency content of the seismic volume averages ~35 Hz with a fallout on the high frequency end at ~65 Hz. Assuming a typical seismic velocity for the depth range analyzed of 1700-2000 m/s we estimate a theoretical vertical resolution set by a quarter wavelength of between 7-14 m.

Seismic waves reflect and refract along geophysical boundaries, many of which are associated with lithologic boundaries in the subsurface. Using this principle, the seismic cube was utilized to interpret channel bodies (CB) of different dimensions from the EQ and LM. For this study, we define channel bodies as any geobody constructed from channelized processes. With this purpose, this term encompasses channels, channel belts, and paleo-valleys. These CBs were interpreted from both horizontal and vertical seismic sections. Interpretation and mapping of the smaller channel features is easier in approximately horizontal time slices compared to vertical sections due to data resolution and typical aspect ratio of channel bodies (width>depth). Channel margins are interpreted on horizontal (time) sections using a variance attribute that accentuates edges or discontinuities in the seismic data (Fig. 33,34). Windows of ~100 milliseconds, which corresponds to about 300 thousand years of age and close to 100m in thickness, are identified for both the EQ and LM time-periods, corresponding to the depths these stratigraphic sections are present in the seismic section. This thickness is roughly equivalent to the compensation scale of the basin (i.e. approximately equal to the upper range of the modern Mississippi River depth). Each of these windows of interest is then divided into ~12 time-slices with a sampling interval of ~8 milliseconds. For every time slice, discontinuities that resemble channel body margins, were mapped. CB margins can be described as two linear features which run approximately parallel to each other, and their sinuosity characteristics are like those of modern-day channels and channel belts. In cross-section, the channel bodies can be interpreted as inclined flanks which truncate underlying seismic horizons. This mapping process produced a database that consists of 821 channel bodies, 431 from EQ and 390 from LM time periods.

Calculation of channel body dimensions

The dimensions of channel bodies can hold valuable clues about their origins, which would suggest whether they are products of sea level cycles. Thus, distributions of their dimensions can aid evaluation of the preservation of sea level signals in strata. Past their link to sea level cycles, the channel body dimensions can also inform us on the presence of autogenic vs allogenic signals. For example, even if channel body features do not resemble paleovalleys, we can compare typical CB dimensions from EQ and the LM with present day channel scales to see if they are all similar, i.e., they show forms which are like the modern autogenic configuration of the channel body, which would suggest a shredding of sea level signals. If they are different from the present-day scales, then preserved channel bodies possibly hold allogenic signals. Using the CB margins interpreted from the seismic data, channel-body widths calculated from the interpreted paired CB margins using a Python based script designed by Sylvester and reported on in Sylvester et al. (2021)(pers. communication, Zoltan Sylvester). The detailed script and explanation for the width calculation is available at https://github.com/zsylvester/channelmapper.

In a coastal environment, the different channelized transport systems present can be binned into four different types- alluvial valley fills, delta distributaries, meandering channels and braided channels. We are following a framework set up by Gibling (2006) to create bins for the different types of CB. The calculated CB widths were compared with the typical widths of these types of channels (Table 2) and then binned into the four types accordingly. Our aim is to ascertain the presence of paleovalleys in the sedimentary packages from the two time periods of interest, which is indicative of the storage of sea level signals. Fluvial-channel bodies have been characterized by their width:depth ratio in the literature [for e.g., (Gibling et al., 2011; Krynine, 1948; Pettijohn et al., 1972)] and we did the same, using typical channel-body widths presented in the extensive database collated by Gibling (2006). The interpreted CBs were binned into the different types of channelized transport systems to differentiate between paleovalleys and other channel bodies.

We also estimate thicknesses of channel bodies, specifically maximum thicknesses, to calculate H^* and T^* values. CBs with depths below the vertical resolution of the seismic volume cannot be interpreted in the vertical seismic slices. For each CB that could not be imaged in the vertical, we used the database from Gibling (2006) to calculate a theoretical maximum CB depths. The database reports the typical width:depth ratio for all the common types of fluvial systems. Depending on the type of CB, the width of the same was combined with the associated width:depth ratios to arrive at the theoretical maximum depth that the particular CB could have. (Table 2)

A portion of channel bodies can be interpreted both on the vertical and horizontal seismic slices. For these CBs the calculation of width and allocating

Table 4 The dimensions and their ratio used in the analysis to interpret types of channel bodies and calculate the channel depths, following Gibling (2006)

Types of channel	Common range for width (km)	Maximum Width to Depth ratio
Delta Distributaries	0.01-0.3	1:5
Meandering	0.3-3	1:30
Braided/Low-Sinuosity rivers	0.5-10	1:50
Valleys fills within alluvial and marine strata	0.2-25	1:10

them to different channel types was done with the methods described above. However, their thickness is calculated from the seismic data itself. To calculate H^* and T^*, we need the approximate depth of the deepest channels in the stratigraphy. For vertically resolvable CBs, we calculate the approximate maximum thickness between interpreted scours, which can be interpreted as the base of a channel body incised by the sediment transport system, and an approximate top envelope, constructed by mapping the seismic reflector just above the scour which was not incised by the channel body. This is the approximate thickness of the channel body, which can be then used in further analysis.

Once CB dimensions were collected, the H^* and T^* for all the CBs are calculated using the equations described in the theoretical background section. There is an important distinction between the earlier works done by Li et al. (2016) and Yu et al. (2017) and this work. In earlier calculations for H^* and T^*, the regional preservation potential for an environmental signal was calculated for an entire depositional basin, using the compensational timescale and depth of the deepest channels in the basin. The experimental setup of these earlier studies utilized a single feed point from which all channels emanated. Thus, all channels were distributaries of the trunk system. In comparison, some of the CBs we image can be linked to the paleo-MR, while others are products of coastal catchments. So, to explore if clear signals of SL change are stored in the MRD strata (which includes products of the trunk system and smaller coastal systems) we generate distributions of H^* and T^* using all CBs measurements.

Well log data

Well log data from the six wells (API # 177094112900, 177094040000, 177094078100, 177094146700, 177090014800, 177094140900) in the study area were also used to study the ratio of sand to shale (or net:gross) preserved in the study region during the two time periods. These publicly available well data from the Bureau of Safety and Environmental Enforcement report gamma ray (GR) and spontaneous potential (SP logs) with depth. Only one well in the area covers the EQ section, while the LM section is covered by all six wells. We focus on the gamma ray (GR) logs to estimate sand:shale proportions.

GR measurements come from wireline logging of wells and measures the naturally occurring radioactivity in the rock or sediment. Compared to sand, clay minerals, which make up a significant fraction of shale layers, generally have a higher concentration of radioactive elements. Thus, shale-free sand generally has a lower GR reading, while shale-rich strata have higher GR values.

A cut-off GR value is assigned to demarcate the sand and the shale sections. Since the well logs come from different logging companies and times of running the wireline logging equipment, the instruments were corrected against different standards and the initial data processing also had different standards applied to them. Due to this, different cut-offs were used for the different wells. To decide on a cut-off value, visual inspection of the logs (Fig 50, 52) was done, followed by plotting the GR data as bar diagrams to see their distributions (Fig 45). Depending on the GR value against a specific depth, if the GR was above the cut-off, it was assigned to be shale, and if not, it was assigned sand. The proportions of sand and shale are then calculated in both EQ and LM sections (Fig 50,52).

Present-day Mississippi channel width

As discussed in Section 3, the present-day Mississippi river channel can be regarded as an example of a predominantly autogenic channel (Bentley Sr et al., 2016). Thus, the dimensions from this channel were compared to the EQ and LM CB dimensions. We use data defining the depth and width of the lower 800 kms of the present-day Mississippi channel, as measured from Head of Passes reported in Nittrouer et al. (2012) to compare the CB dimensions. The U.S. Army Corps of engineers (USACE; data collected 1974–1975; found in Harmar, 2004, appendix) collected these channel survey data on average every 312 m, covering the channel between the normal-flow stretch through the backwater reach. The 40th percentile elevation, from the channel bed, for every transect was used to determine the channel-bed elevation (Nittrouer et al., 2012), which is used as the depth data for a modern-day autogenic channel. The width data comes from the transect profiles. All the elevation data are expressed in meters above mean sea level, and was converted from the data referenced to NGD 1929.

Results

Channel body dimensions

Classification of CBs based on the definitions of Gibling (2006) suggest that CBs interpreted in both EQ and LM are either delta distributaries (~40%) or meandering channels (~50%), with only a small section of these being braided channels (~10%) (Fig 39A). Even though this method creates very sharp boundaries between the different types of CBs, we want to emphasize the fact that in reality, these boundaries are gradational. The difference in the types of CBs between the two time periods only emerge in the tail of the distribution which characterizes the very largest CBs. The cumulative distributive functions

(CDF) of the widths of CBs from the EQ and LM are similar, spreading over scales of 10^1-10^3 m. However, the distribution from the EQ contains several datapoints, which are close to 10^4 m wide (Fig 39A). The significantly wider CBs interpreted in the EQ are interpreted to be paleovalley-fills, which are completely absent in the distribution of the LM CBs. The EQ CBs are not only considerably wider in comparison to the LM CBs, but they are also significantly deeper (Fig 39B). The thickness of the CBs from both EQ and LM are between 10^1-10^2 m, except for the same few CBs from EQ which are between 10^2-10^3 m thick.

The width-to-depth ratio was calculated for the CBs and a comparison was made of the EQ and LM (Fig 41). Almost all the CBs from EQ have a width to depth ratio between 1 to 60, with only two being higher than 100, whereas in case of LM, all but one CBs have a width to depth ratio between 1 and 40, with one being closer to 100. However, when we looked at the width to depth ratios of the CBs in conjunction to their thickness, we note that some of the deepest EQ CBs (depth>100s of m) show low width to depth value (<5), which can be taken as evidence for presence of paleovalleys in the stratigraphy. Width to depth ratios of paleovalleys, in marine and alluvial strata, is highly variable between 1 to 1000, with considerably higher depth than the rest of the CBs in a system (Gibling, 2006). Conversely, for the LM CBs, the deeper channels also have larger width to depth ratios, as expected for a system perturbed mostly by autogenics.

The H^* and T^* values of the CBs from the two different time periods are plotted in a H^*-T^* space in Fig 47. This H^*-T^* space can be divided into four quadrants, based on the values of both the time and depth scales of RSL signal preservation. <5% of the EQ CBs have both H^* and T^* <1, plotting in the signal shredding regime and the rest of the CBs have both H^* and T^* greater than 1, thus CBs from this time is overwhelmingly expected to preserve the RSL signal. The EQ CBs with the lowest H^* and T^* values are paleovalleys. On the other hand, ~40 % of the LM CBs plot in the shredding regime, with only one LM CB having H^*>1 and 60% of them T^*>1. Close to half of the total population of interpreted LM CBs are expected to shred the RSL signal.

Present-day Mississippi channel width

The present-day Mississippi river channel dimensions are compared with those from both the LM and EQ and the CDF of the width (Fig 39A) and thickness (Fig 39B) of the channel bodies from the LM and the present-day Mississippi are plotted. The CDF of the channel width of the Mississippi spreads over a higher range of values, compared to the LM and EQ CBs. The CBs are a collection of different sediment transport systems from tidal channels to paleovalleys, with only a few of them being comparable with a Mississippi-scale system. So, comparing the whole distribution of the width and thickness data is not prudent here. The important observation here is that the deeper and wider channel-bodies present in the EQ make the tails of the distributions heavier compared to that of the modern river or the ones from LM. The dimensions of the present-day autogenic Mississippi river are smaller than the dimensions of the interpreted paleovalleys seen in the coarser tail of the EQ CBs, the width and the thickness of these features being close to a factor larger than anything seen in the LM distribution and the present-day Mississippi River. Thus, the dimensions of the present-day autogenic Mississippi river are closer to the distribution of CB dimensions from the LM, providing more evidence that the LM stratigraphy stored the autogenic signal, shredding the allogenic RSL signal.

Well log data

A major line of evidence that can be used to understand the preservation of signals of RSL forcing in depositional basins is the proportion of sand and shale. In traditional sequence stratigraphic models, the change in RSL cycle is assumed to be the largest contributor to the deposition of sediments in the deeper parts of the ocean (Catuneanu et al., 2009b; Posamentier and Vail, 1988a) and a higher sand/mud ratio signifies the lowest rates of RSL fall to a minimum value of RSL in a RSL cycle (Catuneanu et al., 2009b). During a single RSL cycle, alternation between high and low sand amounts should be seen at a given point, depending on the size of the RSL amplitude as well as the position on the RSL cycle. During highstand (and higher amplitude cycles), the sand/mud ratio should be lower in the deeper marine and vice versa for lowstand (and lower amplitude cycles). Kim et al. (2009) have also shown that repeated eustatic cycling can cause increased sediment delivery to offshore, and the effect is proportional to the amplitude of the RSL cycle. However, there have also been a number of studies that show that there is no direct correlation between deep water sand deposition during lowstand (Burgess et al., 2008; Harris et al., 2018; Harris et al., 2016; Kim et al., 2013).

To analyze sand/mud ratio from a study area, the coverage of well data is essential, since data collected from a well is specific to a single point in the study area. Care must be taken when such data is utilized to reach regional conclusions. Only one well in the area covers the EQ section, while the LM section is covered by six wells. From a single data point in the area, it is not prudent to comment on the 3D distribution of proportion of sediments or their properties. However, some broad observations can be reported from the sand shale proportions, calculated from the GR logs, of these wells as well as by analyzing the pattern of the GR logs.

During the LM, four out of six wells show a higher shale to sand ratio, with ~30% sand present in the subsurface. The remaining two have higher sand percentages (~55%) and both are located in the north-eastern part of the study area. The one well (API #177094078100) that was logged for EQ strata has 35% sand present in it, which is very similar to the average sand percentage in the study area during LM. During LM, this well had ~24% sand, and there was an increase of ~10% sand in this location from LM to EQ (Fig 48).

Analyzing GR log patterns, we can find important paleoenvironmental clues as well. The EQ strata mostly has multiple thin strips of intercalated sand in shale, some of which might be thin tidal channels. Some bell-shaped sandy features can be seen which could signify retrogradation and the presence of fluvial point bars, tidal bars and flats and tidal channels. The very base of this strata in an aggrading blocky sequence, which was probably an amalgamated channel (Fig 50). During the LM, in the same location, we see that the strata had even thinner intercalations of sand and a couple of bell-shaped retrograding bar deposits. Overall analysis of the LM well-logs shows an abundance of sawtooth GR patterns, which can be interpreted to be fluvial floodplains, with a number of bell-shaped retrograding point bars and tidal channel fills and some amalgamated channels. For example, the well with API #177090014800 has a very thick blocky amalgamated channel. The wells with the ~55% sand fraction (API #177094140900 and #177094112900) show evidence of fluvial floodplains, point bars, tidal channel fills and amalgamated channel fills too (Fig 52).

Discussion

The measured (and estimated) dimensions of channel bodies in our study region from the two time periods that we explore, EQ and LM, show differences in CB dimensions that are likely due to differences in allogenic forcings and the basin's signal preservation potential. We defined a stratigraphic signal of RSL change as being an attribute of strata that could be differentiated from the products of autogenic surface dynamics that might occur in a basin unaffected by environmental change. For the MRD basin, we note that a wide distribution of

CB dimensions occurs for both the EQ and LM time periods. These CB's are the products of sediment transport through the paleo-Mississippi River, in addition to many other paleo-coastal rivers.

We use our measurements and estimates of CB thickness and long-term deposition rates to place each CB on the H^*-T^* plot. First, we note that this process produces a distribution of H^*-T^* values for each time period. These distributions span high H^*-T^* values associated with the smaller coastal channels to smaller values tied to CB's with scales similar to the modern day Mississippi River. A key observation is that approximately half of the Miocene CBs plot in the shredding regime, compared to only ~5% of the CBs from the early Quaternary (fig). Practically, this means that the range and period of RSL cycles in the LM were less than the resulting CB thicknesses and the times to generate basin wide deposits of equivalent thicknesses as the CBs for half of the mapped geobodies. However, this result alone does not fully support the shredding of RSL signals in the LM as 1) half of the CB's in the LM do fall within the signal preservation regime and 2) CBs that fall within the shredding regime could have scales influenced by RSL change, just with the influence being less than the total RSL change. We note, though, that all of the mapped CB's in the LM, also have scales that are equal to or less than the scales of the modern day Mississippi channel, which we consider to be an autogenic representation of the system. Taken together, these observations support shredding of signals of RSL change in the LM strata.

In contrast, 95% of the EQ CB's fall within the signal preservation regime of the H^*-T^* plot. This suggests a much higher likelihood that strata of the EQ contain definitive signals of RSL change. Further, of the 5% of EQ CBs that do fall within the shredding regime most have scales in excess of those found on the modern (autogenic) configuration of the Mississippi River and some have width:depth ratios that suggest they formed during the filling of paleo-valleys carved in response to changing RSL. These observations support signal preservation of changing RSL in EQ strata. This is in line with our predictions based on signal shredding theory.

Combined, observations from the LM and EQ support stratigraphic signal shredding theory. These two time periods were predicted to fall on either side of the signal shredding threshold with definitive signals preserved in the EQ, but not in the LM. This highlights how not all RSL change produces measurable signals in the 'recorded history' preserved in the stratigraphic archive. Next, we explore how our H^*-T^* regime can aid prediction of not only the presence, but an expected type of RSL signal in strata.

In this study, we explore sea level change signals which are produced and stored in marginal marine basins. This contrasts with other signals of environmental change, for example sediment supply signals that are produced by changing tectonics or climate in hinterlands, that are produced far from where the stratigraphic signal might be recorded. As such, the primary culprit for shredding the RSL signals we explore is the stratigraphic shredder proposed by

Straub et al. (2020), in contrast to shredding of environmental signals by sediment transport proposed by Jerolmack and Paola (2010). Stratigraphic signal shredding results when the signals of environmental change are of similar or smaller scales as the stratigraphic products of autogenic processes, thus making it difficult to differentiate environmental signal from autogenic noise. In the Mississippi River Basin, the estimated compensation timescale is approximately 140 ka (using a channel depth of 70 m and a subsidence rate of 0.54 m/ka). The dominant Milankovitch timescales of RSL change (100 ky or 40 ky) are thus short in comparison to the basin's maximum autogenic timescale, which would make signal identification beyond background noise difficult in both time periods. However, the amplitudes of the EQ RSL cycles are larger than most EQ CBs, suggesting susceptibility to changing surface dynamics and altered stratigraphic products due to the RSL change. For the LM, the scale of RSL change was also in excess of the thicknesses of about half of the mapped CBs, specifically the smaller mapped CBs. However, the larger mapped CBs from the LM had thicknesses in excess of the RSL cycle range from that time period. Thus, the larger CB's could not be differentiated from the autogenic scales and since there is an autogenic distribution of channel depths on the surface at any time period, which produce a distribution of CB thicknesses, it is difficult to equivocally identify the environmental signal in the smaller channels.

The H^*-T^* framework gives us a tool to quantitatively compare the scales of allogenic environmental forcings with the scales of local autogenic signals.

Here we highlight expected signal attributes for RSL signals that fall in different quadrants of the H^*-T^* space. H^* is a measure of the maximum autogenic depth of the individual channel bodies, compared to the amplitude of the allogenic SL change during that particular time period. In the same way, T^* is a measure of the length of time necessary for a transport system to bury sediment to a depth that it is no longer susceptible to autogenic reworking by autogenic channelized processes, compared to the period of allogenic SL change. H^* and T^* are inversely proportional to autogenic channel depths. A channel that plots in the quadrant defined by both H^* and $T^*>1$ should produce channelized bodies that are both deeper and wider than their autogenic representation. In addition, this should result in more deposition in the distal part of the basin, compared to the proximal settings. In the case of $H^*>1$ and $T^*<1$, we suggest the dominant signal will be an increase in CB thickness relative to autogenic products. For $T^*>1$ and $H^*<1$, we suggest one would see wider CBs and more distal sediment deposition. In the case of H^* and T^* both being less than 1, the RSL signal will be susceptible to shredding. This will only happen when an RSL change signal is imposed on a CB, without any autogenic influence. Here we note that the predicted changes in deposition from proximal to distal parts of the system cannot be conclusively tested in this work, due to the limited geographical region explored, and the limited well-log data from the EQ time-period, which could aid identification of grain size signals in the strata. Future work can be focused on this issue.

Here we highlight the form of the geobodies from the EQ that we suggest carry the signals of RSL change in the EQ strata. In fig. 47, the interpreted paleovalleys from the EQ stratigraphy plot in the signal shredding domain. These paleovalleys have low width to depth ratios, compared with bodies resulting from single channel activity or meander belts, signifying their allogenic origin (fig 41). These geobodies were likely constructed by channels of significant size that were tugged by the RSL change. Channels on the upper end of the autogenic size range that responded to large RSL change create the most easily identifiable signal of paleo RSL-change in our study. This contrasts with other smaller-scale channels that were already been well within the autogenic band, that when tugged by RSL change deepened and widened, but not out of the autogenic bands.

Uncertainties in this study and the implementation of stratigraphic shredding theory

To document and analyze the preservation of RSL signals in stratigraphy, it is useful to estimate paleo-channel dimensions from stratigraphic observables. There are a number of ways to estimate paleo-channel depths from preserved channel fills, but there can be substantial error associated with these methods [for e.g., (Alexander et al., 2020; Mohrig et al., 2000)]. Some of this error is associated with our ability to differentiate stratigraphic products linked to autogenic channel processes from products of allogenic forcing. For example, recent work shows that autogenic processes like avulsions can create backwater and flood scours whose dimensions can be comparable to incised paleovalleys formed in response to changing RSL [for e.g., (Ganti et al., 2019; Trower et al., 2018). The paleovalleys reported in this study are not as large as we expected them. The width to depth ratio as well as the width of the CBs identified as paleovalleys are in the lower end of the range of dimensions suggested by Gibling (2006), which can also be comparable to the modern-day channel belt dimensions. The absence of larger paleovalleys can be restricted by the size of the seismic volume, which would obstruct us from mapping larger CBs.

Conclusion

This work demonstrates how to apply signal shredding theory to field scale settings. Even though a number of numerical and physical experiments have explored signal shredding of RSL change, changing sediment or fluid flux (Jerolmack and Paola, 2010; Li et al., 2016; von der Heydt et al., 2003; Yu et al., 2017), this is the first test of this idea at field scale. While we cannot definitively state that signals of RSL change are present or not in either of the two time periods explored, broadly speaking the results support the stratigraphic signal shredding framework for RSL cycles. This supports the premise that in some sedimentary basins, some RSL cycles are of insufficient duration or magnitude to produce stratigraphic products outside the range of the products of autogenic channel dynamics. This adds to the growing body of literature that explores non-uniqueness of stratigraphic properties, formed by allogenic and/or autogenic processes (Burgess and Prince (2015). It highlights the need for multiple hypotheses and scenario development that should be considered when interpreting stratal architecture, scales, and geometries for interpretation of global RSL changes.

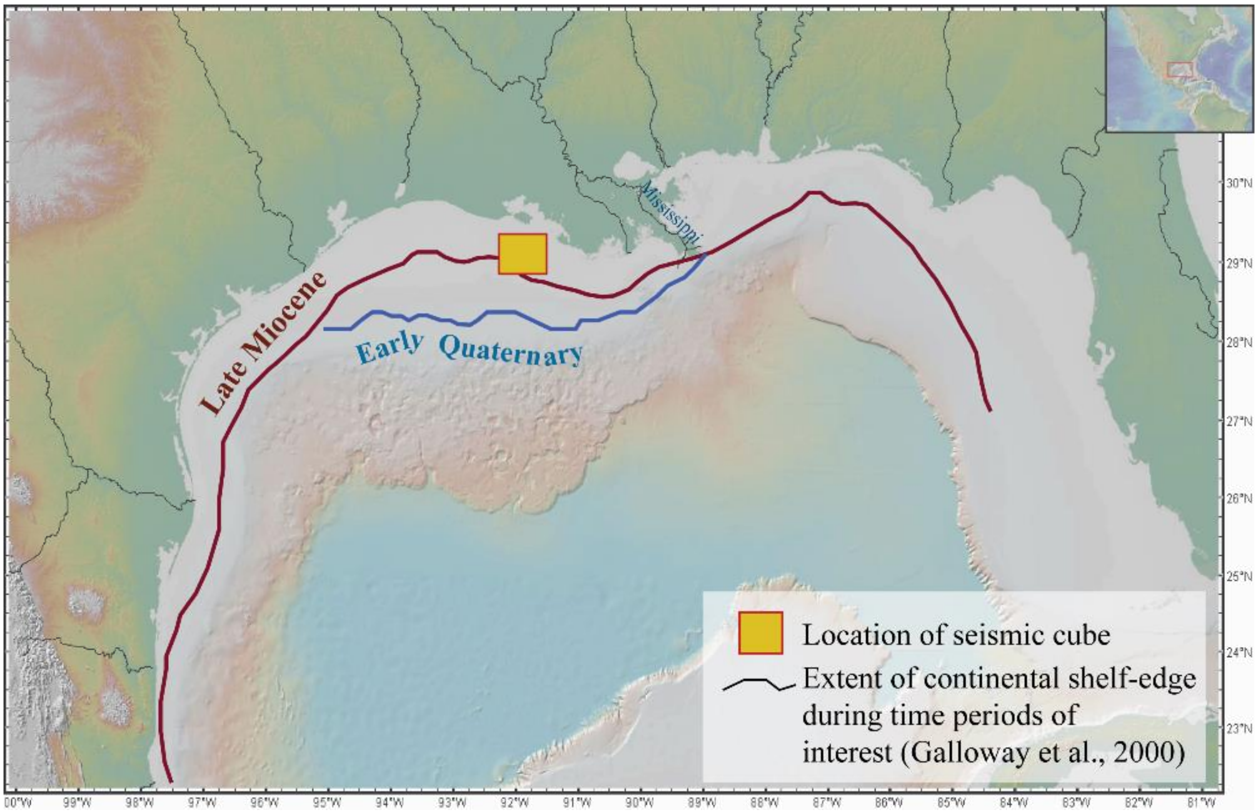

Figure 30 Map of the study area. The blue line is the extent of the continental shelf edge during the Early Quaternary and red signifies the one for Late Miocene. The study area was beyond the shelf edge during both times

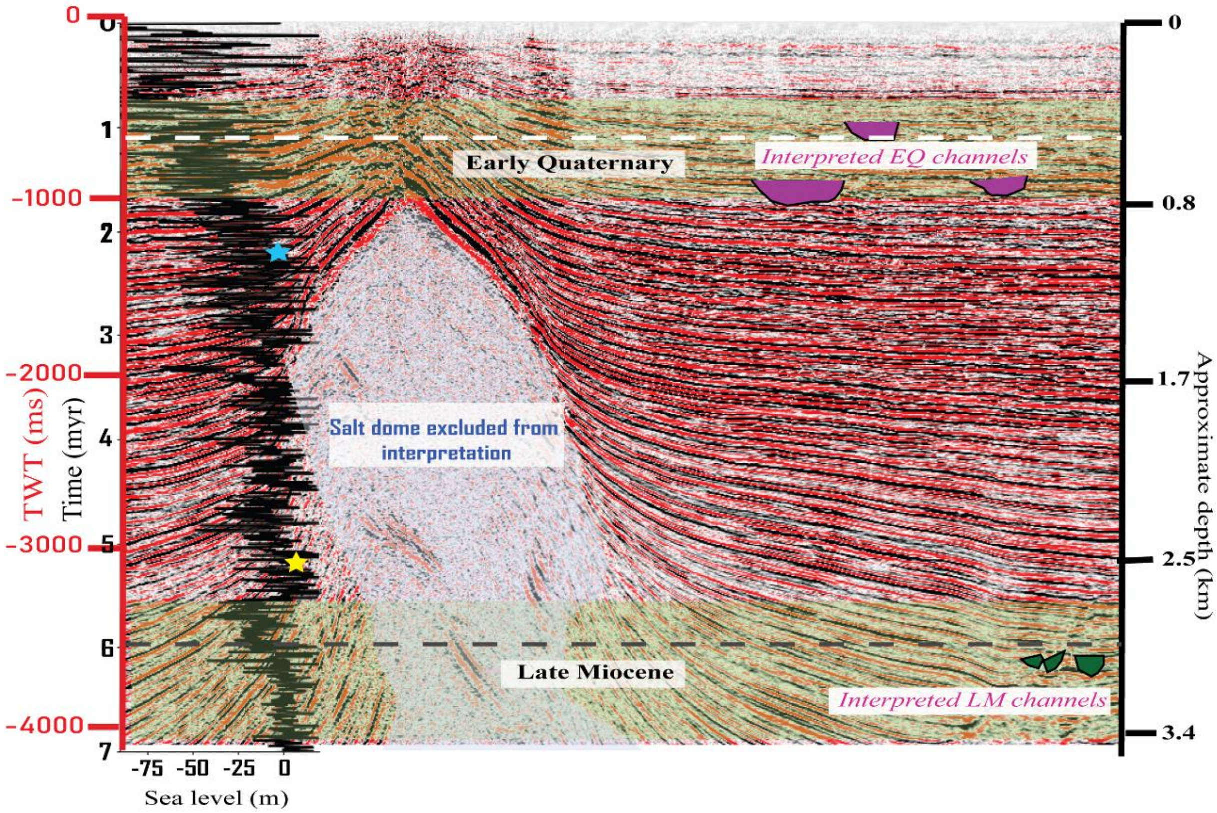

Figure 31 A dip section showing the two-way travel time and depth relationship with respect to the relative sea level history adapted from Miller et al. (2005). The blue star shows the presence of an Early Quaternary microfossil which is used to constrain our time-period of interest, right above shown by a colored box labeled Early Quaternary. The Late Miocene stratigraphy has been constrained from foraminifera samples, shown by a yellow star, which constrains the age of our time period of interest right below, shown by the colored box labeled Late Miocene. Examples of channel bodies interpreted in the vertical sections for both EQ and LM are shown. The white line shows the approximate location of the time slice shown in fig 3 as an example of EQ stratigraphy and the black line is the same shown in fig 4 for Late Miocene.

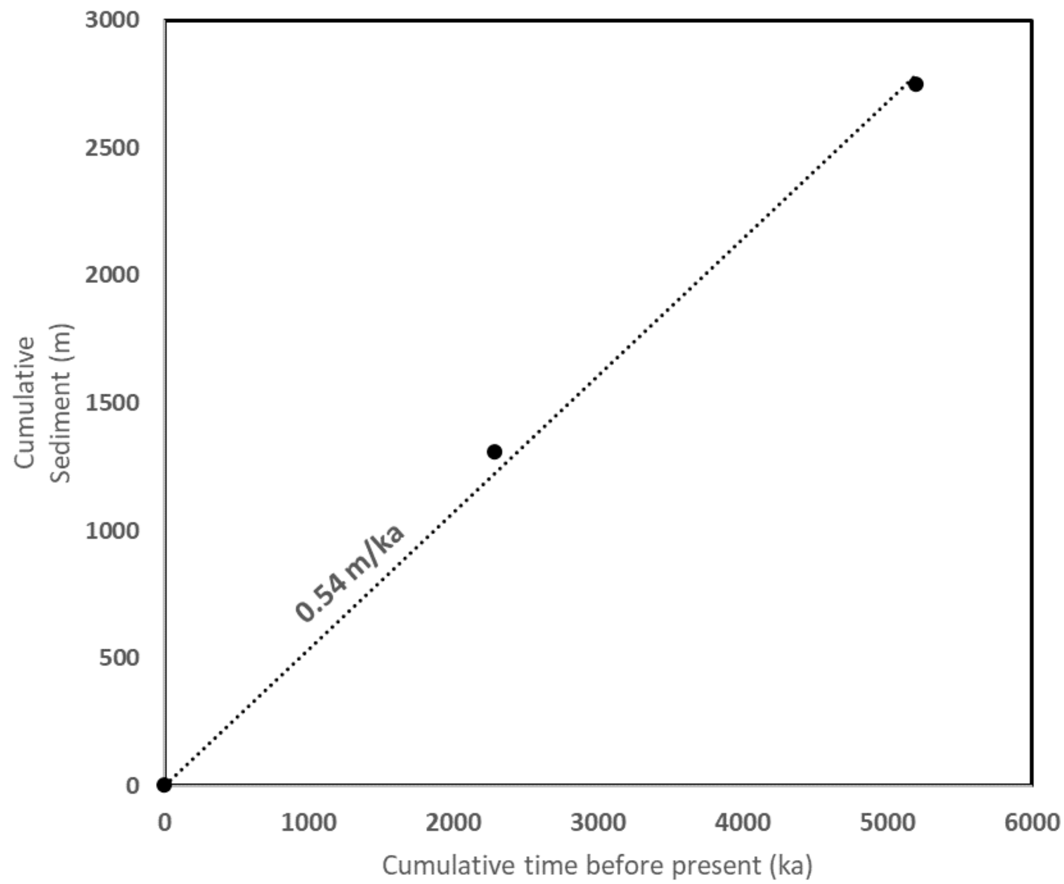

Figure 32 Age vs sediment thickness plot for the study area from Well API # 177094078100. Age data was determined for biostratigraphic markers and best-fit trend line gives a long-term sedimentation or subsidence rate of 0.54 m/ka.

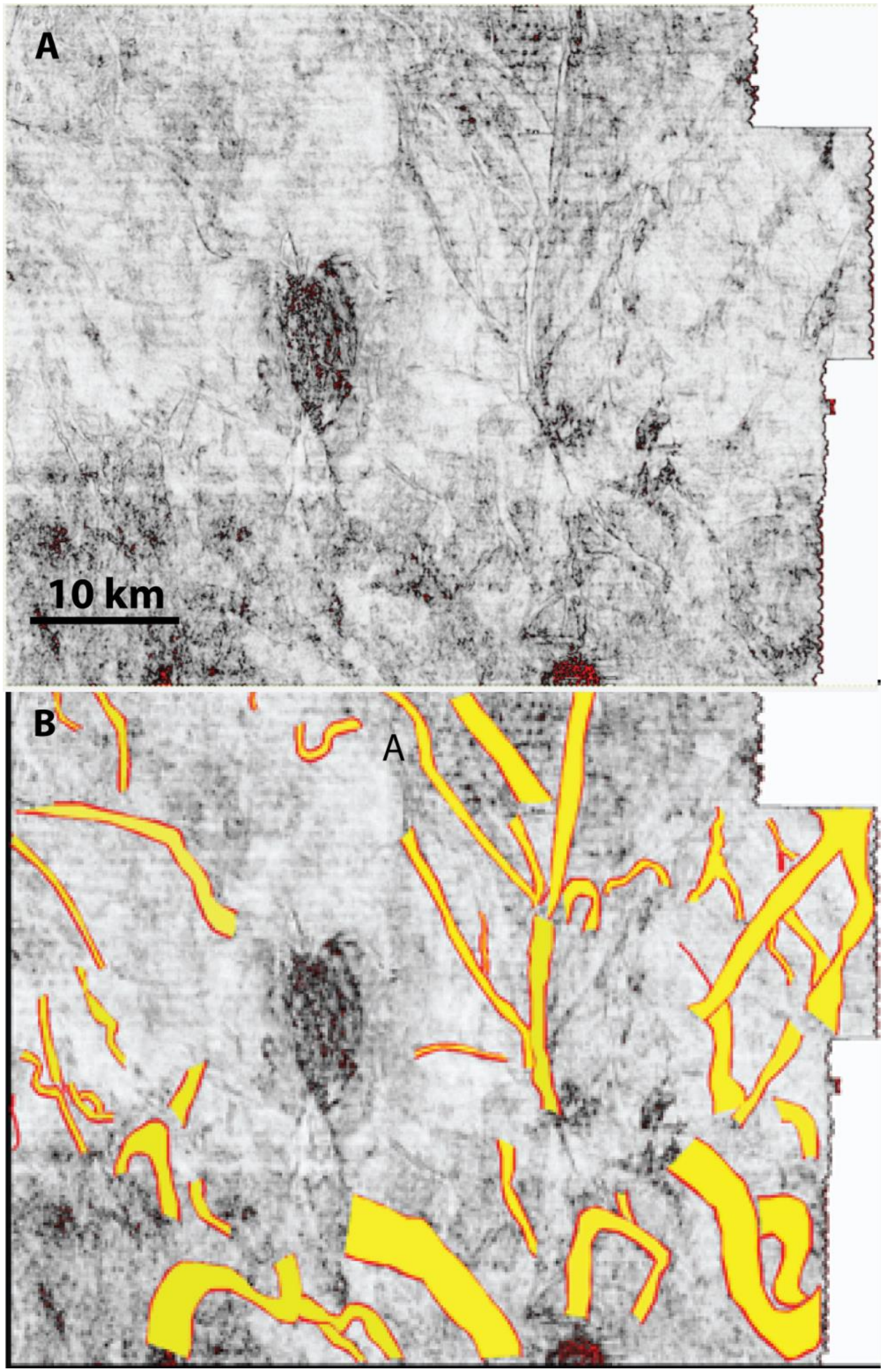

Figure 33 A variance time-slice from EQ time-period. Panel A shows the uninterpreted section and Panel B shows the interpreted channels in yellow.

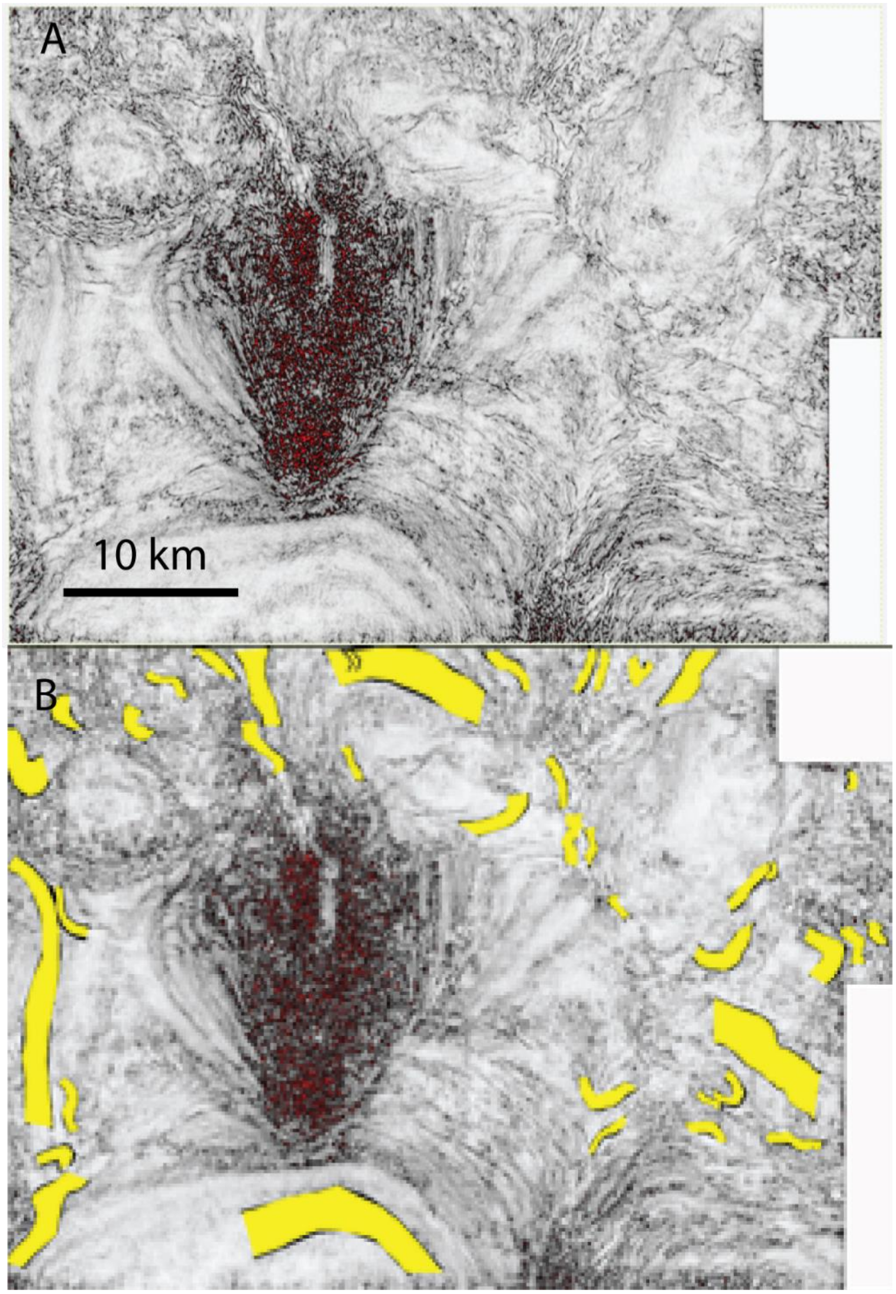

Figure 34 shows a variance time-slice from LM time-period. Panel A shows the uninterpreted section and Panel B shows the interpreted channels in yellow.

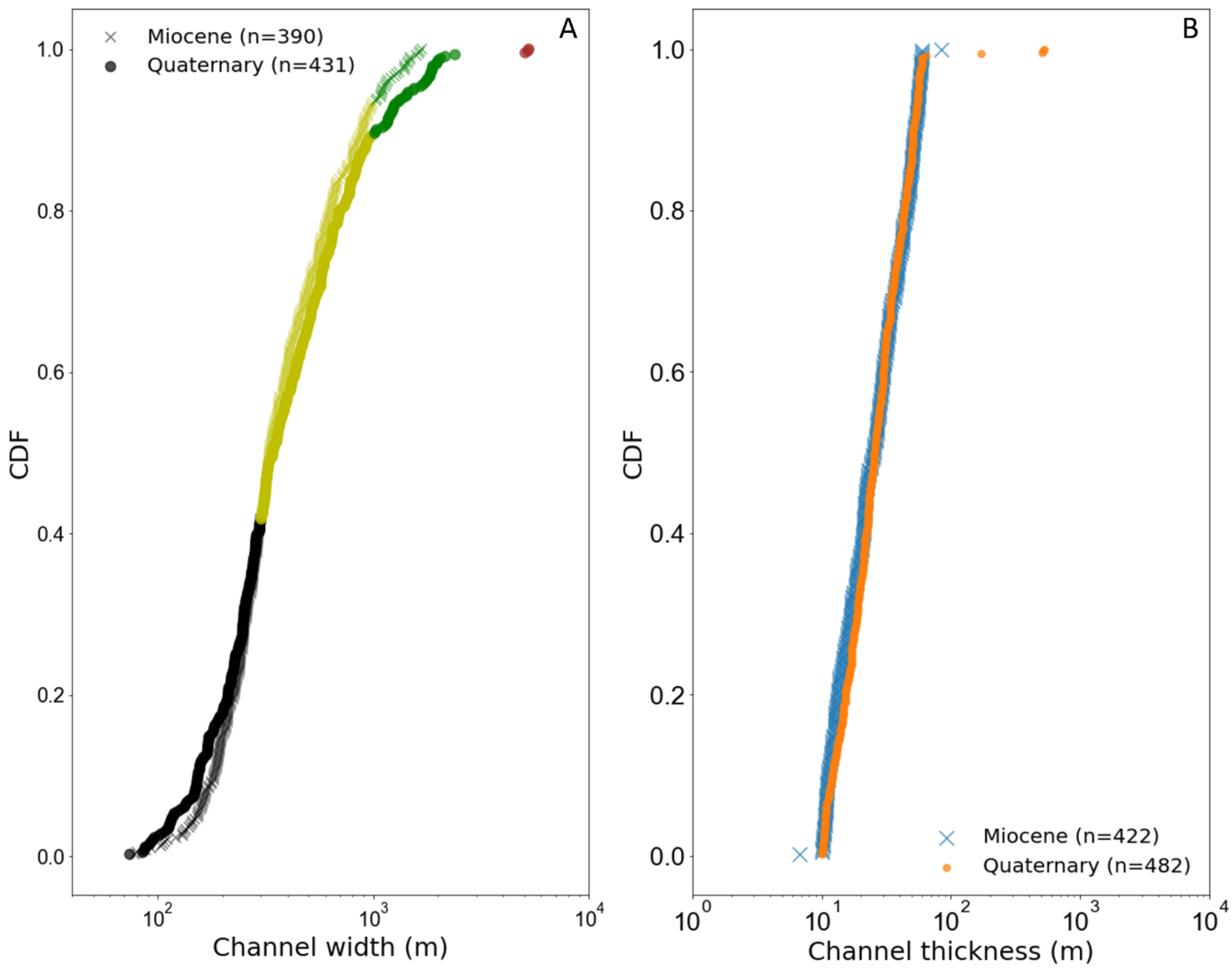

Figure 35 A comparison of channel body widths and thickness between Early Quaternary (shown by circles) and Late Miocene (shown by crosses). The first figure shows the cumulative distribution function of the channel body widths, and the second figure shows the same of the channel body thickness. In both cases, the distributions are similar for two time periods with the exception of the largest channel body features in which the Early Quaternary has a pronounced heavy tail signifying presence of paleovalleys, meaning the EQ stratigraphy preserved the RSL signal.

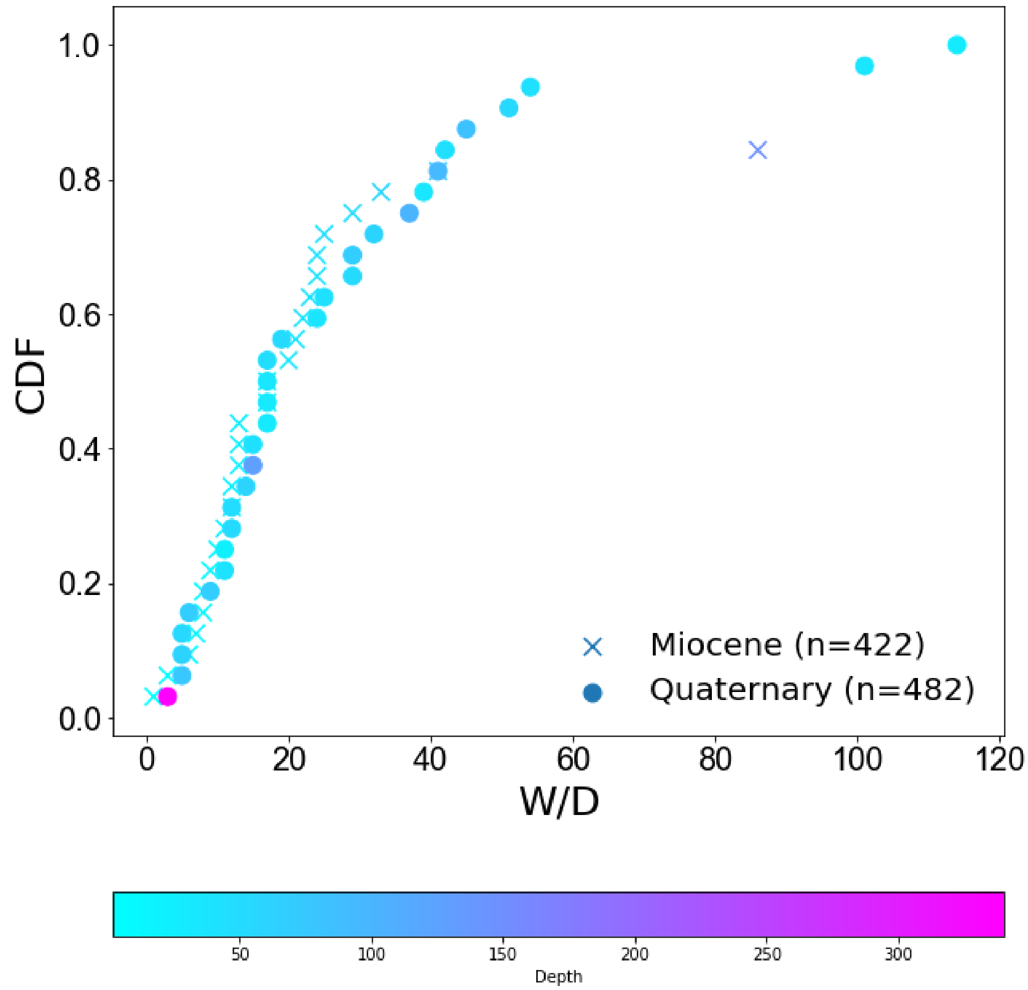

Figure 36 The cumulative distribution function of the width to depth ratio of the EQ (shown by circles) and LM (shown by crosses) channel bodies. Channel bodies are colored according to their thickness, pink signifying deeper channel bodies, blue signifying shallower. Deepest channel-boies from EQ show lower W/D ratio, hence can be considered to be allogenic

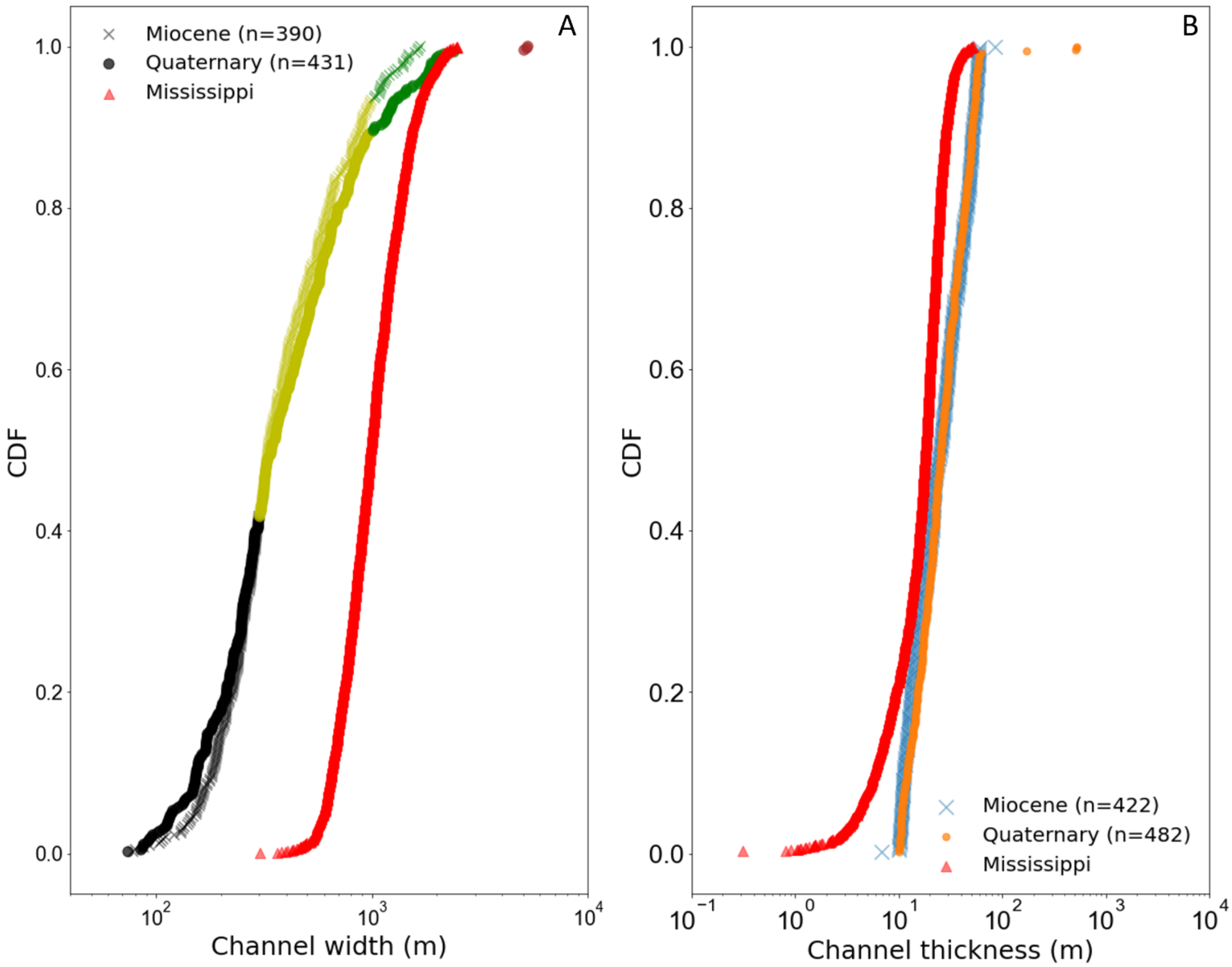

Figure 37 Comparing channel body widths and thickness between EQ (shown by circles), LM (shown by crosses) and the present-day Mississippi river width and depth (shown by red triangles). Panel A shows the cumulative distribution function of the channel body widths, and panel B shows the same of the channel body thickness. In both cases, the difference lies in the heavier tail of the EQ distribution, signifying presence of paleovalleys, which is not seen in the present-day Mississippi river, which is similar to the LM distribution.

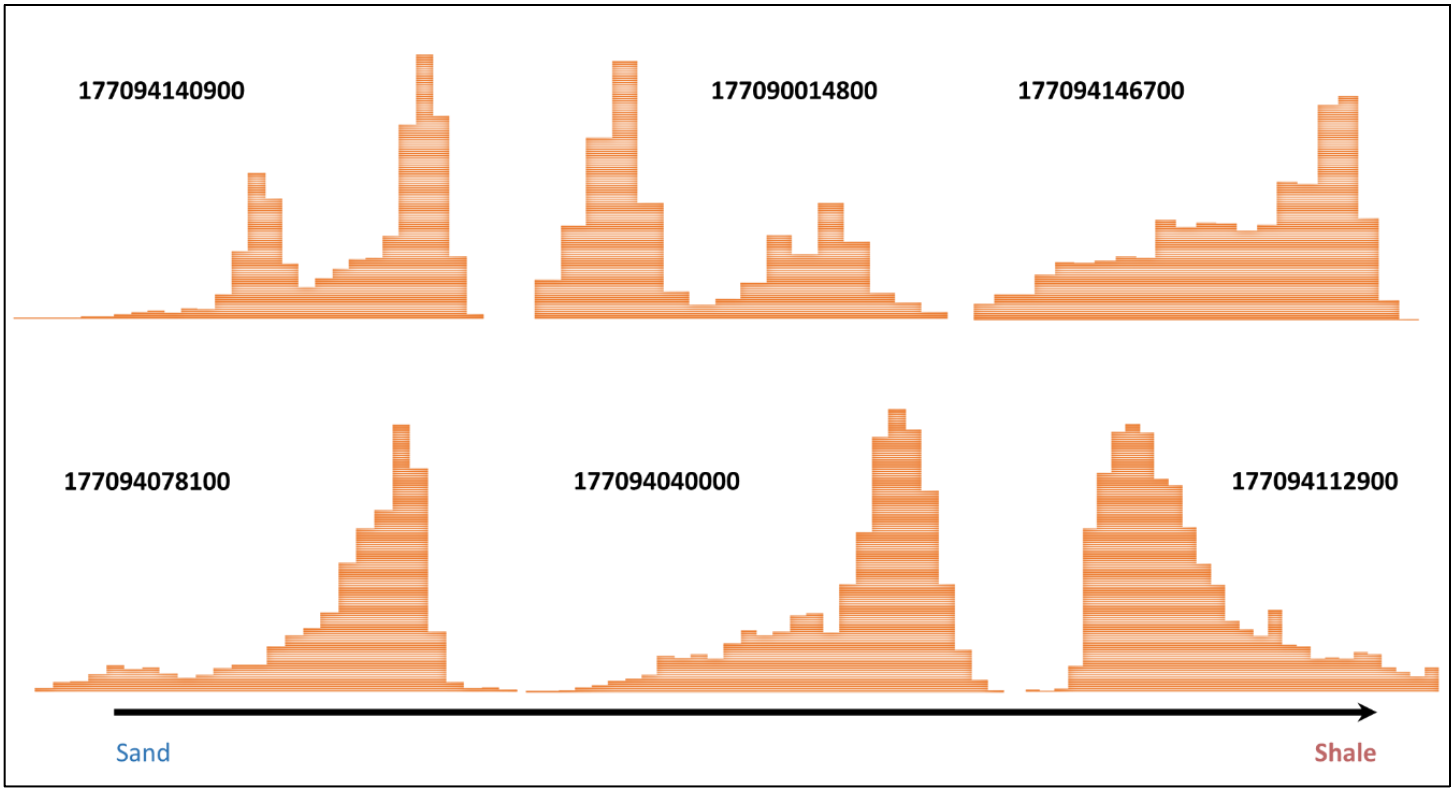

Figure 38 The bar diagrams showing the distributions of GR values for the Miocene stratigraphy in the six wells. The first two wells show a distinct bimodal distributions, which show an almost equal distribution of sand and shale.

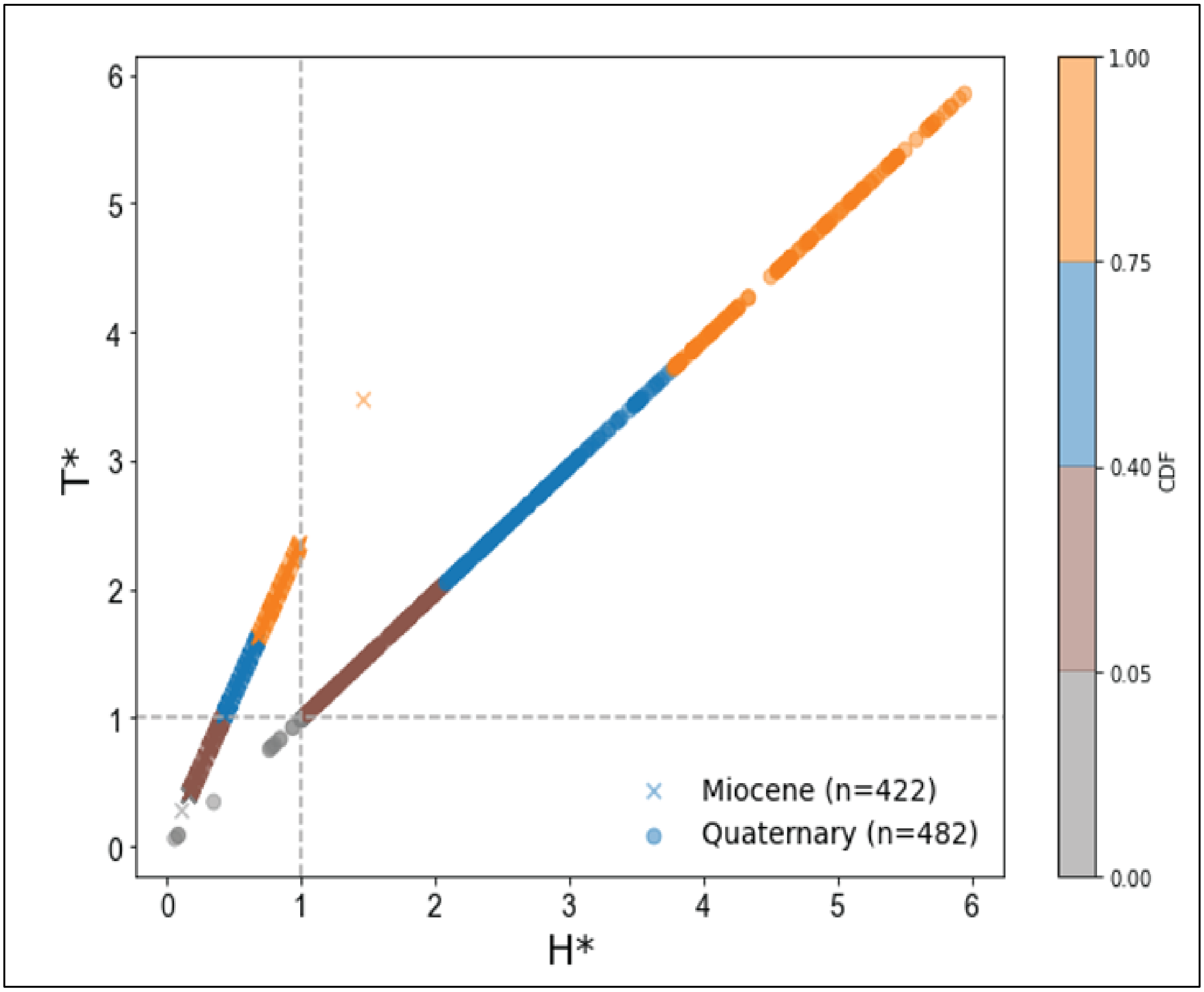

Figure 39 Plot showing H and T* values of EQ (shown by circles) and LM (shown by crosses). The area where H* and T* are less than 1 is the shredding regime and the rest of the space is the preservation regime. Symbols are colored by their CDF values, shown in the corresponding colorbar*

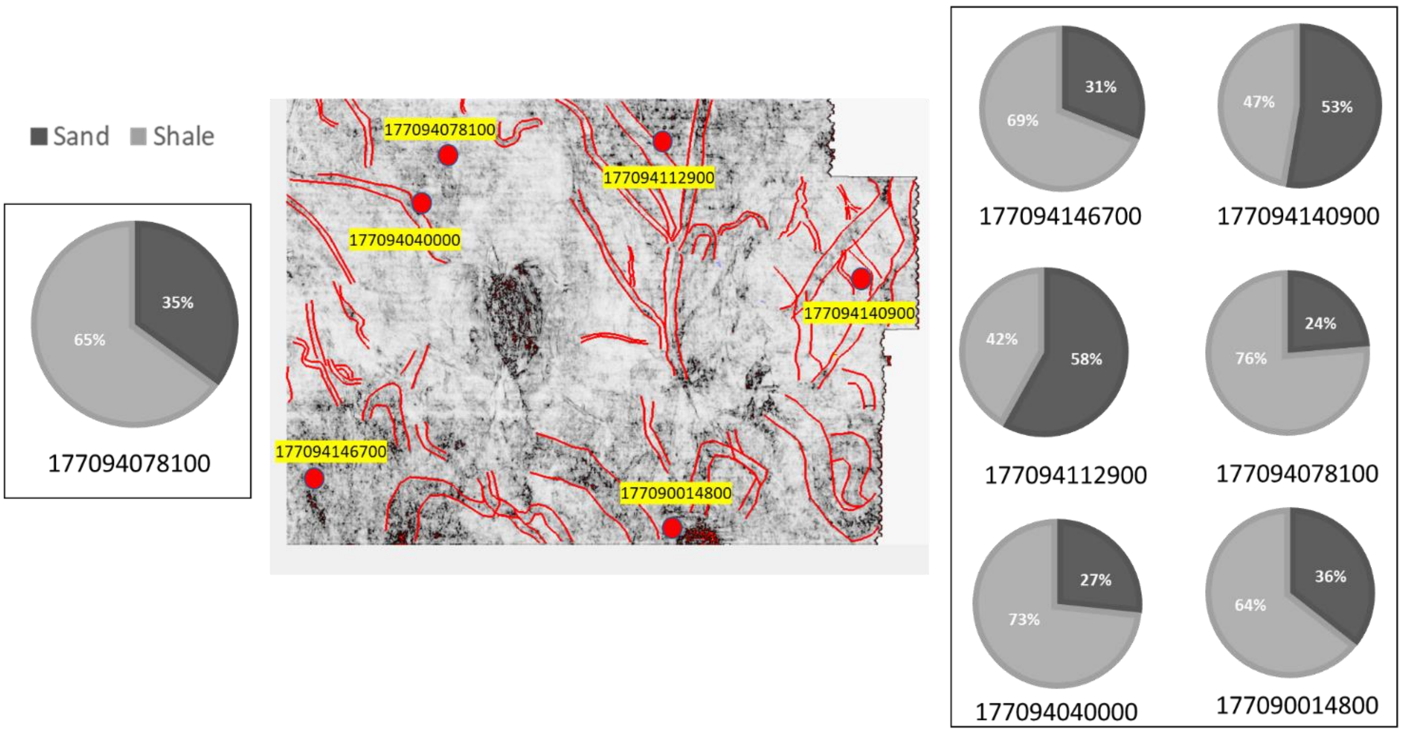

Figure 40 Location of the well logs in the study area shown in the map. The sand:shale ratio is shown with pie charts. The one in the left is from EQ and the six pie charts in the right are from LM.

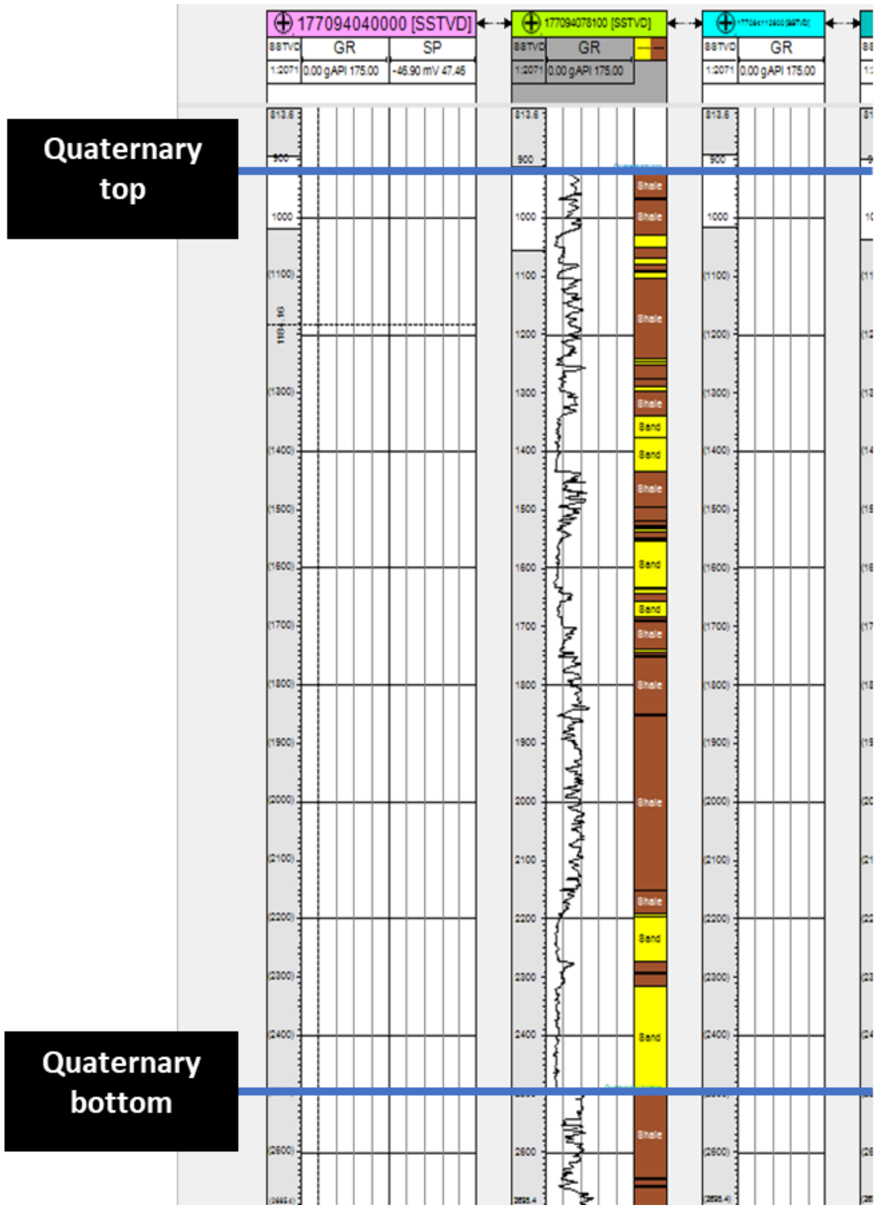

Figure 41 The well-log spans from Quaternary and Miocene strata. The first column shows the GR log, which is followed by the calculated sand-shale log. The yellow boxes in the sand shale log represents sand in the stratigraphy and the brown boxes represents shale.

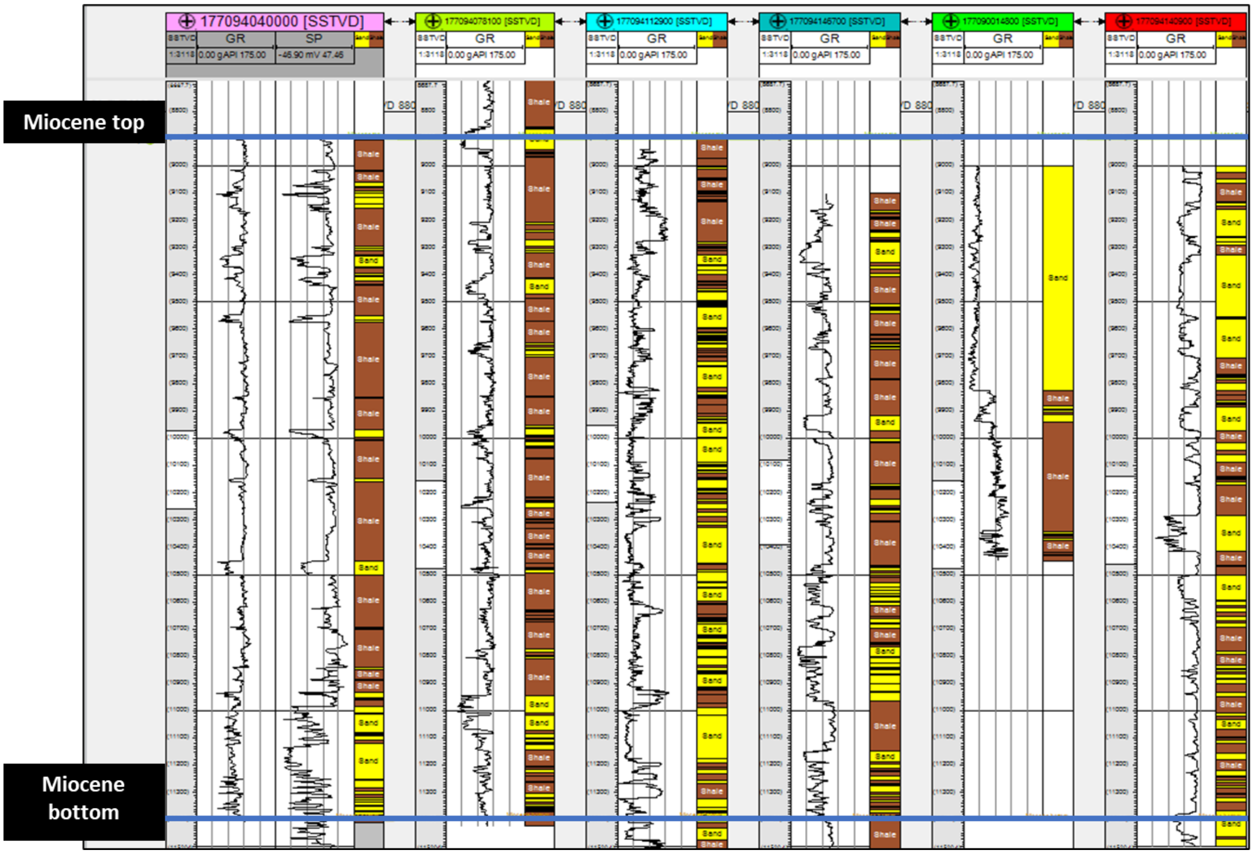

Figure 42 The logs from the six wells that span the Miocene. The first column shows the GR log, which is followed by the calculated sand-shale log. The yellow boxes in the sand shale log represents sand in the stratigraphy and the brown boxes represents shale. The first well also has SP log, shown in the second column. The blue lines denote top and bottom of Miocene.

Akers, W., 1955, Some planktonic foraminifera of the American Gulf Coast and suggested correlations with the Caribbean Tertiary: Journal of Paleontology, p. 647-664.
Alexander, J. S., McElroy, B. J., Huzurbazar, S., and Murr, M. L., 2020, Elevation gaps in fluvial sandbar deposition and their implications for paleodepth estimation: Geology, v. 48, no. 7, p. 718-722.
Alley, R. B., Clark, P. U., Huybrechts, P., and Joughin, I., 2005, Ice-sheet and sea-level changes: science, v. 310, no. 5747, p. 456-460.
Anderson, J. B., Rodriguez, A., Abdulah, K. C., Fillon, R. H., Banfield, L. A., Mckeown, H. A., and Wellner, J. S., 2004, Late Quaternary stratigraphic evolution of the northern Gulf of Mexico margin: a synthesis: SEPM Special Publication, v. 79, p. 1-23.
Anderson, J. B., Wallace, D. J., Simms, A. R., Rodriguez, A. B., Weight, R. W., and Taha, Z. P., 2016, Recycling sediments between source and sink during a eustatic cycle: Systems of late Quaternary northwestern Gulf of Mexico Basin: Earth-science reviews, v. 153, p. 111-138.
Armitage, J. J., Burgess, P. M., Hampson, G. J., and Allen, P. A., 2018, Deciphering the origin of cyclical gravel front and shoreline progradation and retrogradation in the stratigraphic record: Basin Research, v. 30, p. 15-35.
Bentley Sr, S., Blum, M., Maloney, J., Pond, L., and Paulsell, R., 2016, The Mississippi River source-to-sink system: Perspectives on tectonic, climatic, and anthropogenic influences, Miocene to Anthropocene: Earth-Science Reviews, v. 153, p. 139-174.
Best, J. L., and Ashworth, P. J., 1997, Scour in large braided rivers and the recognition of sequence stratigraphic boundaries: Nature, v. 387, no. 6630, p. 275-277.
Bhattacharya, J. P., 2011, Practical problems in the application of the sequence stratigraphic method and key surfaces: integrating observations from ancient fluvial-deltaic wedges with Quaternary and modelling studies: Sedimentology, v. 58, no. 1, p. 120-169.
Blum, M., 2019, Organization and reorganization of drainage and sediment routing through time: The Mississippi River system: Geological Society, London, Special Publications, v. 488, no. 1, p. 15-45.
Blum, M., Martin, J., Milliken, K., and Garvin, M., 2013, Paleovalley systems: Insights from Quaternary analogs and experiments: Earth-Science Reviews, v. 116, p. 128-169.
Blum, M., and Pecha, M., 2014, Mid-Cretaceous to Paleocene North American drainage reorganization from detrital zircons: Geology, v. 42, no. 7, p. 607-610.
Blum, M. D., Hattier-Womack, J., Kneller, B., Martinsen, O., and McCaffrey, B., 2009, Climate change, sea-level change, and fluvial sediment supply to deepwater depositional systems: External Controls on Deep Water Depositional Systems: SEPM, Special Publication, v. 92, p. 15-39.
Blum, M. D., Milliken, K. T., Pecha, M. A., Snedden, J. W., Frederick, B. C., and Galloway, W. E., 2017, Detrital-zircon records of Cenomanian, Paleocene, and Oligocene Gulf of Mexico drainage integration and sediment routing: Implications for scales of basin-floor fans: Geosphere, v. 13, no. 6, p. 2169-2205.

Blum, M. D., and Price, D. M., 1998, Quaternary alluvial plain construction in response to glacio-eustatic and climatic controls, Texas Gulf coastal plain.

Burgess, P. M., and Prince, G. D., 2015, Non-unique stratal geometries: implications for sequence stratigraphic interpretations: Basin Research, v. 27, no. 3, p. 351-365.

Burgess, P. M., Steel, R. J., Granjeon, D., Hampson, G., and Dalrymple, R., 2008, Stratigraphic forward modeling of basin-margin clinoform systems: Implications for controls on topset and shelf width and timing of formation of shelf-edge deltas: Recent advances in models of siliciclastic shallow-marine stratigraphy, v. 90, p. 35-45.

Buzas-Stephens, P., Livsey, D. N., Simms, A. R., and Buzas, M. A., 2014, Estuarine foraminifera record Holocene stratigraphic changes and Holocene climate changes in ENSO and the North American monsoon: Baffin Bay, Texas: Palaeogeography, Palaeoclimatology, Palaeoecology, v. 404, p. 44-56.

Catuneanu, O., Abreu, V., Bhattacharya, J. P., Blum, M. D., Dalrymple, R. W., Eriksson, P. G., Fielding, C. R., Fisher, W. L., Galloway, W. E., Gibling, M. R., Giles, K. A., Holbrook, J. M., Jordan, R., Kendall, C. G. S. C., Macurda, B., Martinsen, O. J., Miall, A. D., Neal, J. E., Nummedal, D., Pomar, L., Posamentier, H. W., Pratt, B. R., Sarg, J. F., Shanley, K. W., Steel, R. J., Strasser, A., Tucker, M. E., and Winker, C., 2009a, Towards the standardization of sequence stratigraphy: Earth-Science Reviews, v. 92, no. 1, p. 1-33.

-, 2009b, Towards the standardization of sequence stratigraphy: Earth-Science Reviews, v. 92, p. 1-33.

Chapin, C. E., 2008, Interplay of oceanographic and paleoclimate events with tectonism during middle to late Miocene sedimentation across the southwestern USA: Geosphere, v. 4, no. 6, p. 976-991.

Ciarletta, D. J., Lorenzo-Trueba, J., and Ashton, A., 2019, Mechanism for retreating barriers to autogenically form periodic deposits on continental shelves: Geology, v. 47, no. 3, p. 239-242.

Clark, P. U., McCabe, A. M., Mix, A. C., and Weaver, A. J., 2004, Rapid rise of sea level 19,000 years ago and its global implications: Science, v. 304, no. 5674, p. 1141-1144.

Combellas-Bigott, R. I., and Galloway, W. E., 2006, Depositional and structural evolution of the middle Miocene depositional episode, east-central Gulf of Mexico: AAPG bulletin, v. 90, no. 3, p. 335-362.

Diegel, F. A., Karlo, J., Schuster, D., Shoup, R., and Tauvers, P., 1995, Cenozoic structural evolution and tectono-stratigraphic framework of the northern Gulf Coast continental margin: in M. P. A. Jackson, D. G. Roberts, and S. Snelson, eds., Salt tectonics: a global perspective: AAPG Memoir, v. 65, p. 109-151.

Fairbanks, R. G., 1989, A 17,000-year glacio-eustatic sea level record: influence of glacial melting rates on the Younger Dryas event and deep-ocean circulation: Nature, v. 342, no. 6250, p. 637-642.

Feeley, M., Moore Jr, T., Loutit, T., and Bryant, W., 1990, Sequence stratigraphy of Mississippi Fan related to oxygen isotope sea level index: AAPG bulletin, v. 74, no. 4, p. 407-424.

Fisk, H. N., and McFarlan Jr, E., 1955, Late Quaternary deltaic deposits of the Mississippi River: Geological Society of America Special Paper, v. 62, p. 279-302.

Frederick, B. C., Blum, M., Fillon, R., and Roberts, H., 2019, Resolving the contributing factors to Mississippi Delta subsidence: Past and Present: Basin Research, v. 31, no. 1, p. 171-190.

Galloway, W. E., 1989, Genetic stratigraphic sequences in basin analysis II: application to northwest Gulf of Mexico Cenozoic basin: AAPG Bulletin, v. 73, no. 2, p. 143-154.

-, 2008, Depositional evolution of the Gulf of Mexico sedimentary basin: Sedimentary basins of the world, v. 5, p. 505-549.

Galloway, W. E., Ganey-Curry, P. E., Li, X., and Buffler, R. T., 2000, Cenozoic depositional history of the Gulf of Mexico basin: AAPG Bulletin, v. 84, no. 11, p. 1743-1774.

Galloway, W. E., Whiteaker, T. L., and Ganey-Curry, P., 2011, History of Cenozoic North American drainage basin evolution, sediment yield, and accumulation in the Gulf of Mexico basin: Geosphere, v. 7, no. 4, p. 938-973.

Ganti, V., Chu, Z., Lamb, M. P., Nittrouer, J. A., and Parker, G., 2014, Testing morphodynamic controls on the location and frequency of river avulsions on fans versus deltas: Huanghe (Yellow River), China: Geophysical Research Letters, v. 41, no. 22, p. 7882-7890.

Ganti, V., Lamb, M. P., and Chadwick, A. J., 2019, Autogenic Erosional Surfaces in Fluvio-deltaic Stratigraphy from Floods, Avulsions, and Backwater Hydrodynamics: Journal of Sedimentary Research, v. 89, no. 8, p. 815-832.

Gibling, M. R., 2006, Width and thickness of fluvial channel bodies and valley fills in the geological record: a literature compilation and classification: Journal of Sedimentary Research, v. 76, p. 731-770.

Gibling, M. R., Fielding, C. R., and Sinha, R., 2011, Alluvial valleys and alluvial sequences: towards a geomorphic assesment, *in* North, C. P., ed., From Rivers to Rock: Geological Society of London Special Publication.

Haq, B. U., 1991, Sequence stratigraphy, sea-level change, and significance for the deep sea: Sedimentation, Tectonics and Eustasy: Sea-Level Changes at Active Margins, p. 1-39.

Haq, B. U., Hardenbol, J., and Vail, P. R., 1987, Chronology of fluctuating sea levels since the Triassic: Science, v. 235, no. 4793, p. 1156-1167.

Harris, A. D., Baumgardner, S. E., Sun, T., and Granjeon, D., 2018, A Poor Relationship Between Sea Level and Deep-Water Sand Delivery: Sedimentary Geology, v. 370, p. 42-51.

Harris, A. D., Covault, J. A., Madof, A. S., Sun, T., Sylvester, Z., and Granjeon, D., 2016, Three-Dimensional Numerical Modeling of Eustatic Control On Continental-Margin Sand DistributionA. D. HARRIS ET AL. NUMERICAL MODELING OF EUSTATIC CONTROL ON CONTINENTAL-MARGIN SAND DISTRIBUTION: Journal of Sedimentary Research, v. 86, no. 12, p. 1434-1443.

Imbrie, J., and Imbrie, J. Z., 1980, Modeling the climatic response to orbital variations: Science, v. 207, no. 4434, p. 943-953.

Jerolmack, D. J., and Paola, C., 2010, Shredding of environmental signals by sediment transport: Geophysical Research Letters, v. 37, p. L19401.
Kim, W., Paola, C., Martin, J., Perlmutter, M. A., and Tapaha, F., 2009, Net pumping of sediment into deep water due to base-level cycling: Experimental and theoretical results, *in* Kneller, B., Martinsen, O. J., and McCaffrey, B., eds., External Controls on Deep-Water Depositional Systems: SEPM Special Publication 92, p. 41-56.
Kim, Y., Kim, W., Cheong, D., Muto, T., and Pyles, D. R., 2013, Piping coarse-grained sediment to a deep water fan through a shelf-edge delta bypass channel: Tank experiments: Journal of Geophysical Research: Earth Surface, v. 118, no. 4, p. 2279-2291.
Krynine, P. D., 1948, The megascopic study and field classification of sedimentary rocks: The Journal of Geology, v. 56, no. 2, p. 130-165.
Li, Q., Yu, L., and Straub, K. M., 2016, Storage thresholds for relative sea-level signals in the stratigraphic record: Geology, v. 44, no. 3, p. 179-182.
Licciardi, J. M., Clark, P. U., Jenson, J. W., and Macayeal, D. R., 1998, Deglaciation of a soft-bedded Laurentide Ice Sheet: Quaternary Science Reviews, v. 17, no. 4-5, p. 427-448.
Lisiecki, L. E., and Raymo, M. E., 2005, A Pliocene-Pleistocene stack of 57 globally distributed benthic delta O-18 records (vol 20, art no PA1003, 2005): Paleoceanography, v. 20, no. 2.
McMillan, M. E., Heller, P. L., and Wing, S. L., 2006, History and causes of post-Laramide relief in the Rocky Mountain orogenic plateau: Geological Society of America Bulletin, v. 118, no. 3-4, p. 393-405.
Miller, K. G., Kominz, M. A., Browning, J. V., Wright, J. D., Mountain, G. S., Katz, M. E., Sugarman, P. J., Cramer, B. S., Christie-Blick, N., and Pekar, S. F., 2005, The phanerozoic record of global sea-level change: Science, v. 310, no. 5752, p. 1293-1298.
Mohrig, D., Heller, P. L., Paola, C., and Lyons, W. J., 2000, Interpreting avulsion process from ancient alluvial sequences: Guadalope-Matarranya (northern Spain) and Wasatch Formation (western Colorado): Geoogical Society of America Bulletin, v. 112, p. 1787-1803.
Nittrouer, J. A., 2013, Backwater hydrodynamics and sediment transport in the lowermost Mississippi River Delta: Implications for the development of fluvial-deltaic landforms in a large lowland river: IAHS-AISH Publ, v. 358, p. 48-61.
Nittrouer, J. A., Shaw, J., Lamb, M. P., and Mohrig, D., 2012, Spatial and temporal trends for water-flow velocity and bed-material sediment transport in the lower Mississippi River: Geological Society of America Bulletin, v. 124, no. 3-4, p. 400-414.
Olariu, C., and Steel, R. J., 2009, Influence of point-source sediment-supply on modern shelf-slope morphology: Implications for interpretation of ancient shelf margins: Basin Research, v. 21, no. 5, p. 484-501.
Paola, C., 2000, Quantitative models of sedimentary basin filling: Sedimentology, v. 47, p. 121-178.

Paola, C., Ganti, V., Mohrig, D., Runkel, A. C., and Straub, K. M., 2018, Time Not Our Time: Physical Controls on the Preservation and Measurement of Geologic Time: Annual Review of Earth and Planetary Sciences, v. 46, p. 409-438.

Peel, F., Travis, C., and Hossack, J., 1995, Genetic structural provinces and salt tectonics of the Cenozoic offshore US Gulf of Mexico: A preliminary analysis: in M. P. A. Jackson, D. G. Roberts, and S. Snelson, eds., Salt tectonics: a global perspective:AAPG Memoir, v. 65, p. 153-175.

Peel, F. J., 2014, How do salt withdrawal minibasins form? Insights from forward modelling, and implications for hydrocarbon migration: Tectonophysics, v. 630, p. 222-235.

Pettijohn, F., Potter, P., and Siever, R., 1972, Sand and Sandstone. Springer-Verlag, Berlin Heidelberg New York.

Posamentier, H. W., and Vail, P. R., 1988a, Eustatic controls on clastic deposition II - sequence and systems tract models, *in* Wilgus, C. K., Hastings, B. S., Posamentier, H. P., Van Wagoner, J. V., Ross, C. A., and Kendall, C. G. S. C., eds., Sea-Level Changes, SEPM special publicaiton 42, p. 125-154.

-, 1988b, Eustatic Controls on Clastic Deposition II—sequence and Systems Tract Models: SEPM Special Publications, p. 125-154.

Raymo, M. E., Lisiecki, L., and Nisancioglu, K. H., 2006, Plio-Pleistocene ice volume, Antarctic climate, and the global δ18O record: Science, v. 313, no. 5786, p. 492-495.

Romans, B. W., Castelltort, S., Covault, J. A., Fildani, A., and Walsh, J., 2016, Environmental signal propagation in sedimentary systems across timescales: Earth-Science Reviews, v. 153, p. 7-29.

Sadler, P. M., 1981, Sediment accumulation rates and the completeness of stratigraphic sections: Journal of Geology, v. 89, p. 569-584.

Saucier, R. T., 1994, Geomorphology and Quaternary geologic history of the Lower Mississippi Valley, US Army Engineer Waterways Experiment Station.

Simms, A. R., Anderson, J. B., DeWitt, R., Lambeck, K., and Purcell, A., 2013, Quantifying rates of coastal subsidence since the last interglacial and the role of sediment loading: Global and planetary change, v. 111, p. 296-308.

Strong, N., and Paola, C., 2008, Valleys that never were: time surfaces versus stratigraphic surfaces: Journal of Sedimentary Research, v. 78, no. 7-8, p. 579-593.

Swartz, J. M., Cardenas, B. T., Mohrig, D., and Passalacqua, P., 2022, Tributary channel networks formed by depositional processes: Nature Geoscience, v. 15, no. 3, p. 216-221.

Sylvester, Z., Durkin, P., Hubbard, S., and Mohrig, D., 2021, Autogenic translation and counter point bar deposition in meandering rivers: GSA Bulletin.

Toby, S. C., Duller, R. A., De Angelis, S., and Straub, K. M., 2019, A stratigraphic framework for the preservation and shredding of environmental signals: Geophysical Research Letters.

Tofelde, S., Savi, S., Wickert, A. D., Bufe, A., and Schildgen, T. F., 2019, Alluvial channel response to environmental perturbations: fill-terrace formation and sediment-signal disruption: Earth Surface Dynamics, v. 7, no. 2, p. 609-631.

Trampush, S., Hajek, E., Straub, K., and Chamberlin, E., 2017, Identifying autogenic sedimentation in fluvial-deltaic stratigraphy: Evaluating the effect of outcrop-quality data on the compensation statistic: Journal of Geophysical Research-Earth Surface, v. 122, p. 1-23.

Trampush, S. M., and Hajek, E. A., 2017, Preserving proxy records in dynamic landscapes: Modeling and examples from the Paleocene-Eocene Thermal Maximum: Geology, v. 45, no. 11, p. 967-970.

Trower, E. J., Ganti, V., Fischer, W. W., and Lamb, M. P., 2018, Erosional surfaces in the Upper Cretaceous Castlegate Sandstone (Utah, USA): Sequence boundaries or autogenic scour from backwater hydrodynamics?: Geology, v. 46, no. 8, p. 707-710.

Van De Wiel, M. J., and Coulthard, T. J., 2010, Self-organized criticality in river basins: Challenging sedimentary records of environmental change: Geology, v. 38, no. 1, p. 87-90.

Van Wagoner, J., Posamentier, H., Mitchum, R., Vail, P., Sarg, J., Loutit, T., and Hardenbol, J., 1988, An overview of the fundamentals of sequence stratigraphy and key definitions.

Van Wagoner, J. C., 1995, Sequence stratigraphy and marine to nonmarine facies architecture of foreland basin strata, Book Cliffs, Utah, U.S.A., *in* Van Wagoner, J. C., and Bertram, G. T., eds., Sequence Stratigraphy of Foreland Basin Deposits: Outcrop and Subsurface Examples from the Createaceous of North America, Volume 64, American Association of Petroleum Geologists, Memoirs, p. 137-223.

von der Heydt, A., Grossmann, S., and Lohse, D., 2003, Response maxima in modulated turbulence. II. Numerical simulations: Physical Review E, v. 68, no. 6, p. 066302.

Wang, Y., Straub, K. M., and Hajek, E. A., 2011, Scale-dependent compensational stacking: An estimate of autogenic time scales in channelized sedimentary deposits: Geology, v. 39, no. 9, p. 811-814.

Weimer, P., 1991, Sequence stratigraphy of the Mississippi Fan related to oxygen isotope sea level index: discussion: AAPG Bulletin, v. 75, no. 9, p. 1500-1507.

Winker, C. D., 1982, Cenozoic shelf margins, northwestern Gulf of Mexico.

Wolstencroft, M., Shen, Z., Törnqvist, T. E., Milne, G. A., and Kulp, M., 2014, Understanding subsidence in the Mississippi Delta region due to sediment, ice, and ocean loading: Insights from geophysical modeling: Journal of Geophysical Research: Solid Earth, v. 119, no. 4, p. 3838-3856.

Wu, X., 2004, Upper Miocene depositional history of the central Gulf of Mexico Basin, The University of Texas at Austin.

Xu, J., Snedden, J. W., Galloway, W. E., Milliken, K. T., and Blum, M. D., 2017, Channel-belt scaling relationship and application to early Miocene source-to-sink systems in the Gulf of Mexico basin: Geosphere, v. 13, no. 1, p. 179-200.

Yu, L., Li, Q., and Straub, K. M., 2017, Scaling the Response of Deltas To Relative-Sea-Level Cycles By Autogenic Space and Time Scales: A Laboratory Study: Journal of Sedimentary Research, v. 87, no. 8, p. 817-837.

Zachos, J., Pagani, M., Sloan, L., Thomas, E., and Billups, K., 2001, Trends, rhythms, and aberrations in global climate 65 Ma to present: science, v. 292, no. 5517, p. 686-693.

CONCLUSIONS

I have explored RSL change and its effect on sediment transport on the continental shelf system in this dissertation. Mass redistribution, both in the form of water and sediments, on the shelf is an active area of research and this dissertation advances the fields of paleo-sea level studies as well as sediment transport and stratigraphy.

In the first chapter of this dissertation, I have identified the North American ice sheet, and not the Antarctic ice sheet, as the dominant source of meltwater that was being added to the global oceans during the 9-7 ka time-period. I have also shown that the ice models being used hitherto were underestimating the amount of meltwater that was being produced by the North American ice sheet by at least ~14 m. This work has the potential to change our perspective about the events that led to the most recent abrupt climate change event, the 8.2 kyr event, as well as help us in understanding future climate change events.

In the next two chapters, I look at processes related to sediment transport and preservation of these sediments and the signals embedded in them with relation of relative sea level change. This work adds to the idea of stochasticity and non-unique solutions in sediment transport and sequence stratigraphic models. I provide new insight into the progradation of the continental shelf edge and transport of sediments into the deeper ocean during lowstand sea level change depending on the available sediment flux and the distance between the shelf edge and the lowstand shoreline in the second chapter of my dissertation.

Preservation of relative sea level signals and reconstructing these relative sea level changes have been a big part of sequence stratigraphy. In the third chapter, I question the rationale that all RSL signals are equally preserved in the stratigraphy and can be reconstructed, using seismic data and the theory of signal shredding. I show that only larger RSL signals are stored in a large depositional basin like the Mississippi River and smaller RSL signals are effectively shredded. This is the first field testing of the signal shredding theory.

This dissertation advances the fields of stratigraphy, sediment transport processes and paleo sea-level studies. However, several questions and gaps in data have been raised by this dissertation which I hope to answer in the future. The dearth in both RSL as well as stratigraphic data from the Southern Hemisphere can be a barrier in answering some of these questions. Better constraints on sea level from places such as Africa, South America and Australia can help us in understanding the contribution of the Antarctic meltwater to the global sea level change. Accessible seismic and stratigraphic data can shed better light on researching the preservation of signals and fundamental questions about effective sediment transport to the deeper ocean during changes of sea level.

BIOGRAPHY